Universität Bremen

ALFRED-WEGENER-INSTITUT
HELMHOLTZ-ZENTRUM FÜR POLAR- UND MEERESFORSCHUNG

On the Flow of Modified Warm Deep Water toward the Filchner Ronne Ice Shelf, Weddell Sea, Antarctica

Der Einstrom von Modifiziertem Warmem Tiefenwasser zum Filchner-Ronne-Schelfeis, Weddellmeer, Antarktis

Dissertation zur Erlangung des akademischen Grades
Doktor der Naturwissenschaften
- Dr. rer. nat -

Fachbereich 1: Physik und Elektrotechnik
Universität Bremen

vorgelegt von
Svenja Ryan

Bremen, Juni 2018

First reviewer:	Prof. Dr. Torsten Kanzow Alfred Wegener Institute Helmholtz Centre for Polar and Marine Research and Institute of Environmental Physics University of Bremen
Second reviewer:	Prof. Dr. Monika Rhein Institute of Environmental Physics University of Bremen
Doctoral colloquium:	4th October 2018

Abstract

Enhanced basal melt rates have been observed at many ice shelves around Antarctica in the last decade, which has mostly been attributed to an increased transport of Circumpolar Deep Water (CDW) onto the continental shelf. One of the largest ice shelves, namely the Filchner Ronne Ice Shelf (FRIS), is located in the southern Weddell Sea and plays a key role in the production of Weddell Sea Deep Water (WSDW) due to ocean-ice shelf interaction. While today the large continental shelf in front of FRIS is covered with cold and dense water, model studies have suggested the potential for an increased flow of Modified Warm Deep Water (MWDW) toward and into the FRIS cavity, via the Filchner Trough, causing a substantial increase in basal melt rates by the end of this century. To gain a better understanding of the relevant processes, this thesis investigates the seasonality of the hydrography along the eastern flank of the Filchner Trough with focus on the MWDW inflow, using ship-based in-situ measurements and mooring time series as well as numerical simulations.

Hydrographic data obtained during two *RV Polarstern* cruises show that the Filchner Trough is filled by a thick doming layer of super-cooled Ice Shelf Water (ISW) emerging from the FRIS cavity. The thickness of this layer increases from the Filchner Sill ($\sim$ 300 m) toward the ice shelf front ($\sim$ 1000 m). Based on hydrographic sections along 76°S, MWDW enters the continental shelf along the shallower eastern flank of the trough above the 400 m isobath. Temperature, salinity and velocity time series at 76°S from 2014 to 2016 reveal a distinct seasonal cycle in hydrography. Southward flow of MWDW with maximum temperatures of -1°C is observed from summer to autumn. Lighter warm water appear first at mid-depth, followed by a denser warm inflow along the bottom about 2 months later. The seasonal inflow is related to the seasonal heaving of the Antarctic Slope Front (ASF) along the continental shelf break, which is suppressed below the shelf break depth of $\sim$ 400 m during winter. A weakly stratified water column is found in winter with temperatures at the surface freezing point ($\theta = -1.9$°C), suggesting shelf convection reaching deeper than 400 m. From spring through to summer, the ISW layer in the trough is found to extend onto the adjacent, shallower shelf further east associated with northward flow. Only when this layer retreats, does is warm inflow observed along the bottom toward the end of summer. The timing of the onset of the MWDW inflow at the shelf break and the strength of the winter convection may determine whether the warm water can reach the ice shelf front.

With the aim to further analyse the seasonal and interannual variability of the MWDW flow toward FRIS, a global configuration of the Finite Element Sea ice-Ocean Model (FESOM) is applied on a newly developed mesh. The mean resolution is set to 3 km over the southern Weddell Sea continental shelf and decreases to 15 km in the northeastern Weddell Gyre. An assessment of the modelled Weddell Gyre reveals deficiencies in the used configuration, in particular in the eastern part of the gyre. The results highlight the importance of the inflow along the gyre's eastern boundary for the properties of water masses found above the continental slope circulating around the Weddell Sea. Additionally, high resolution, in the order of the first baroclinic Rossby radius of deformation, is required to maintain a realistic ASF structure in the model. Both are crucial components that impact the MWDW flow onto the southern Weddell Sea continental shelf.

In order to achieve a realistic hydrography associated with the ASF upstream of the Filchner Trough, a new FESOM configuration is developed, where the 3-D temperature and salinity field above the continental slope between Kapp Norvegia and the Brunt Ice Shelf is restored to a climatology, recently compiled from ship-based and seal-tag data. This approach leads to an improved representation of the ASF and, ultimately, the MWDW flow onto the continental shelf. The seasonal southward flow of MWDW along the eastern flank of the Filchner Trough is reproduced in the model. Shelf convection in winter impedes the southward flow, even though the restored hydrography includes only summer data and does not capture the observed seasonal heaving of the ASF. This results in MWDW being present above the shelf break depth all year around. It is shown that higher densities in the trough and on the adjacent shelf area can lead to a thicker layer of MWDW inflow at mid-depth, by lifting the isopycnals at the shelf break, while lower densities lead to a concentrated inflow along the bottom of the Eastern Shelf. The model results suggest that at present-day conditions, with ISW filling the Filchner Trough, there is no direct pathway along the Eastern Shelf for MWDW to enter the FRIS cavity. This is likely due to the narrowing of the continental shelf toward the south. As a conclusion, FRIS may, unlike other ice shelves around Antarctica, be protected from warm intrusion as long as dense water in the trough forces the MWDW inflow to isobaths shallower than 500 m on the Eastern Shelf.

Zusammenfassung

An vielen Schelfeisen in der Antarktis wurden über das letzte Jahrzehnt erhöhte basale Schmelzraten beobachtet, was hauptsächlich auf einen zunehmenden Transport von warmem zirkumpolarem Wasser auf das Kontinentalschelf zurückgeführt wurde. Eines der größten Schelfeise in der Antarktis, namentlich das Filchner-Ronne-Schelfeis (FRIS), befindet sich im Süden des Weddellmeeres und spielt eine bedeutende Rolle für die Produktion von Tiefenwasser im Weddellmeer (WSDW) durch Ozean-Schelfeis-Wechselwirkung. Bislang wird auf einem großen Teil des vorgelagerten Kontinentalschelfs kaltes und dichtes Meerwasser produziert. Jedoch deuten Modellstudien auf ein Potential für einen in Zukunft verstärkten Einstrom von modifiertem warmem Tiefenwasser (MWDW) in Richtung FRIS hin. Dieser würde zu einem beträchtlichen Anstieg der basalen Schmelzraten bis zum Ende diesen Jahrhunderts führen. Mit dem Ziel dahingehend relevante Prozesse besser zu verstehen, untersucht diese Arbeit die saisonale Hydrographie entlang der östlichen Flanke des Filchnergrabens, mit Fokus auf den MWDW-Einstrom. Dazu werden schiffsbasierende in-situ Daten und Verankerungsdaten, sowie numerische Simulationen verwendet.

Hydrographische Daten von zwei *RV Polarstern* Expeditionen zeigen, dass der Filchnergraben mit einer dicken, gewölbten Schicht aus supergekühltem Schelfeiswasser (ISW) gefüllt ist, welches in FRIS Kaverne entsteht. Die Dicke dieser Schickt nimmt von der Filchnerschwelle ($\sim 300\,\mathrm{m}$) in Richtung Schelfeiskante zu ($\sim 1000\,\mathrm{m}$). Basierend auf hydrographischen Schnitten entlang 76°S, sieht man, dass MWDW über der 400 m Isobathe entlang der östlichen Flanke des Filchnergrabens auf das Kontinentalschelf fließt. Verankerungszeitserien, aufgenommen zwischen 2014 und 2016 bei 76°S, offenbaren einen deutlichen saisonalen Zyklus der Hydrographie. Ein südwärtiger Strom des MWDWs mit maximalen Temperaturen von 1°C ist von Sommer bis Herbst beobachtet. Das warme Wasser tritt zunächst mit geringerer Dichte in mittlerer Wassertiefe auf, gefolgt von einem dichteren Einstrom entlang des Bodens etwa zwei Monate später. Der saisonale Einstrom kann mit der saisonalen Auf- und Abwärtsbewegung der Front am antarktischen Kontinentalhang (ASF), welche im Winter unterhalb der Schelfkantentiefe von etwa 400 m liegt, in Zusammenhang gebracht werden. Eine Wassersäule mit geringer Schichtung im Winter und Temperaturen um den Oberflächengefrierpunkt ($\theta = -1.9$°C), weisen auf Konvektion auf dem Schelf hin, welche tiefer als 400 m reicht. Vom Frühling bis zum Sommer, erstreckt sich die ISW-Schicht im

Filchnergraben bis auf das anliegende, flacherere Schelf im Osten, in Verbindung mit einer nordwärtigen Strömung. Wenn sich diese Schicht gegen Ende des Sommers zurückzieht, beginnt der warme Einstrom entlang des Bodens. Der Startzeitpunkt des warmen Einstroms an der Schelfkante und die Stärke der Winterkonvektion auf dem Schelf könnte bestimmen, ob das MWDW die Schelfeiskante erreicht oder nicht.

Mit dem Ziel die Analyse der saisonalen und interannualen Variabilität des MWDW-Einstroms in Richtung FRIS zu vertiefen, wird eine globale Konfiguration des Finite Elemente Meereis-Ozean Model (FESOM) auf einem neu erstellten Gitter verwendet. Diese hat eine mittlere Auflösung von 3 km auf dem Kontinentalschelf im südlichen Weddellmeer welche sich auf 15 km im nordöstlichen Weddellwirbel verringert. Eine Untersuchung des modellierten Weddellwirbels zeigt Defizite in der angewendeten Konfiguration auf, welche besonders stark im östlichen Teil des Wirbels ausgeprägt sind. Die Ergebnisse heben die Relevanz des warmen Einstroms entlang des östlichen Randes des Weddellwirbels für die Wassermasseneigenschaften entlang des Kontinentalhangs vor, welche im Weddellmeer rezirkulieren. Des Weiteren ist eine hohe Auflösung, in der Größenordnung des ersten baroklinen Rossbyradius, von Nöten, um eine realistische Struktur der ASF im Model aufrechtzuerhalten. Beide Komponeten haben großen Einfluss auf den MWDW-Einstrom am Kontinentalschelf im südlichen Weddellmeer.

Um eine realisitsche Hydrography entlang des Kontinentalhangs stromaufwärts des Filchnergrabens zu erreichen, wird eine neue FESOM Konfiguration entwickelt, in welcher das 3-D Temperatur- und Salzfeld über dem Kontinentalhang zwischen Kapp Norvegia und dem Brunt Schelfeis auf eine kürzlich entwickelte Klimatologie zurückgesetzt wird, welche schiffsbasierende Beobachtungen und Robbendaten zusammenführt. Dieser Ansatz führt zu einer verbesserten Darstellung der ASF im Modell und, daraus resultierend, einem realistischerem Einstrom von MWDW auf den Kontinentalhang im südlichen Weddellmeer. Der saisonale südwärtige MWDW-Einstrom entlang der östlichen Flank des Filchnergrabens wird im Model reproduziert. Schelf-Konvektion im Winter vehindert die südwärtige Ausbreitung von MWDW, obwohl die verwendete Klimatolgie nur auf Sommerdaten basiert, und somit die ASF im Winter nicht unter die Kontinentalrandtiefe gedrück wird, was einen ganzjährigen warmen Einstrom erlauben würde. Es wird gezeigt, dass höhere Dichten im Filchnergraben und dem anliegenden östlichen Kontitnentalschelf zu einen warmen Einstrom über eine breit-

ere Schicht in der mittleren Wassertiefe führen können, indem die Isopyknen am Kontinentalrand angehoben werden. Im Gegensatz dazu führen geringere Dichten zu einem verstärkten warmen Signal entlang des Bodens, welches sich jedoch über eine geringere Wassertiefe erstreckt. Die Modellresultate deuten an, dass unter gegenwärtigen Bedingungen, in denen der Filchnergraben mit dichtem ISW gefüllt ist, kein direkter Pfad für das MWDW besteht, um über das Schelf östlich des Grabens in die FRIS-Kaverne zu gelangen, da das flache Kontinentalschelf in Richtung Schelfeiskante schmal wird und nicht bis in die Kaverne reicht. Folglich ist es naheliegend, dass FRIS, im Vergleich zu anderen Schelfeisen in der Antarktis, vor dem Eindringen warmen Wassers geschützt ist, solange dichtes Wasser im Graben den warmen Einstrom auf das flachere, östliche Kontinentalschelf zwingt.

List of Acronyms

AABW	Antarctic Bottom Water
ACC	Antarctic Circumpolar Current
ACoC	Antarctic Coastal Current
ADCP	Acoustic Doppler Current Profiler
APE	Available Potential Energy
ASC	Antarctic Slope Current
ASF	Antarctic Slope Front
CDW	Circumpolar Deep Water
CFSR	Climate Forecast System Reanalysis
CTD	Conductivity-Temperature-Depth
DJF	Average over monthly data of December, January, February
EKE	Eddy Kinetic Energy
ESW	Eastern Shelf Water
ENSO	El Niño-Southern Oscillation
FESOM	Finite Element Sea Ice-Ocean Model
FIS	Filchner Ice Shelf
FOW	Filchner Overflow Water, modelled equivalent to ISW
FRIS	Filchner Ronne Ice Shelf
HIGH	Model simulation with high resolution mesh
HSSW	High Salinity Shelf Water
IPCC	Intergovernmental Panel on Climate Change
ISW	Ice Shelf Water
JJA	Average over monthly data of June, July, August
LOW	Model simulation with low resolution
MAM	Average over monthly data of March, April, May
MEOP	Marine Mammals Exploring the Oceans Pole to Pole
MOC	Meridional Overturning Circulation

Continued on next page

List of Acronyms - *Continued from previous page*

MWDW	Modified Warm Deep Water
NADW	North Atlantic Deep Water
NCEP	National Centers for Environmental Prediction
NSIDC	National Snow and Ice Data Center
NOAA	National Oceanic and Atmospheric Administration
SON	Average over monthly data of September, October, November
SSH	Sea Surface Height
PF	Polar Front
RCM	Recording Current Meter
RESTORING	Simulation with regional restoring
RIS	Ronne Ice Shelf
RTopo	Refined Topography data set
RV	Research Vessel
SAF	Subantarctic Front
SAM	Southern Annular Mode
SB	Southern Boundary
SBE	Sea Bird Electronics
SIC	Sea Ice Concentration
STD	Standard Deviation
SW	Surface Water
WDW	Warm Deep Water
WOA	World Ocean Atlas
WSBW	Weddell Sea Bottom Water
WSDW	Weddell Sea Deep Water
WW	Winter Water

Contents

1. Introduction

The Meridional Overturning Circulation (MOC), driven by the atmospheric winds and thermohaline processes, plays a major role in Earth's climate and climate variability. The ocean stores and transports heat, fresh water and carbon around our planet, thus acting as a climate regulator. Large ocean - atmosphere fluxes of heat and fresh water occur in localized regions in the high latitudes, such as the North Atlantic and different sites around the Antarctic continent. Here, the ocean loses heat, hence buoyancy, to the atmosphere and dense waters are formed that sink to form the lower branch of the overturning circulation. The densest water in the global ocean is formed around Antarctica (*Foster and Carmack*, 1976), namely the Antarctic Bottom Water (AABW), which covers large parts of the abyssal ocean in all three major ocean basins(*Mantyla and Reid*, 1983; *Orsi et al.*, 2001). The lighter Northern Hemisphere counterpart, the North Atlantic Deep Water (NADW), sinks to mid-depth, where it flows southward until it is brought to the surface again as part of the the upwelling branch in the Southern Ocean (*Sverdrup*, 1933; *Marshall and Speer*, 2012).

While the deep water formation is mainly driven by buoyancy, strong zonal winds supply the necessary energy for the upwelling. Westerlies over the Southern Ocean drive a northward Ekman transport, creating a divergence in the surface flow south of the wind maximum. Furthermore, easterlies near the Antarctic continent induce Ekman transport toward the coast, thus enhancing the horizontal divergence of Ekman transport. Consequently, the Southern Ocean plays a key role by closing the meridional overturning circulation (*Marshall and Speer*, 2012). Additionally, dense waters in the interior ocean are lifted by vertical mixing, induced by internal processes such as breaking internal waves (*Mashayek et al.*, 2017).

The ocean takes up heat at the surface, therefore, the largest amount of heat is stored in the upper ocean. In regions of deep water formation heat and carbon

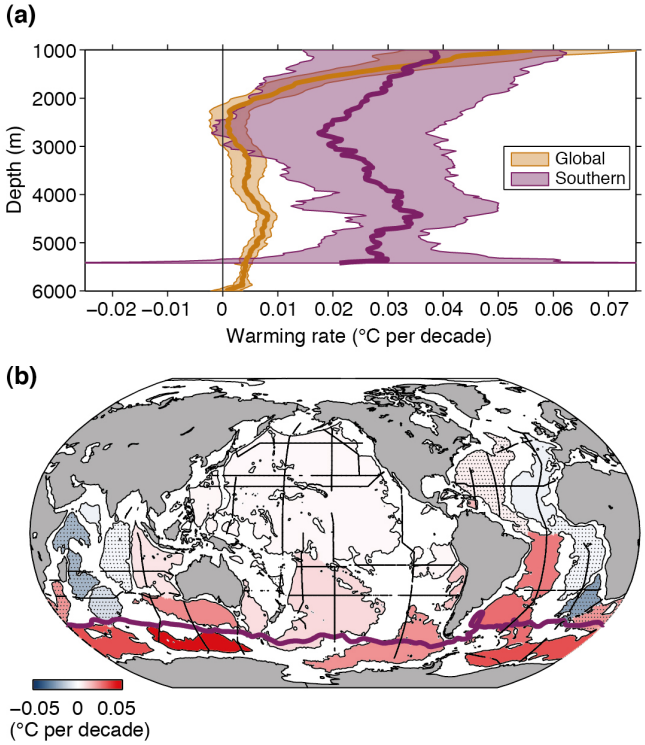

Figure 1.1: (a) Areal mean warming rates in °C per decade with 5 to 95% confidence intervals (shading). (b) Mean warming rates below 4000 m in °C per decade at 95% confidence interval (except stippled patches). Figure is taken from the IPCC Fifth Assessment Report (Data from *Purkey and Johnson* (2010)).

can be transported into the deep ocean and will be stored there for a long time; thus at the present state, the ocean reduces the rate of climate change. However, the ocean starts to warm up not only at the surface but first studies report on a warming of deep waters since the 1980s (*Purkey and Johnson*, 2010). Figure 1.1a, from the 5th IPCC (Intergovernmental Panel on Climate Change) report, shows areal mean warming rates per decade versus depth for the global and the Southern Ocean.

While in the global ocean the warming is mostly limited to the surface, the Southern Ocean experiences a strong warming throughout the whole water column with maxima at the surface and below 4000 m depth, indicating a deep ocean heat uptake. This is further illustrated by the mean warming rate below 4000 m (Figure 1.1b). A poleward migration of the Antarctic Circumpolar Current (ACC), which transports warm water, called Circumpolar Deep Water (CDW) at mid-depth, could partly be responsible for a warming in the upper layer. A southward shift of the ACC can also influence the bottom water properties by an increased

entrainment of CDW as dense water plumes, formed on the continental shelf of Antarctica, flow down the continental slope to ultimately contribute to AABW formation (*Couldrey et al.*, 2013).

The ocean warming has important implications for future sea level rise. The largest contribution comes from thermal expansion (thermosteric) but also fresh water/ mass input from glacial discharge was shown to cause rapid sea level rise along the Antarctic margins (*Rye et al.*, 2014). The latter, together with fresh water input by increased sea ice melting, can additionally impact the deep water formation locally; fresh surface water increases the stability of the water column, hence impeding deep convection. This in turn can lead indirectly to a warming of the bottom waters as the 'supply' of cold, dense water decreases. A freshening of AABW has been observed in the Ross Sea and off Adélie Land (i.e. *Aoki et al.* (2005); *Rintoul* (2007)), potentially linked to a freshening of the shelf waters (*Jacobs et al.*, 2002, 2010) resulting from enhanced basal melting of ice shelves along the West Antarctic Ice Sheet (*Pritchard et al.*, 2012; *Nakayama et al.*, 2014).

Ice shelves are the floating extensions of an ice sheet and have a stabilising effect by buttressing, i.e. their weight creates friction at the sea floor and bordering land masses. Submarine melting and iceberg calving are natural processes to balance the mass gain of an ice sheet via snow accumulation, however, ice shelf thinning and decreased buttressing will lead to an enhanced ice discharge(*Dupont and Alley*, 2005). Not only does the ocean impact the ice shelves, the ice shelves also have a large effect on the ocean. The glacial melt water significantly influences the ocean circulation on the shelf and contributes to water mass transformations (*Nicholls et al.*, 2009) and ultimately to AABW formation in some regions, thus leaving a global footprint.

The Antarctic ice sheet holds roughly 27 Mio km^3 of ice which is equivalent to $58\,m$ sea level (*Fretwell et al.*, 2013). Over the last two decades, the loss of Antarctic ice shelf volume and grounded ice have increased significantly (*Paolo et al.* (2015)), due to enhanced basal melt rates around Antarctica (*Rignot et al.* (2013), see Figure 1.2). As a result, the present day mass balance is negative (*Rignot et al.*, 2011). Most dramatic ice discharge occurrs along the West Antarctic Ice Sheet, in the Amundsen and Bellingshausen Seas (*Rignot et al.*, 2008; *Pritchard et al.*, 2012; *Nakayama et al.*, 2013; *Wouters et al.*, 2015). Here, the ACC hugs the continental slope and intrusions of warm mid-depth CDW onto the continental shelf are observed, creating a strong heat flux toward the ice shelves. Several

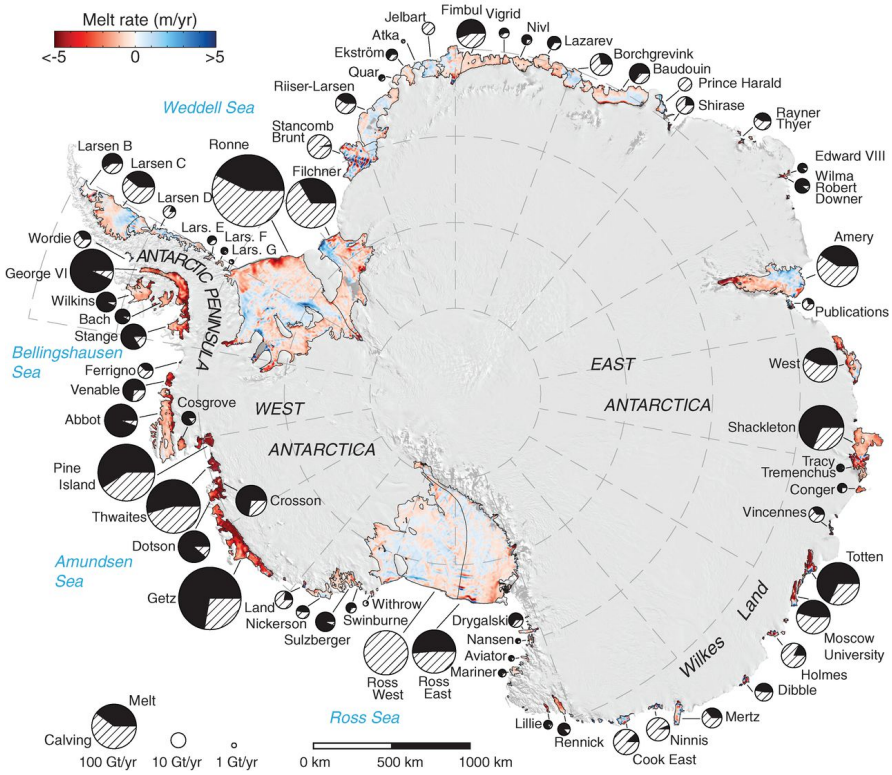

Figure 1.2: Figure from *Rignot et al.* (2013) (Their Fig. 1): Color coded from <-5 m/year (freezing) to >+5 m/year (melting) and overlaid on a 2009 Moderate Resolution Imaging Spectroradiometer mosaic of Antarctica. Ice-shelf perimeters in 2007 and 2008, excluding ice rises and ice islands, are thin black lines. Each circle graph is proportional in area to the mass loss from each shelf, in Gt/year, partitioned between iceberg calving (hatch fill) and basal melting (black fill).

studies show that this warm water enters the ice shelf cavities along the bottom, driving rapid basal melting (*Jacobs et al.*, 2011, 2013; *Dutrieux et al.*, 2014).

In these regions of Antarctica the atmospheric forcing in winter is not strong enough to erode the warm water from above, allowing a warm deep layer to persist, while a shallower winter mixed layer develops above. Other parts of Antarctica, such as the southern Weddell Sea, are governed by harsher atmospheric conditions in winter and convection to the bottom occurs in large coastal polynyas, due to enhanced sea ice production *Petty et al.* (2013, 2014). Here, warm water entering the continental shelf will be eroded or strongly modified during winter leading to lower ice shelf basal melt rates (*Rignot et al.*, 2013).

Today, the contributions to sea level rise from thermal expansion and melting continental ice in Greenland and Antarctica are roughly equal (*Church et al.*, 2013), however, if the mass loss from the ice sheets continues to accelerate, it will

be the main contributor of sea level rise in the future (*Rignot et al.*, 2011). The ocean will play the key role in determining the rate of retreat of the Antarctic Ice Sheet (*Golledge et al.*, 2017). Hence, it is essential to further study ocean-ice shelf interactions and the processes transporting warm water onto the continental shelf around Antarctica, ultimately posing a big threat to ice shelves.

This study will focus on the warm water transport onto the southern Weddell Sea continental shelf, where the Filchner Ronne Ice Shelf (FRIS), one of the largest ice shelves in Antarctica is located. Therefore, I will give a more detailed introduction to the Weddell Sea hydrography and circulation, relevant processes and FRIS in the following sections.

1.1 General circulation and hydrography of the Weddell Sea

The Weddell Sea (Figure 1.3) has long been regarded as the major source and export region of AABW (*Orsi et al.*, 1999; *Jullion et al.*, 2010)(Carmack1977, Orsi2002) followed by the Ross Sea, Adélie Land and Cape Darnely (*Meredith*, 2013). Even though the actual net production of AABW is under debate (*Couldrey et al.*, 2013; *Jullion et al.*, 2014), it is indisputable that the Weddell Sea plays a key role in the densification of water masses and in the closure of the lower limb of the meridional overturing circulation. The region undergoes a very strong seasonal cycle in sea ice, being almost fully covered in winter ($\approx 6 \cdot 10^6\, km^2$), followed by a significant retreat in summer ($\approx 1 \cdot 10^6\, km^2$)[1].

The circulation in the Weddell Sea is dominated by a cyclonic subpolar gyre, with a suggested double-cell structure (*Orsi et al.*, 1993; *Beckmann et al.*, 1999). The gyre is thought to be mainly driven by the strong westerlies over the Southern Ocean and easterlies close to the Antarctic continent, as results of the strong high pressure system over the continent. A baroclinic flow, induced by density gradients between the dense centre of the gyre and, in many areas, fresh continental shelf further enhances the general circulation (*Graham et al.*, 2013). The gyre boundaries are determined by the Antarctic continent in the south and the west and by topography in the north, where the South Scotia Ridge and the Southwest Indian Ridge are located, acting as a dynamical barrier, inducing strong oceanic

[1]Sea ice areas for summer and winter in the Weddell Sea taken from `https://nsidc.org/data/pm/weddell`

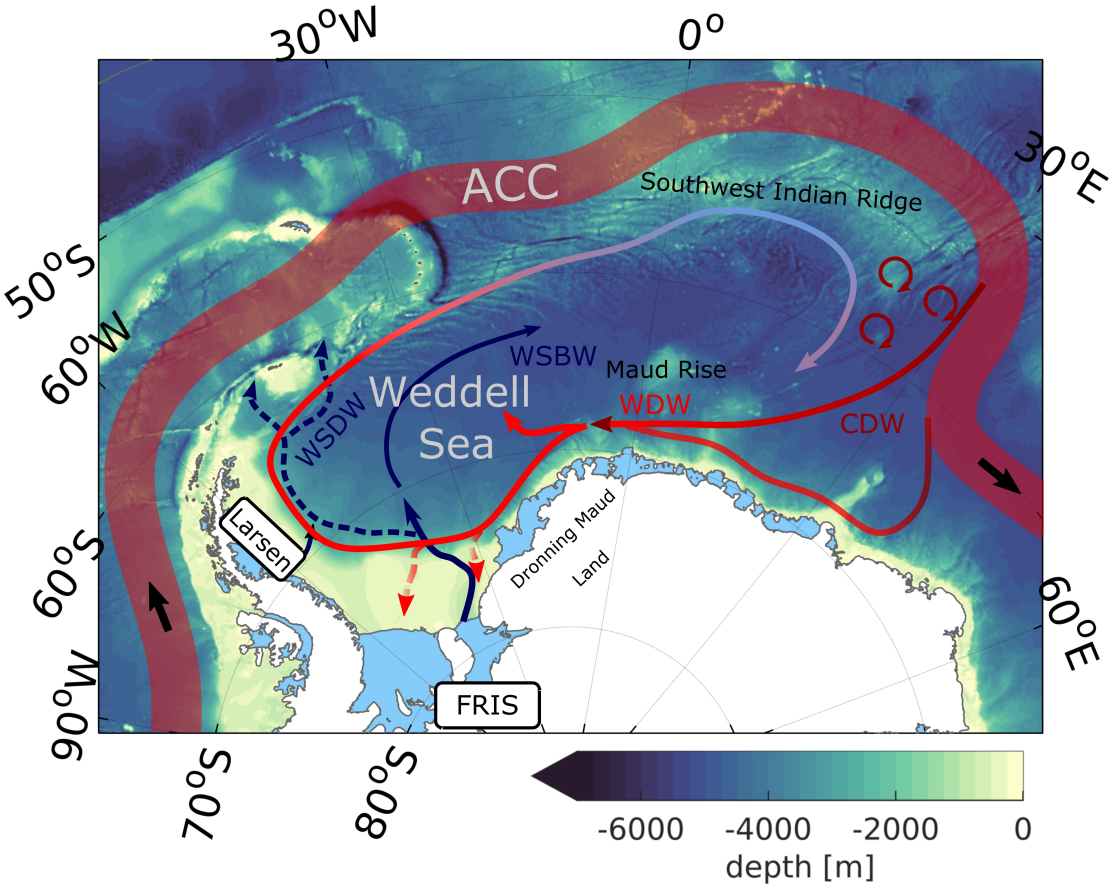

Figure 1.3: Bathymetric map of the Atlantic sector in the Southern Ocean, with focus on the Weddell Sea. Arrows represent a schematic of the Weddell Gyre circulation and pathways of present water masses. Relevant bathymetric features are labeled in black. Important Abbreviations have the following meaning: WSDW = Weddell Sea Deep Water, WSBW = Weddell Sea Bottom Water, WDW = Warm Deep Water, CDW = CDW, ACC = Antarctic Circumpolar Current, FRIS = Filchner Ronne Ice Shelf

fronts (*Orsi et al.*, 1995).

The eastern margin is less defined as no physical barrier is present. It is a highly dynamic region where an intense exchange between the ACC and the Weddell Gyre occurs and warm, saline CDW enters the gyre at around 30°E (*Gouretski and Danilov*, 1993; *Schröder and Fahrbach*, 1999; *Park et al.*, 2001). *Ryan et al.* (2016) suggest that the inflow occurs via two routes; one eddy-driven, shorter and one advective, longer pathway, both carrying CDW of different origin within the ACC. The mixture of these two will determine the properties of the warm water that eventually circulates within the gyre, which is called Warm Deep Water (WDW) within the Weddell Gyre. While the WDW flows westward along the

continental slope, it gradually cools and freshens. Thus, the continental shelf in the Weddell Sea, does not come into direct contact with warm ACC waters, in contrast to the western side of the Antarctic Peninsula. The fresher and cooler WDW recirculates within the gyre and forms the so called cold regime (*Gordon and Huber*, 1984; *Schröder and Fahrbach*, 1999) as the northern branch of the gyre, which then mixes with the new CDW entering the gyre east of the prime meridian.

In the southwestern and western Weddell Sea, dense waters are produced on the broad continental shelf via strong sea ice formation in the coastal polynyas and active interaction with ice shelves (*Orsi et al.*, 1999). These waters ultimately form AABW when they cascade down the continental slope (*Gill*, 1973; *Foster and Carmack*, 1976; *Foldvik*, 2004). Within the Weddell Sea one differentiates between two different dense water masses; the Weddell Sea Bottom Water (WSBW) comprises the coldest and densest water, which is primarily produced on the southern Weddell Sea continental shelf where FRIS is located (see Figure 1.3). Weddell Sea Deep Water (WSDW) is warmer and lighter due to either entrainment of WDW into the cascading dense shelf waters or direct mixing of WDW with WSBW below (*Gordon et al.*, 2001). The continental shelf in front of the Larsen Ice Shelves on the eastern side of the peninsula is the second main production region. Waters originating from here have a distinct signature and are fresher/lighter than the equivalent from the southern shelf (*Fahrbach et al.*, 1995; *Huhn et al.*, 2008; *Gordon et al.*, 2010; *van Caspel et al.*, 2015). The production rates off LIS are smaller, however, the lighter WSDW likely contributes more to the global AABW as it can more easily exit the basin through shallower passages in the north, such as the Orkney Passage (*Naveira Garabato et al.*, 2002; *Schodlok et al.*, 2002), while the densest WSBW is trapped in the deep basin.

1.2 Antarctic slope front and cross-shelf exchanges

The Antarctic Slope Front (ASF) separates the offshore Circumpolar Deep Water (or the Weddell Sea equivalent WDW) from the colder and mostly fresher shelf waters and is a nearly persistent feature around the Antarctic continent (*Heywood et al.*, 2004). The front is of climatic importance, by controlling warm water transport onto the continental shelf and, ultimately, toward ice shelves around Antarctic. Onshore Ekman transport around the Antarctic margins deepens the

coastal isopycnals *Sverdrup* (1954); *Gill* (1973) and creates horizontal density gradients, that in turn drive the westward flowing Antarctic Slope Current (ASC), which accounts for roughly 50% of the total Weddell Gyre transport in the south-eastern Weddell Sea (*Heywood et al.*, 1998). The ASC transport shows a seasonal cycle (*Graham et al.*, 2013), which is suggested to be controlled by the Ekman drift induced by the local wind field (*Núñez-Riboni and Fahrbach*, 2009; *Mathiot et al.*, 2011). In areas where the continental shelf is very narrow, the ASC merges with the Antarctic Coastal Current (ACoC), which is generally found over the continental shelf (*Heywood et al.*, 1998). For simplicity, there will be no distinction between the ACoC and the ASC in this study, and the current will be referred to as ASC solely. Due to the sloping isopycnals, the WDW core in the Weddell Sea is located deeper near the continental slope compared to the open ocean (*Fahrbach et al.*, 1994). In regions of dense water formation on the continental shelf, the ASF depicts a characteristic v-shape structure, as isopycnals from denser mid-depth water off-shelf connect to the dense isopycnals on the shelf (*Gill*, 1973; *Jacobs*, 1991).

Nøst et al. (2011) suggest that the wind-driven Ekman overturning in the upper layer is balanced by a deeper counteracting eddy-driven overturning circulation, which acts to flatten the isopycnals (see also *Zhou et al.* (2014)). Vertically diverted isopycnals create available potential energy (APE) and baroclinic instabilities arise along the front. Eddies transfer this APE to eddy-kinetic energy (EKE) and generate a less energetic state of the water mass. The importance of eddies for on-shore transport of WDW was pointed out by *Stewart and Thompson* (2015). The described processes induce mixing along the pycnocline and a slightly cooler and fresher version of WDW is formed, called Modified Warm Deep Water (MWDW). It is this water mass that eventually enters the continental shelf. *Hattermann et al.* (2014) showed that eddy-resolving simulations are needed in order to properly represent frontal dynamics, which is crucial to correctly model the on-shelf transport of WDW and, ultimately, assessing the influence on the ice shelf.

Topographic features, such as cross-shelf cutting troughs, can additionally create an on-shelf flow of warm water and channel it toward ice shelves (*Klinck and Dinniman*, 2010; *St-Laurent et al.*, 2013). In the Weddell Sea such a trough is found on the southern continental shelf, which extends all the way from the shelf break to the grounding line of FRIS. The broad continental shelf in front of FRIS

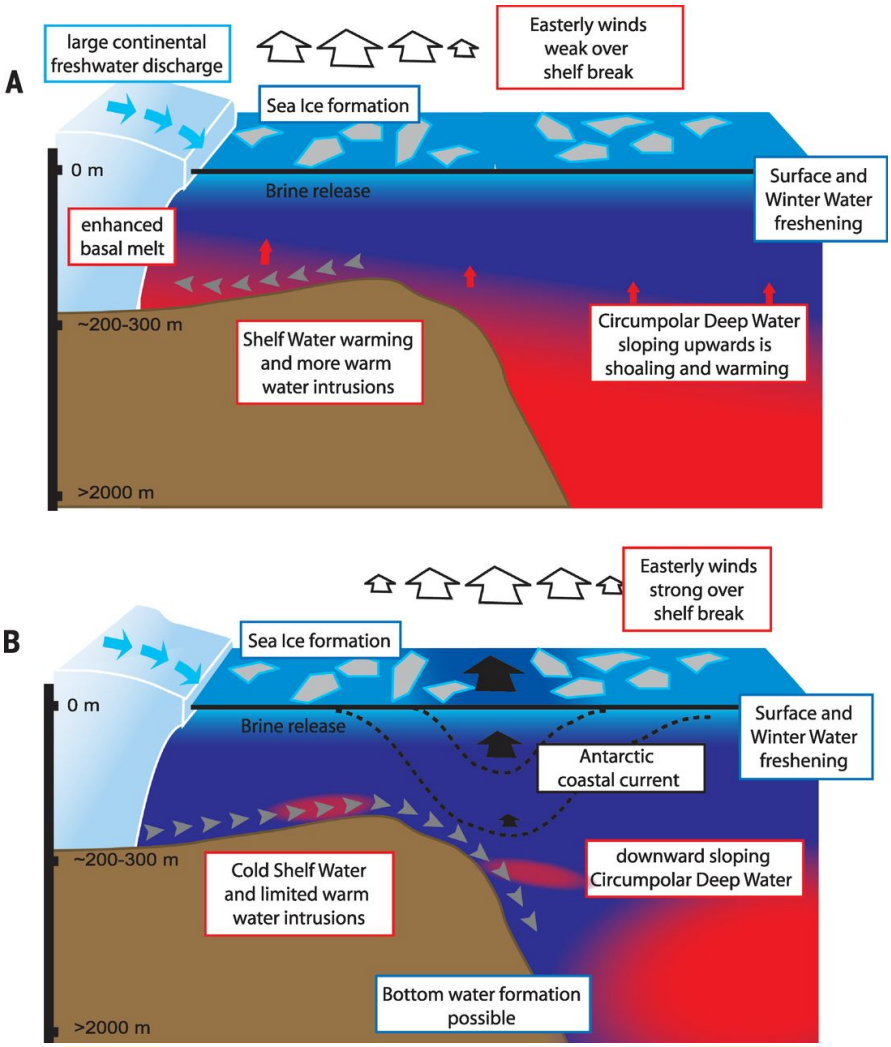

Figure 1.4: Schematic of warm water (e.g. Amundsen Sea) and cold water (e.g. Weddell Sea) continental shelf from *Schmidtko et al.* (2014) (their Fig. 4). The Weddell Sea equivalent of Circumpolar Deep Water is called Warm Deep Water (WDW).

is governed by strong winter convection, indicated by deep modelled mixed layer depths (*Petty et al.*, 2013, 2014) and dense water production due to ocean-ice shelf interaction. Both processes, up to now, protect the ice shelf from a permanent warm inflow. While a change to strong warm inflow along the Filchner Trough is suggested to be possible in a future warming climate (*Hellmer et al.*, 2012, 2017; *Timmermann and Hellmer*, 2013), there are regions around Antarctica, where observations show, already today, a direct flow of CDW on the continental shelf reaching the ice shelves (e.g. *Moffat et al.* (2009); *Nakayama et al.* (2013)).

While coastal troughs can regionally play an important role in the on-shelf

transport of warm water, it was shown by *Schmidtko et al.* (2014) that, generally, regions, where warm intrusions are observed, are governed by weaker easterly winds above the shelf break, which allows a shoaling is the isopycnals (see Figure 1.4a). In contrast, stronger easterly winds suppress the warm water at the shelf break, therefore, limiting warm water intrusions (see Figure 1.4b), as observed in the Ross and Weddell Sea.

Another important difference between the polar gyres (Ross and Weddell Gyre) and, e.g., the western side of the Antarctic peninsula is, that CDW, with temperatures above 1.5°C, is significantly warmer than its modified derivatives within the gyres (WDW in Weddell Gyre), which typically range between 0°C and 1.5°C. In the southern Weddell Sea, it is again a modified version (MWDW) with temperatures around −1°C, which enters the shelf. Therefore, the potential heat that can be transported to ice shelves is lower within the polar gyres.

Nevertheless, the interest in the southern Weddell Sea has widened in recent years from the focus being mainly on the cold outflow from beneath FRIS, to the warm inflow along the eastern flank of the Filchner Trough.

1.3 The Filchner Ronne Ice Shelf

FRIS is, by volume, the largest ice shelf in Antarctica and comprises an area of $450,000\,\mathrm{km}^2$ (*Fox et al.*, 1994), which is only exceeded by the Ross Shelf. Figure 1.5 shows a map of the region and the main circulation, as assumed presently. The Filchner Ice Shelf (FIS) in the east and Ronne Ice Shelf (RIS) in the west are separated by Berkner Island but are connected via a passage south of the island. FRIS is located on a wide continental shelf that has a shelf break of roughly 400m depth and deepens towards the grounding line. Prominent bathymetric features are the Filchner and Ronne Trough, where the major water mass exchange across the ice shelf front occurs. The Filchner Trough runs from the shelf break all the way to the grounding line of FIS, thus creating a direct connection of the open-ocean with the cavity. It has a sill depth of 600 m and deepens toward the cavity to roughly 1500 m depth.

[2]

[2]The following part of 1.3 is part of a publication in the *Journal of Geophysical Research* with the title *Seasonal cycle of hydrography on the eastern shelf of the Filchner Trough, Weddell Sea, Antarctica (Ryan et al., 2017).*

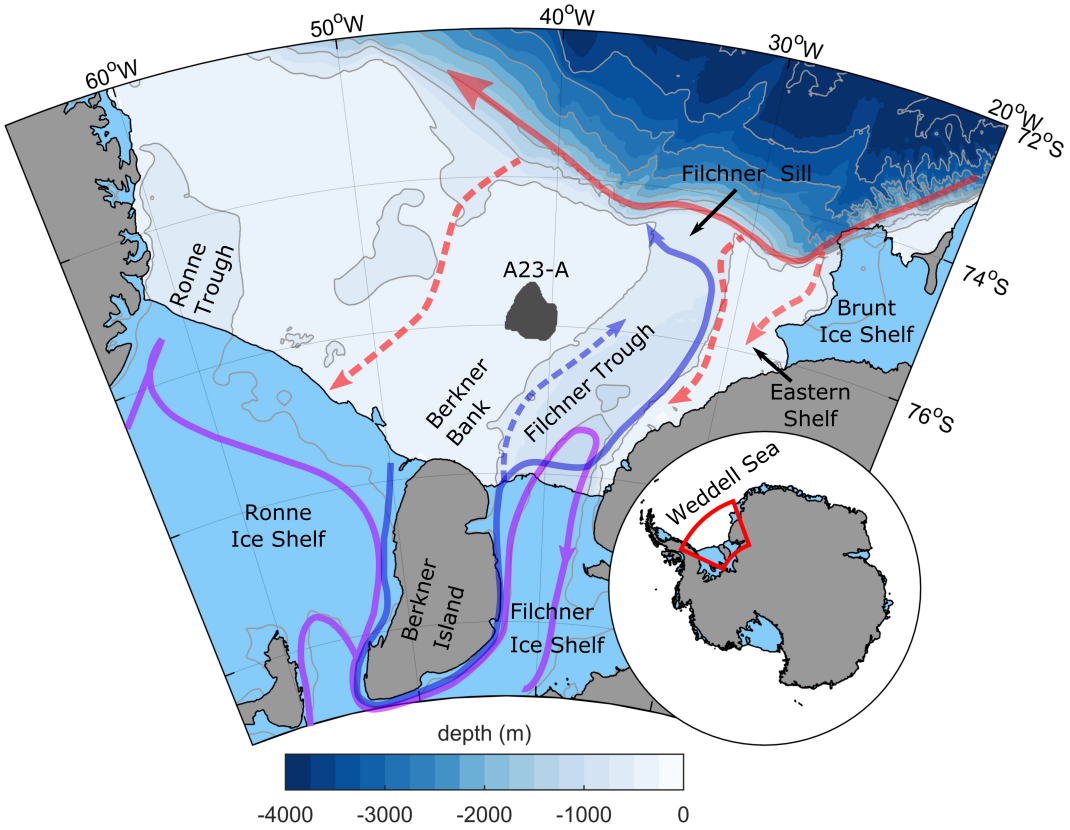

Figure 1.5: Circulation underneath FRIS after *Nicholls et al.* (2009). Circulation in Filchner Trough adjusted to results from *Darelius et al.* (2014a). Dashed grey arrows indicate flow of MWDW onto shelf. Blue and red represent ISW from different origin. Figure modified from *Ryan et al.* (2017). Bathymetry contours (thin grey) are given in 500 m intervals using RTopo2 (*Schaffer et al.*, 2016).

The role of the Filchner Trough for the FRIS region is twofold. Firstly, it is the only area where water with potential temperatures below the surface freezing point ($\theta < -1.9°C$), known as Ice Shelf Water (ISW, *Foldvik and Gammelsrød* (1988)), can leave the shelf area and contribute to the deep water formation. Secondly, with the sill being deeper than the actual shelf break the trough can act as a conduit for MWDW, flowing along the continental slope, southward towards the ice shelf due to the conservation of potential vorticity.

The ISW outflow along the Filchner Trough has long been of interest (*Foster and Carmack*, 1976; *Foldvik*, 2004; *Nicholls et al.*, 2009). ISW originates from High Salinity Shelf Water (HSSW), which is formed on the continental shelf west of the trough during winter when the water column becomes increasingly dense from surface cooling and brine release during sea ice formation. Being the densest water mass on the shelf it enters the sub-ice shelf cavity mainly via the Ronne

Trough (*Nicholls et al.*, 2003). Even though HSSW has potential temperatures around the surface freezing point ($\theta \sim -1.9°C$), it can melt ice under increased pressure. Hence, it interacts with the ice shelf base (*Gade*, 1979) and forms ISW, which leaves the FRIS cavity and the continental shelf via the Filchner Trough (see Figure 1.5). Once the ISW crosses the sill, it enters the open ocean, where it contributes to the dense water formation (*Foldvik et al.*, 1985a; *Foldvik*, 2004). *Darelius et al.* (2014a) show from hydrographic observations and ocean model results that ISW flows towards the sill on the eastern slope of the trough, which had been hypothesized to be concentrated along the western flank (*Nicholls et al.*, 2009). At the sill the ISW flows westward where it then leaves the depression and descends the continental slope. The outflow is geostrophically balanced and analytical (*Kida*, 2011) and numerical (*Wang et al.*, 2012) models suggest that its strength is determined by the density difference between the dense outflow and the off-shelf density. However, velocity time series at the sill do not show a seasonal cycle in the outflow velocity (*Darelius et al.*, 2014b).

The bottom circulation in the trough was suggested to be cyclonic (*Carmack and Foster*, 1975) and comprises waters that are too dense to cross the sill. These can be dense ISW but also admixtures of HSSW, formed during winter on the Berkner Bank, that can enter the trough along the bottom on the western side. This can cause seasonal and interannual hydrographic variability within the trough (*Nøst and Østerhus*, 1998; *Darelius et al.*, 2014b).

While the dense outflow remains an important process, the inflow of MWDW has become a focus of interest in recent years. *Hellmer et al.* (2012) and *Timmermann and Hellmer* (2013) suggest from model results that in a future warming climate MWDW may enter the Filchner trough via a redirected coastal current, which eventually fills the trough and reaches into the ice shelf cavity, causing very high basal melt rates below FRIS, similar to warm inflow currently observed in the Amundsen Sea (*Arneborg et al.*, 2012).

Darelius et al. (2016) for the first time observed MWDW near the Filchner Ice Front during a one-year long mooring deployment in 2013. They suggest a strong correlation between the inflow and easterly winds in the region. Long-term weak easterly winds will lift the thermocline at the shelf break, enabling the MWDW to cross the sill, while local storm events will set up a strong coastal current to transport the warm water close to the ice shelf front. However, they find no evidence of the warm water entering the ice shelf cavity as the observed signal at

the mooring is flowing to the north along the eastern flank of the trough (*Darelius et al.*, 2016).

At the Filchner Sill Conductivity-Temperature-Depth (CTD) data from tagged Weddell seals show the inflow of warm water onto the shelf along the 400 m isobath during summer (*Foldvik et al.*, 1985b; *Årthun et al.*, 2012). Additionally, *Årthun et al.* (2012) use mooring data from 2007-2009 located at the eastern side of the sill. The results show interannual variability regarding the start and the duration of the inflow, which they suggest to be connected to the surface wind stress and a related up-/downward movement of the WDW core along the continental slope. Modelling studies show the importance of meso-scale eddies for the transport of MWDW onto the continental shelf across the ASF (*Nøst et al.*, 2011; *Stewart and Thompson*, 2016) or via coastal troughs, such as the Filchner Trough (*St-Laurent et al.*, 2013; *Daae et al.*, 2017).

[3]

1.4 Sea ice in the Weddell Sea

Sea ice plays an important role in high-latitudes by modulating the ocean-atmosphere interaction, such as air-sea heat fluxes and momentum exchange. Sea ice formation and melting influence the upper ocean stratification (*Martinson and Iannuzzi*, 1998). It was shown that seasonal and interannual variability of sea ice can impact water mass properties significantly in the Weddell and Ross Sea (*Thorsten et al.*, 1998; *Jacobs and Comiso*, 1989; *Jacobs et al.*, 2002; *Petty et al.*, 2013).

The Weddell Sea undergoes a strong seasonal cycle in sea ice. Figure 1.6 shows mean sea ice concentration maps from 2000 to 2017 for February (minimum) and September (maximum). Furthermore, time series of the areal mean concentration for the whole Weddell Gyre and the Filchner region are plotted (c). In winter the Weddell Sea is almost completely covered by sea ice with a mean concentration over 80%; open water is only found in few coastal polynyas, e.g. in front of the Fimbul and Ronne Ice Shelves. Highest concentrations ($> 98\%$) are found in the southwestern Weddell Sea and along the Antarctic Peninsula. This region remains almost fully ice covered during summer, while the northeastern corner of the gyre is completely ice free.

The continental shelf in front of FRIS is governed by heavy sea ice all year

[3] The part of publication (*Ryan et al.*, 2017) finishes here.

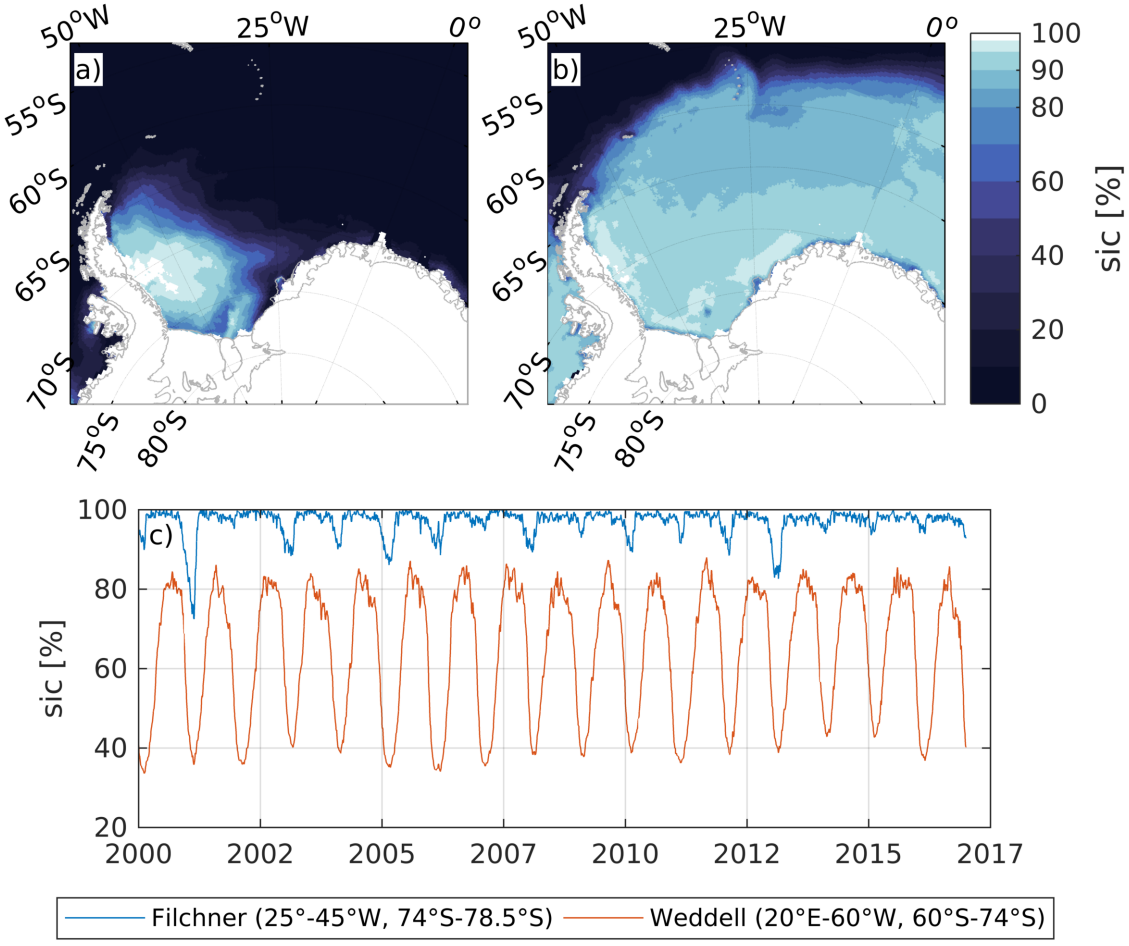

Figure 1.6: Multi-year mean (2000-2017) summer (a) and winter (b) sea ice concentration in the Weddell Sea. c) Time series of areal mean sea ice concentration. Data available at `ftp://ftp-icdc.cen.uni-hamburg.de/asi_ssmi_iceconc/ant/`.

around, however, large polynyas can open up in front of Ronne and near the Brunt Ice Shelf. Mean summer ice coverage reveals a narrow band of thick ice cover north of Berkner Island, along the western flank of the Filchner Trough. This band is caused by a giant grounded ice berg (A23-A, see Figure 1.5), which is the remainder of three icebergs (A22, A23, and A24) that separated from the FIS front in 1986 (*Ferrigno and Gould*, 1987). Hence, the westward sea ice drift in the region is blocked by the ice berg, resulting in a dense ice field, which prohibited oceanographic measurements on the western side of the Filchner Trough in the

last decade.

While in the Weddell Sea the maximum sea ice concentration is rather constant, the minimum concentration seems to have an interannual cycle with a period of 5 to 7 years, e.g. year 2006, 2011 and 2016 show a minimum concentration. Antarctic sea ice is suggested to be influenced by large scale climate modes, such as El Niño-Southern Oscillation (ENSO), where less sea ice in the Pacific sector and more sea ice in the Weddell Sea are associated to El Niño and vice versa during La Niña (*Rind et al.*, 2001; *Yuan*, 2004). The Filchner region also shows strong interannual variability in the minimum concentration. In some years, as for example in 2001 and 2013 the mean ice coverage is very low. In other years, such as 2002 and 2007, the concentration remains almost 100% in summer. The effect of sea ice variability on the cross-shelf exchange in the southern Weddell Sea is not understood but could play an important role. For example, sea ice coverage was very low in 2013, when *Darelius et al.* (2016) observed a strong warm inflow event along the eastern flank of the Filchner Trough.

1.5 Objectives and Contents

The southern Weddell Sea remains a heavily undersampled region due to its remoteness, heavy sea ice cover and hazardous atmospheric conditions, which leaves several research questions open and requires continuous field measurements and, at the same time, improvement of ocean models. This thesis has the following objectives:

- Observations at the shelf break show a seasonal flow of MWDW onto the continental shelf at the eastern side of the Filchner Sill (*Årthun et al.*, 2012) and warm pulses have been observed for the first time close to the FIS front in 2013 (*Darelius et al.*, 2016). However, little is known about the seasonal and interannual variability along the eastern flank of the Filchner Trough. What is the seasonal variability of the MWDW inflow downstream of the shelf break? What are the main processes involved?

- With exponentially increasing computational power and data storage capabilities, more powerful ocean models are being developed. In this thesis, a global configuration of the Finite Element Sea Ice - Ocean Model (FESOM), which allows a local mesh refinement. How well is the Weddell Gyre circu-

lation represented in low and high resolution simulations and how does it influence the cross-shelf exchange in the southern Weddell Sea?

- How do the model results compare to observations and can the model reproduce a realistic flow of MWDW onto the continental shelf? If so, what is the interannual variability and can MWDW enter the FIS cavity via the Eastern Shelf?

This thesis is structured as follows: Chapter 2 describes data and methods an consists of two parts: First, the oceanographic fieldwork, relevant for this thesis and all used data sets are described. Furthermore, applied methods are introduced and some theoretical background is provided. Second, FESOM and its governing equations are introduced. The newly compiled horizontal, finite-element mesh is described and its improvements compared to a previously used, coarser mesh, are highlighted. Furthermore, an overview of the used forcing, the model set-up a and the model simulations is given. In Chapter 3, observations, comprising ship-based, moored and seal-tag hydrographic data as well es oxygen isotopes, are used to analyse the Filchner Trough hydrography. Particular focus lies on the seasonal hydrography along the eastern flank of the Filchner Trough, derived from mooring data. Chapter 4 is used to perform a model assessment. Particular interest is given to the Weddell Gyre hydrography and circulation to investigate what effect increased resolution has and whether the model is suitable for an analysis of the cross-shelf exchange at the southern Weddell Sea continental shelf. A model experiment, where the hydrography over the continental slope upstream of the Filchner Trough is restored, is presented in Chapter 5. The modelled inflow of MWDW is discussed with respect to its seasonal and interannual variability. Finally, concluding remarks and an outlook for future work are given in Chapter 6. Complementary Figures with the aim to give additional insight or support to arguments are presented in the Appendix A.

The major part of Chapter 3 (section 3.2) has been published in the *Journal of Geophysical Research: Oceans* under the title *Seasonal cycle of hydrography on the eastern shelf of the Filchner Trough, Weddell Sea, Antarctica (Ryan et al., 2017).* Introduction and Data and Methods sections from the paper are integrated in Chapter 1 and Chapter 2 in this thesis. The beginning and end of the according passages are marked by footnotes.

2. Data and Methods

2.1 Oceanographic fieldwork

In this thesis, a number of different observational data sets are used and analysed, which will be described in the following. Section 2.1.2 is part of my publication (*Ryan et al.* (2017), Data and Methods). Furthermore, I will give an overview and introductions to used methods.

2.1.1 Ship-borne hydrographic data

Conductivity-Temperature-Depth

Hydrographic data was obtained during two research cruises with *RV Polarstern* in 2013/2014 (PS82) and 2015/2016 (PS96) by lowering Conductivity-Temperature-Depth (CTD) sondes from the ship. The station positions are shown in Figure 2.1. The CTD sensors are typically attached to a rosette, equipped with 24 12l-bottles, which is veered out to the sea floor on a conductive cable, transmitting the recorded data to a screen in real-time. This allows to stop the instrument at desirable depths, were the water bottles are closed. Water samples are important to calibrate sensors but are also used for other measurements, such as trace gases or isotopes. Final products are continuous profiles of temperature, salinity, dissolved oxygen and other parameters, depending on which sensors where attached. The conductivity and temperature sensors were additionally calibrated before and after the cruise by Seabird Electronics, leading to accuracies of 0.001°C for temperature and 0.003 for salinity (*Knust and Schröder*, 2014; *Schröder*, 2016).
Furthermore, CTD data from a *RSS Ernest Shackleton* cruise (ES060) (*Darelius and Fer*, 2015) in 2013 are used to compare temperature sections at 76°S from different years, in order to investigate the warm inflow along the eastern flank of the Filchner Trough.

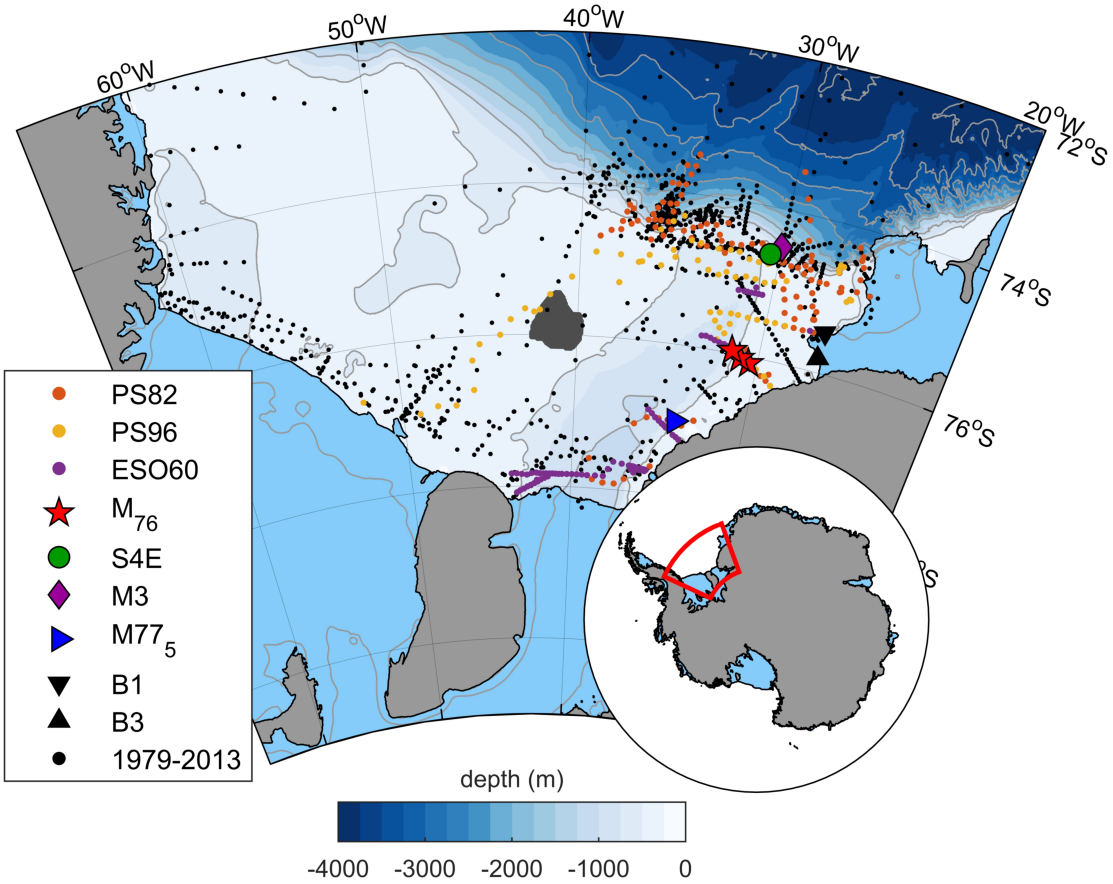

Figure 2.1: Station map of CTD-data obtained during PS82 (orange dots) and PS96 (yellow dots), mooring positions and available historical CTD-stations (see legend). Bathymetry contours (thin grey) are given in 500 m intervals using RTopo2 (*Schaffer et al.*, 2016)

Oxygen isotopes

In regions where the ocean interacts with glaciers, oxygen isotopes proof very useful, especially the ratio of oxygen isotope 18 (O^{18}) to oxygen isotope 16 (O^{16}). Precipitation is mostly depleted in the heavier O^{18} due to fractionation processes during evaporation and condensation. Accordingly, the same applies for Antarctic snow and ice (meteoric), hence, the ratio is widely used to analyse the melt water influence in the ocean. Particularly, the salinity-isotope relation can give information about several hydrological processes; generally a linear relationship is found, whose slope ,however, depends on regional climate (*Srivastava et al.*, 2007; *Tiwari et al.*, 2013).

Water samples for $\delta^{18}O$ measurements have only been taken during PS96 and were processed with a Finnigan DELTA plus mass spectrometer at the ILTS lab-

oratory, Hokkaido University. The process determines the stable oxygen isotope ratio of water with respect to Vienna Standard Mean Ocean Water (VSMOW) and is then expressed as:

$$\delta^{18}O = \left(\frac{\left(\frac{^{18}O}{^{16}O}\right)_{sample}}{\left(\frac{^{18}O}{^{16}O}\right)_{vsmow}} - 1 \right) \times 1000 \quad (‰) \tag{2.1}$$

The measurements can be very sensitive to the equipment and technique used. In

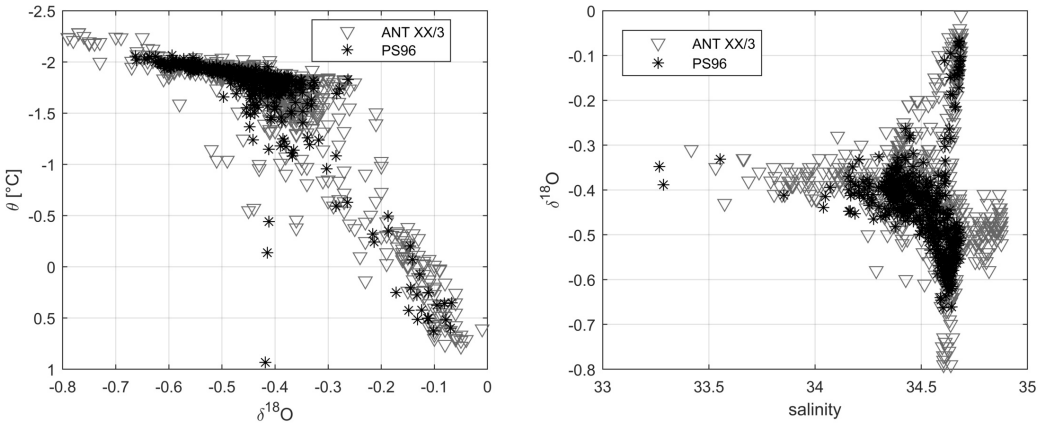

Figure 2.2: Potential temperature (left) and salinity (right) vs. δ^{18}O from PS96 (black) and ANTII/3 (grey)

my thesis, I will compare our data with historical data from the Polarstern expedition *ANTXII/3* in 1995 in order to analyse ISW properties within the Filchner Trough and possible origins. In Figure 2.2a oxygen isotope data of both cruises is plotted against potential temperature. For ISW, there is an almost linear relationship of the two parameters and the distribution agrees well for both cruises. It becomes very clear that the lowest values are associated with water below the surface freezing point, hence ISW, which contains glacial melt water. Therefore, δ^{18}O serves as an excellent tracer for ISW and I conclude that, even though measured differently, data from both cruises are comparable and can be used for the analysis of ISW. Similarly, a very good agreement is found in the isotope-salinity relation between both datasets (Figure 2.2b).

2.1.2 Moored measurements [1]

Three moorings have been deployed on the continental shelf at the eastern flank of the Filchner Trough at 76°S during a cruise with *RV Polarstern* in summer 2014 (PS82, *Knust and Schröder* (2014)) and successfully recovered 2 years later (PS96, *Schröder* (2016)). The deepest mooring was located at the slope with a water depth of about 600 m ($M_{31.5W}$ (*Schröder et al.*, 2014a)), and two moorings on the Eastern Shelf at roughly 430 m depth (M_{31W} (*Schröder et al.*, 2014b) and $M_{30.5W}$ (*Schröder et al.*, 2014c)); see Table 2.1 and the map (Figure 1.3) for locations. Instruments cannot be deployed shallower than 300 m in this region due to the presence of large icebergs. The nomenclature has been chosen such that the subscripts indicate the longitude of the mooring position. All moorings were equipped with two Microcats (SBE37), measuring temperature, salinity and pressure in an hourly interval. Additionally, a Recording Current Meter (RCM) of type RCM11 was attached just below the lower Microcat 20 m above the bottom (see Table 2.1), with a sample rate of 2 hrs. All instruments, except the RCM at $M_{31.5W}$ which failed after 8 months, have recorded data for the complete time period of two years. The instruments were calibrated and the data processed after the cruise. The nominal depth of the instruments has been adjusted to the pressure records and salinity has been recomputed with the corrected depth. Directions from the compass were corrected by the magnetic inclination. These mooring data are the centerpiece of our study and allow the definition of a seasonal cycle on the Eastern Shelf.

Records from a mooring array deployed across the eastern flank of the Filchner Trough at 77°S are included in the study (*Darelius et al.*, 2016; *Darelius and Fer*, 2017), in order to assess the robustness of our presented seasonal cycle in time and space. The mooring used was deployed at the 500 m isobath in January 2013 during the ES060 cruise and recovered in January 2014 during PS82.

Results from the new mooring data presented here, are compared to data from a mooring (S4E) deployed between 2007 and 2009 at the shelf break (74.62°S, 30.5°W) on the eastern side of the Filchner sill (*Årthun et al.*, 2012). Temperature was recorded with 5 sensors, evenly spread in the lower 400 m and recording at a 5 minute interval. A mean annual time series was computed on a daily basis by

[1] This section is part of a publication in the *Journal of Geophysical Research* with the title *Seasonal cycle of hydrography on the eastern shelf of the Filchner Trough, Weddell Sea, Antarctica (Ryan et al., 2017).*

averaging data of the same day of the year for the three years, i.e. the temperature at day 100 will be the average of the day 100 in 2007-2009. As the time period does not cover the complete three years, some values in the resulting time series only average over two records. This analysis allows us to link our observations to the processes at the shelf break, where the flow onto the continental shelf and its properties are controlled.

In addition, we use data from mooring M3 (74.5°S, 30.015°W, *Jensen et al.* (2013); *Fer* (2016)), which was located at the shelf break at roughly 700 m depth east of the Filchner sill (see Table 2.1 for details). Two moorings (B1, B3) deployed in the vicinity of the Brunt Ice Shelf in 2003 are used to obtain information about the seasonality of the coastal current. Both moorings were displaced by ice bergs, however, stayed within the coastal current. For further information see the cruise report of JR097 (*Nicholls*, 2005).

Daily SSMI-SSMIS (ASI algorithm) sea ice concentration data, originally computed at and provided by IFREMER, Brest, France, were obtained as a 5-day median-filtered and gap-filled product from the Integrated Climate Data Center in Hamburg (ICDC), Germany.

Table 2.1: Mooring Instrumentation: T is temperature, C is conductivity, P is pressure, V is horizontal velocity, and W is vertical velocity

Mooring	Latitude/Longitude	In/Out	Bottom Depth (m)	Height (mab)	Parameter
$M_{30.5W}$	76° 05.47′S	5 Jan 2014	450	118	T, C, P
	030° 28.19′W	21 Jan 2016		20	T, C, P, V
M_{31W}	76° 02.75′S	5 Jan 2014	456	118	T, C, P
	030° 59.65′W	22 Jan 2016		20	T, C, P, V
$M_{31.5W}$	75° 57.71′S	5 Jan 2014	580	265	T, C, P
	031° 28.92′W	22 Jan 2016		20*	T, C, P, V
M3	74°30.63′S	13 Feb 2009	725	10	T, C
(*Jensen et al.*, 2013)	030° 09.90′W	9 Feb 2010		25	T, V
				77, 154, 360	T, C, P
				102, 128, 257	T
				123:4:199	V, W
				205, 305	T, P
$M77_5$	77° 0.48′S	2 Jan 2013	490	25, 110, 160	T
(*Darelius et al.* (2016),	034° 03.06′W	09 Jan 2014		10, 85	T, C
their M_{NORTH})				19:4:119	V
S4E			469	10, 50, 100, 150[c], 200	T
(*Årthun et al.*, 2012)					
B1	75°27.911′S	7 Feb 2003	228	40, 140	V
	026°50.477′W	24 Feb 2005			
B3	75°48.734′S	6 Feb 2003	329	40, 135, 215, 255	V
	026°51.953′W	24 Feb 2005			

* Current meter stopped recording after 8 months (26 Aug 2014).

[c] Sensor malfunctioned shortly after deployment.

[2]

2.1.3 CTD-equipped seal data

In remote areas like the Weddell Sea, where sea ice in winter serves as an additional impediment, marine mammals, such as Weddell and elephant seals, have become important assistants for the oceanic community. They often travel thousands of kilometres and continuously dive to great depth along their way. Equipping them with light weight-weight devices allows biologist to study their foraging behaviour, while oceanographic data is collected at the same time. During PS82 (2014) five Weddell seals were tagged in the south eastern Weddell Sea (*Bornemann et al.*, 2015). The data is part of the MEOP (Marine Mammals Exploring the Oceans

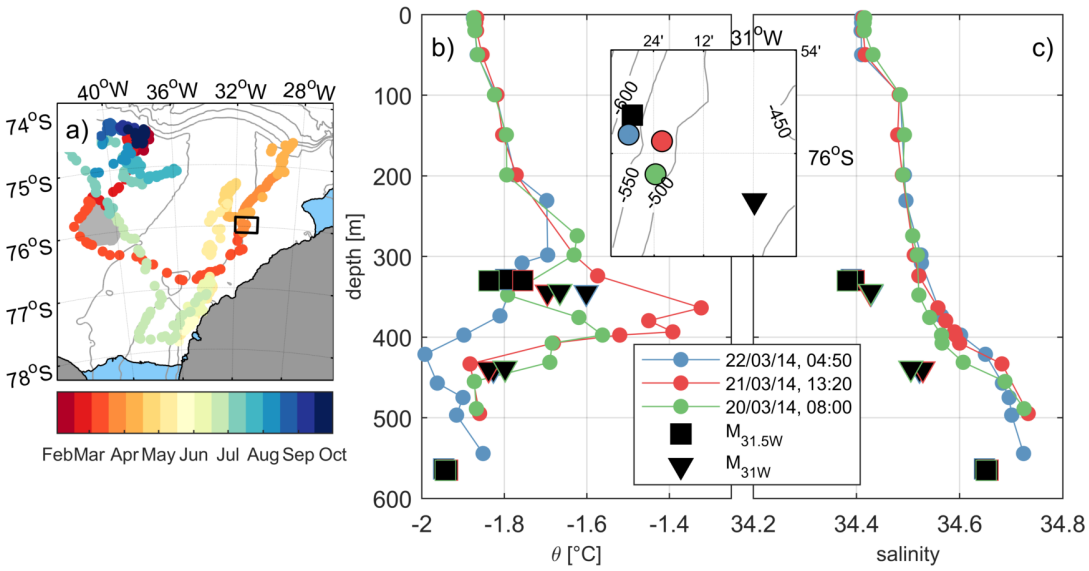

Figure 2.3: a) Distribution of profiles obtained by seal f04 in 2014. The colour shading gives the time of the year. Bathymetry is shown in thin grey lines with 500 m interval. The black square indicates the boundaries of the small map. b) Profiles of potential temperature at the three closest positions to the $M_{31.5W}$ (square) and M_{31W} (triangle) mooring. Records from microcats at two levels at each mooring are marked with the respective marker. The colour frame around the marker indicates the point in time closest to the seal profile. c) same as b) but for salinity.

Pole to Pole) project which maintains a quality-controlled database (*Treasure et al.*, 2017). They give a nominal accuracy 0.005 °C for temperature and 0.02 for

[2]The part of publication (*Ryan et al.*, 2017) finished here.

salinity (*Boehme et al.*, 2009). Due to a size limitation of the seal loggers, data storage has to be minimized and no continuous profiles are available. Instead, a mean profile over a 6-hours period is obtained (For further details see *Boehme et al.* (2009)).

One diligent seal (f04) sampled the eastern and western part of the Filchner Trough between February and September 2014 (see Figure 2.3a) and recorded temperature and salinity. It was tagged on the western side of the trough, afterwards travelled around the big iceberg A23-A to cross the trough and proceeded north along the eastern side of the trough toward the shelf break. Then it travelled back south south along the eastern flank, crossed the trough again and arrived at its starting location in spring. On its way the seal passed close by mooring $M_{31.5W}$, allowing a data quality check. Figure 2.3 shows temperature (b) and salinity (c) profiles recorded by the seal and the mooring measurements at the same time (max. ± 40 min). The most significant profile for this validation is the blue one, which is located just south of the mooring. Here, the temperature matches very well, keeping in mind that the seal profile is an average over 6 hrs. Additionally, mooring data from M_{31W} is shown in the plot (triangle markers), which captures warmer temperatures at mid-depth in agreement with the two seal profiles slightly up-slope at the 500 m-isobath. Salinity shows a bias of about 0.1, which however is consistent. Therefore, the seal data seems trustworthy and useful in order to analyse the general structure of hydrography.

2.1.4 Frequency analysis

Mooring data used in this thesis is low-pass filtered, as tidal currents can become very strong on the continental shelf. Even though they play an important role in mixing processes on the shelf and at the shelf break, they can overshadow seasonal or interannual variability. To ensure that no other signals are filtered out, I performed a spectral analysis using the multitapering method and plotted the one-sided power spectrum of the rotary components of one of the mooring time series (see Figure 2.4a). The major tidal frequencies are marked as well as the Coriolis frequency. All major peaks of the data coincide with a tidal frequency. Highest energies are found for the semi-diurnal tides and the Coriolis frequency, which are almost identical in my study area. The latitude where they are exactly the same is called *critical latitude* and is found at 74.5°S. Consequently, it is difficult to differentiate between tidal and inertial variability in a cartesian

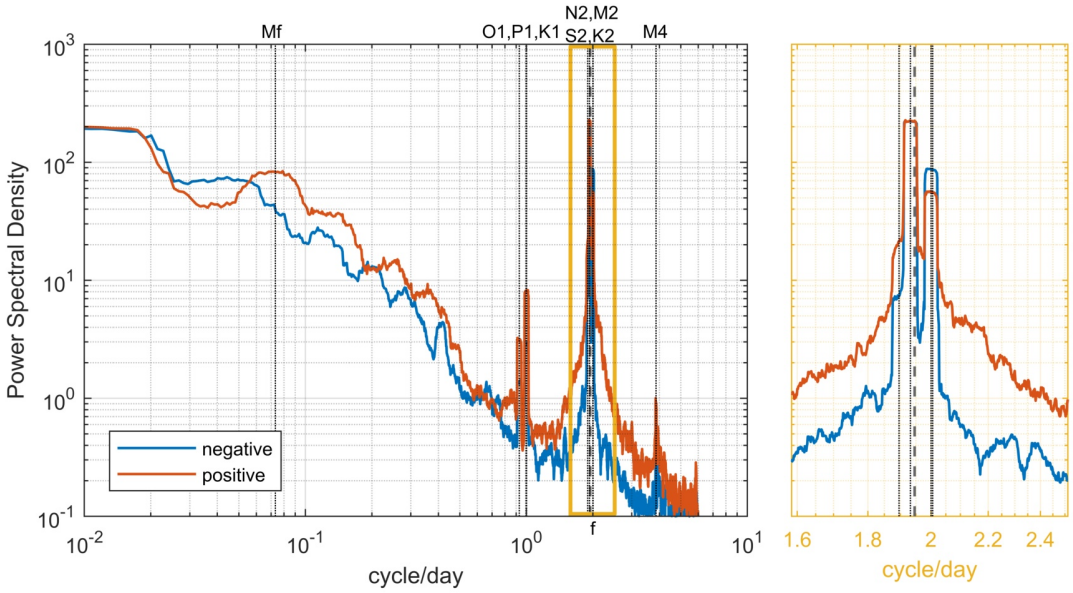

Figure 2.4: Multitaper rotary spectra of M_{31W}. The vertical dotted lines mark the major tidal frequencies and the thick dashed line marks the Coriolis frequency. The right panel is a zoom-in of the yellow rectangle in the left panel.

spectra, which is why a rotary spectra is advantageous. Here, positive and negative rotating frequencies are separated and since inertial oscillations are always into positive (negative) direction in the southern (northern) hemisphere, it is possible to detect them. Figure 2.4b shows a zoom-in of the yellow box and we find two separate peaks; one represents the M2 component and Coriolis frequency and the other the S2 and K2 component. The negative frequency density drops off faster on either side of the peaks compared to the positive frequency density, which can be attributed to the presence of inertial waves. In shallow areas, such as a continental shelf, the interaction of tides with topography will cause internal waves or since they are influenced by the Coriolis force also called inertial waves.

There are no other important signals in the time series and the major energy is found within the diurnal and semi-diurnal frequencies, while the fortnightly tides are not significant. Thus, it is legitimate to apply a low-pass filter with a cut-off frequency below 1 cycle per day, i.e., a period higher than 24 hrs, to the time series in order to remove the tidal signals.

2.1.5 Water mass modification through basal melting

When the HSSW, formed on the continental shelf in winter due to sea ice formation and related brine release, enters the ice shelf cavity, it interacts with the ice shelf base (Ice-Pump Mechanism). Due to the increased pressure, the freezing point decreases, hence the HSSW, having temperatures around the surface freezing point, is able to induce basal melting. This process is primarily depended on thermal driving, i.e. the temperature difference between the mixed layer close to the ice shelf base and the temperature of the ice base itself. The heat that the water loses is linear to the fresh water input from the ice shelf and can, therefore, be displayed as a straight line in the θS diagram, passing through the potential temperature and salinity of the source water (θ_0, S_0). The slope of the line was described by *Gade* (1979)

$$\frac{d\theta}{dS} = \underbrace{\frac{L}{S_0 c_w}}_{1} + \underbrace{\frac{(\theta_f - T_i)c_i}{S_0 c_w}}_{2} + \underbrace{\frac{(\theta_0 - \theta_f)}{S_0}}_{3}, \tag{2.2}$$

with θ_f being the potential temperature at which melting occurs at the ice shelf base and T_i the temperature of the core of the ice shelf; specific heat capacities of ice and water are given by c_i and c_w (approx. 2010 and $4000 \mathrm{J\,kg^{-1}\,°}C^{-1}$), respectively; L is the latent heat of ice ($3.35 \times 10^5 \,\mathrm{J\,kg^{-1}}$). The different terms arise from the following processes:

1. Latent heat of the source water mass. This term is the dominant one and leads to a slope of 2.4 °C.
2. Approximation of the heat loss into the ice shelf by diffusion. This term only becomes important in melting regions. It is roughly one order smaller than the first term but makes a measurable contribution by increasing the slope to roughly 2.8 °C
3. This term describes the need of the seawater to be cooled to the in-situ freezing point but does not make a significant contribution.

In my thesis, I will use the Gade line to discuss possible source water masses of the ISW that is observed in the hydrographic data. I will use the following conventions where source salinities between 34.65 and 34.7 describe HSSW produced on the Berkner Bank and salinities over 34.75 describe HSSW entering the cavity

via the Ronne Trough. Values in between are a transition product and below 34.65 describe a source within the Filchner Trough (see *Grosfeld et al.* (2001)).

2.1.6 Variance ellipses

For bivariate data, such as velocity data, the variability can be spread out into not one but two dimensions, hence the variances and covariance are given by a matrix:

$$\vec{\sum} \equiv \frac{1}{N}\sum_{n=0}^{N-1}(\vec{z}_n - \bar{\vec{z}})(\vec{z}_n - \bar{\vec{z}})^T, \qquad \text{with } \vec{z} = \begin{pmatrix} x \\ y \end{pmatrix} \quad \text{, and } \vec{z}^T = \begin{pmatrix} x & y \end{pmatrix}$$

$$\Leftrightarrow \qquad \vec{\sum} = \frac{1}{N}\sum_{n=0}\begin{bmatrix} (x_n - \bar{x})^2 & (x_n - \bar{x})(y_n - \bar{y}) \\ (x_n - \bar{x})(y_n - \bar{y}) & (y_n - \bar{y})^2 \end{bmatrix} \tag{2.3}$$

The red terms are the sample variances σ_x^2, σ_y^2 and the blue terms the covariance between x_n and y_n.
Using the *eigenvalue decomposition* on the variance matrix, shows that it can also be written in the following way:

$$\vec{\sum} = \underbrace{\begin{bmatrix} \cos\theta & -\sin\theta \\ \sin\theta & \cos\theta \end{bmatrix}}_{\vec{J}(\theta)} \underbrace{\begin{bmatrix} a^2 & 0 \\ 0 & b^2 \end{bmatrix}}_{\vec{D}(a,b)} \underbrace{\begin{bmatrix} \cos\theta & \sin\theta \\ -\sin\theta & \cos\theta \end{bmatrix}}_{\vec{J}^T(\theta)}, \tag{2.4}$$

where $\vec{J}(\theta)$ is the rotation matrix and its transpose ($\vec{J}^T(\theta)$) for the rotation angle θ and $\vec{D}(a,b)$ a diagonal matrix with the eigenvalues of $\vec{\Sigma}$. Note that the rotation matrix is unitary, hence the multiplication with its transpose gives the identity matrix I:

$$\vec{J}^T(\theta)\vec{J}(\theta) = \vec{J}(\theta)\vec{J}^T(\theta) = \underbrace{\begin{bmatrix} 1 & 0 \\ 0 & 1 \end{bmatrix}}_{I}$$

This holds because the transpose of the rotation matrix is the same as a rotation in the opposite direction. Hence:

$$\vec{\sum}^* = \vec{J}^T(\theta)\left[\vec{J}(\theta)\vec{D}(a,b)\vec{J}^T(\theta)\right]\vec{J}(\theta) = \vec{D}(a,b)$$

where $\vec{\Sigma}^*$ is a rotated version of the covariance matrix. This means that rotating the data diagonalizes $\vec{\Sigma}$, i.e. the covariance becomes zero. This is the common

approach used in principal component analysis, such as the Empirical Orthogonal Function (EOF) analysis. Furthermore, it can be shown that the covariance matrix describes an ellipse with major axis a, minor axis b and the orientation angle θ (with respect to the x-axis). Its eccentricity gives us information about whether the variability is anisotropic or directional. The orientation of the ellipse indicates the direction in which the variability is concentrated.
The general form of an ellipse is given by:

$$\frac{x^2}{a^2} + \frac{y^2}{b^2} = \begin{bmatrix} x & y \end{bmatrix} \begin{bmatrix} 1/a^2 & 0 \\ 0 & 1/b^2 \end{bmatrix} \begin{bmatrix} x \\ y \end{bmatrix} = \vec{z}^T \vec{D}^{-1}(a,b)\vec{z} = 1 \tag{2.5}$$

Applying the same form to the covariance matrix leads to:

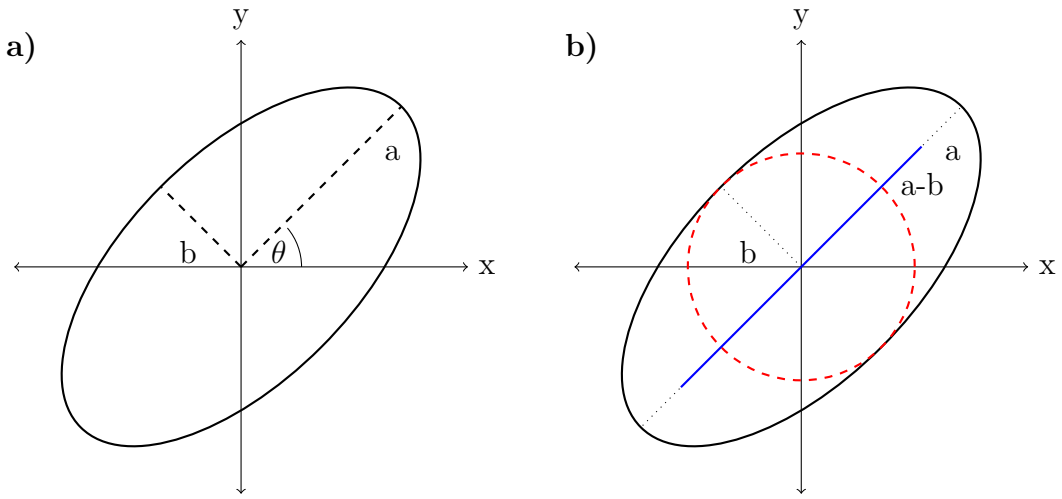

Figure 2.5: a) Schematic of a variance ellipse with major axis a, minor axis b and the orientation angle θ. b) Variance ellipses with blue line indicating directional variability and red circle giving the purely isotropic variability.

$$\begin{aligned}
\vec{z}^T\vec{\Sigma}^{-1}\vec{z} &= \vec{z}^T \left[\vec{J}(\theta)\vec{D}(a,b)\vec{J}^T(\theta)\right]^{-1} \vec{z} \\
&= \vec{z}^T \vec{D}^{-1}(a,b) \underbrace{\vec{J}^{-1}(\theta)\left(\vec{J}^T(\theta)\right)^{-1}}_{=\left(\vec{J}(\theta)\vec{J}^T(\theta)\right)^{-1}=I^{-1}=I} \qquad \Big| \cdot\vec{J}(\theta)\cdot\vec{J}^T(\theta) \\
&= \left[\vec{J}^T(\theta)\vec{z}\right]^T \vec{D}^{-1}(a,b)\left[\vec{J}^T(\theta)\vec{z}\right] \qquad \text{with } \vec{J}(\theta) = \left(\vec{J}^T(\theta)\right)^T \\
&= 1
\end{aligned} \tag{2.6}$$

To plot the ellipse we need a and b; these can be given explicitly:

$$\begin{aligned} a^2 &= \frac{1}{2}\mathbf{tr}\{\Sigma\} + \frac{1}{2}\sqrt{[\mathbf{tr}\{\Sigma\}]^2 - 4\mathbf{det}\{\Sigma\}} \\ b^2 &= \frac{1}{2}\mathbf{tr}\{\Sigma\} - \frac{1}{2}\sqrt{[\mathbf{tr}\{\Sigma\}]^2 - 4\mathbf{det}\{\Sigma\}} \end{aligned} \tag{2.7}$$

with $\mathbf{tr}\{\Sigma\}$ being the trace, i.e. the sum of the diagonal elements and $\mathbf{det}\{\Sigma\}$ being the determinant of Σ. The angle θ can be obtained by carrying out the matrix multiplication $\vec{J}(\theta)\vec{D}(a,b)\vec{J}^T(\theta)$ and some rewriting:

$$\tan 2\theta = \frac{2\Sigma_{xy}}{\Sigma_{xx} - \Sigma_{yy}} \tag{2.8}$$

With these three quantities the variance ellipse can be plotted and it can further be decomposed into directional variability in direction of θ with the variance $a^2 - b^2$ and into purely isotropic variability with variance $2b^2$ (For details on how to obtain a,b and θ see *Emery and Thomson* (2001), Chapter 4 and *Preisendorfer* (1988), Chapter 2). The ellipses provide generally a powerful tool when being combined with low- or bandpass filtering, as done in this thesis. They allow to separate tidal variability, which is often in the direction of bathymetry and dominates the velocity time series, from the internal, such as seasonal variability.
In this thesis, variance ellipses are used to analyse monthly mean velocities from our two-year long mooring time series from the eastern flank of the Filchner Trough, in order to investigate the seasonal cycle of the circulation and hydrography.

2.2 The Finite Element Sea Ice-Ocean model

In this study, the global Finite Element Sea Ice-Ocean Model (FESOM) is used (*Timmermann et al.*, 2009; *Wang et al.*, 2014). Its precursor is the Finite Element Ocean Model (*Danilov et al.*, 2004; *Wang et al.*, 2008), which has been coupled to a sea ice model, including ice shelf cavities and a dynamic-thermodynamic sea-ice component (*Timmermann et al.*, 2009). It has been developed at the Alfred Wegener Institute and is the first global general circulation model based on an unstructured mesh (see Figure 2.6). Unstructured meshes have the advantage that they can be refined locally, depending on the area of interest. This is a valuable tool especially for polar regions, where the Rossby radius of deformation becomes

very small (see Figure 2.7c) and at the same time limited observations make it difficult to apply accurate boundary conditions for regional models.

2.2.1 Governing Equations

The ocean model solves the set of hydrostatic primitive equations with the Boussinesq approximation applied. The system of governing equations is split into two-subproblems, dynamical and thermodynamical, and solved separately. In the dynamical part the 3-D momentum equations (2.9), the vertically-integrated continuity equation (2.10) and the hydrostatic equation (2.11) are solved for horizontal velocity ($\vec{u}_h$), sea surface height (η) and pressure p:

$$\frac{\partial \vec{u}}{\partial t} + \vec{u} \cdot \nabla \vec{u} + f(\vec{k} \times \vec{u}) + g\nabla\eta + \frac{1}{\rho_0}\nabla p = \nabla \cdot A_h \nabla \vec{u} + A_v \frac{\partial^2 \vec{u}}{\partial^2 z}, \tag{2.9}$$

$$\frac{\partial \eta}{\partial t} + \nabla \cdot \int_{z=-H}^{z=\eta} \vec{u}\, dz = 0, \tag{2.10}$$

$$\frac{\partial p}{\partial z} = -g\rho. \tag{2.11}$$

where $\vec{u} = (u, v, w)$ is the velocity vector, f is the latitude dependent Coriolis parameter $f = f(\theta)$, $\vec{k} = (0, 0, 1)$ is the vertical unit vector and g the gravitational acceleration. The mean sea water density and the deviations from it are ρ_0 and ρ, respectively. A_h and A_v represent the lateral and vertical turbulent viscosity coefficients.

The thermodynamic part solves the tracer equations for potential temperature T and salinity S (2.13), the continuity equation (2.12) for the vertical velocity w and uses the equation of state (2.14) to compute density (*Jackett and Mcdougall*, 1995):

$$\frac{\partial w}{\partial z} = -\nabla_h \cdot \vec{u}_h, \tag{2.12}$$

$$\frac{\partial C^m}{\partial t} + \vec{u_h} \cdot \nabla C^m + \frac{\partial (wC^m)}{\partial z} = \nabla_h \cdot K_h^m \nabla C^m + \frac{\partial}{\partial z}\left(K_v^m \frac{\partial C^m}{\partial z}\right), \tag{2.13}$$

$$\rho = \rho(T, S, p). \tag{2.14}$$

with $C^1 \equiv T$, $C^2 \equiv S$ and K_h^m, K_v^m are the lateral and vertical turbulent viscosity coefficients for the m^{th} tracer.

Ice shelves provide a link between the open ocean and the land ice mass. The

interaction of the two plays a significant role in the polar oceans. The ocean-ice shelf interaction in the model is based on the three-equation approach by *Hellmer and Olbers* (1989). While the ice shelf cavity geometry remains constant, the model accounts for the thermodynamic coupling, i.e., for the heat loss from the ocean to the ice and a glacial melt water flux is derived and applied to the salinity in the layer adjacent to the ocean- ice shelf interface.

The sea ice component of FESOM is a dynamic-thermodynamic sea ice model (*Timmermann et al.*, 2009), based on the thermodynamics of *Parkinson and Washington* (1979). It is a two-layer model, with the upper layer accounting for snow and the lower layer representing ice. Heat storage is neglected in both layers. Velocities for the advection of ice and snow volume are derived from a elastic-viscous-plastic solver described by *Danilov and Wang* (2015).

2.2.2 Horizontal mesh

The governing equations are all solved on the same locations (nodes), which is analogous to the Arakawa A-grid (*Arakawa and Lamb*, 1977). The horizontal mesh consists of triangular elements at the surface while the 3D domain is represented by tetrahedral elements. In the vertical, nodes are aligned below the surface nodes. Moreover, a hybrid grid is used. Here, 25 terrain-following (sigma) layers are used down to a defined isobath (2500 m) around the Antarctic continent, while 36 z-layers are used in the ocean north of the isobath (Figure 2.6). It was shown by *Wang and Meredith* (2008) that terrain-following grids allow for a better representation of overflow processes, e.g. downslope plume propagation. However, such a set-up can also induce artificial advection and diffusion along sigma-layers (e.g. *Lemarié et al.* (2012)). On the southern Weddell Sea continental shelf, overflow processes of the locally formed dense water play an important role, which is why a hybrid configuration was chosen.

The advantage of finite-element grid is that they allow local refinement of the horizontal resolution, which is particularly useful in studies of high latitudes, a region where the internal Rossby radius of deformation becomes very small ($\mathcal{O}$[3 km]). In this thesis, two different meshes are used; the first one (hereafter referred to as LOW) is taken from *van Caspel* (2016) and has a resolution between 4 km and 73 km in the Weddell Sea, with the higher resolution on the southern and western Weddell Sea, while the northeastern corner of the gyre is resolved coarsely ($\mathcal{O}$[3 km], see Figure 2.7a). The isobath for the transition from z- to sigma-levels

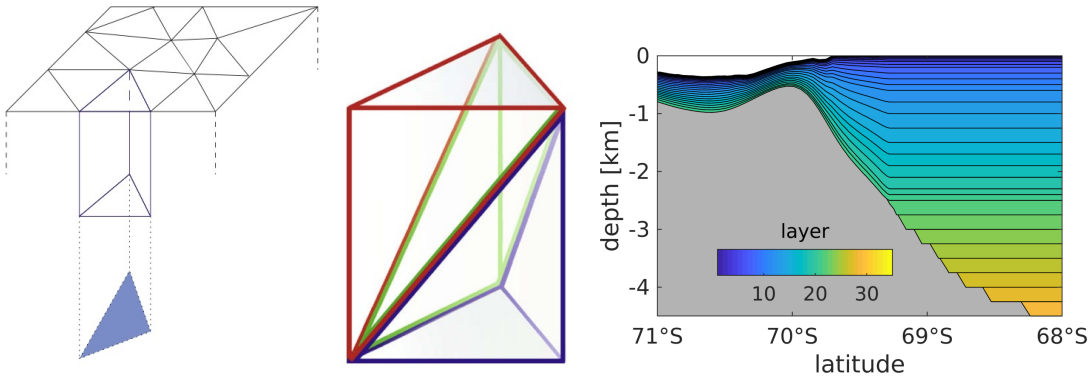

Figure 2.6: *Left*: Figure from *Timmermann et al.* (2009) (Their Figure 1);Illustration of the three-dimensional structure of the FESOM mesh. Grid nodes in the interior ocean are aligned under the surface triangles (left). Each of the resulting prisms is split into three tetrahedrons (right). *Right*: Schematic of a hybgrid vertical grid. The sigma-layers are used in adjunction with ice shelf modelling for Antarctic regions and along the continental shelf; z-level are used in the open ocean beyond the 2500 m isobath.

is set to 2500 m. Additionally, I designed a new mesh (hereafter HIGH) for this study, with increased resolution over the whole Weddell gyre, including the eastern boundary of the gyre (resolution ≈ 15 km). Further refinement was made over the continental shelf in the southern Weddell Sea, with a mean resolution of 3.5 km. Although it was pointed out that a model resolution $\mathcal{O}(1\,\text{km})$ would be needed in order to fully resolve mesoscale processes (*St-Laurent et al.*, 2013), the mesh size could not be further increased due to computational constraints. Mesh HIGH comprises over 11 Mio. nodes.

Figure 2.7c shows a map of the first baroclinic Rossby radius of deformation over the Weddell Sea area, which can be estimated, according to *Chelton et al.* (1998), by vertically integrating the buoyancy (Brunt-Väisälä) frequency N over the whole water column, using the density field from the World Ocean Atlas 2013 (WOA3,*Locarnini et al.* (2013); *Zweng et al.* (2013)):

$$R = \frac{1}{f\pi} \int_{-H}^{0} N(z) dz, \tag{2.15}$$

with N being

$$N = \sqrt{\frac{-g}{\rho} \frac{\partial \rho}{\partial z}} \tag{2.16}$$

Due to a weakly stratified water column, the whole Weddell Gyre is governed by

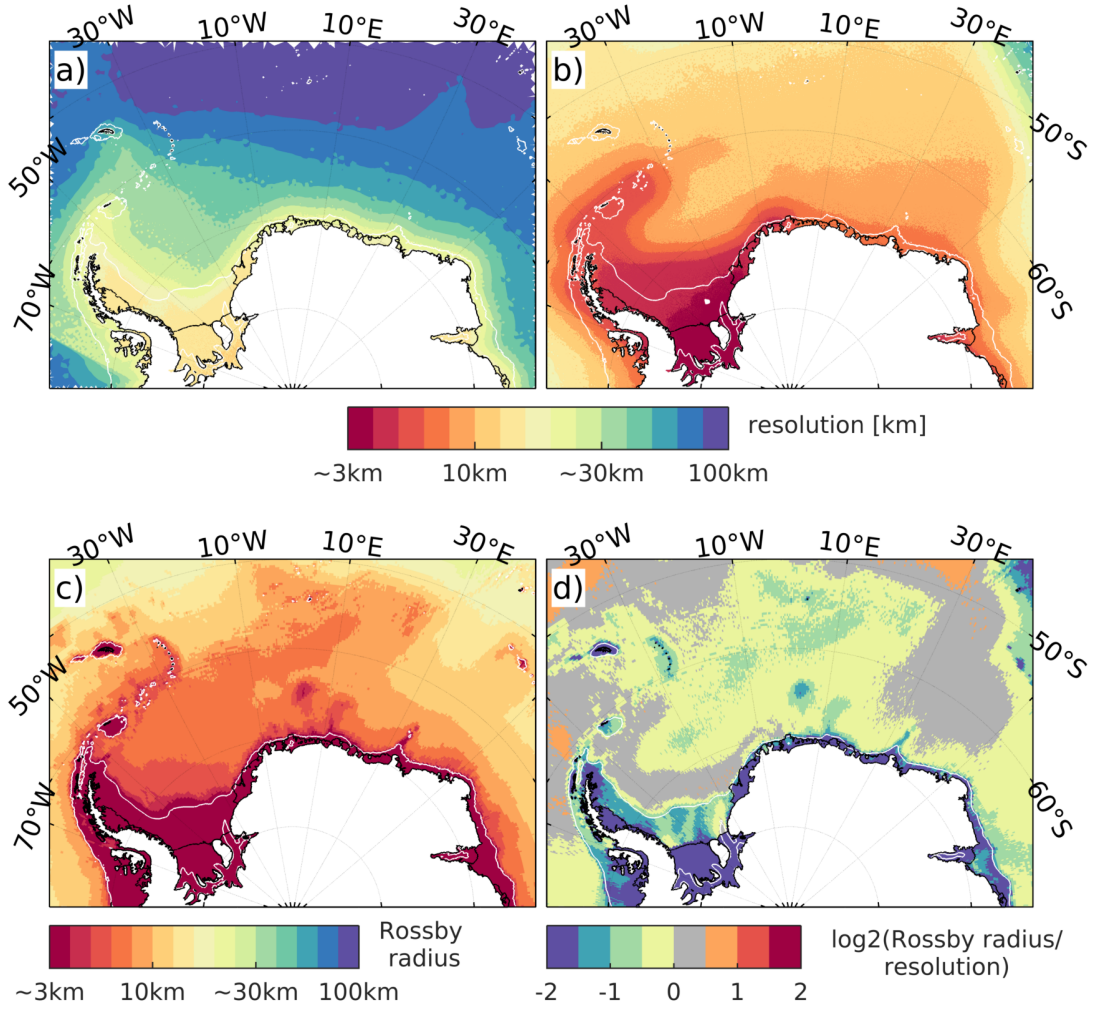

Figure 2.7: Model resolution for mesh LOW (a) and mesh HIGH (b) on a logarithmic color scale. c) estimate of the first baroclinic Rossby radius, derived from WOA13 according to *Chelton et al.* (1998); d) Logarithm of the ratio of the first baroclinic Rossby radius relative to the mesh resolution for mesh HIGH. For values above one, the model is eddy-resolving while it is eddy-permitting for values between 0 and 1.

Rossby radii below 10 km and even smaller on the continental shelf ($2-4$ km) and in the ice shelf cavities (1 km). This poses a strong limitation for global ocean modelling. Even the HIGH mesh, as generated for this study, is only at the edge of eddy-permitting within the Weddell Gyre. This is illustrated in Figure 2.7d showing the ratio of the Rossby radius the mesh resolution , where the model is eddy-resolving for values above 1, and eddy-permitting for values between 0 and 1. Values below 0 indicate areas where eddies are suppressed. The influence of

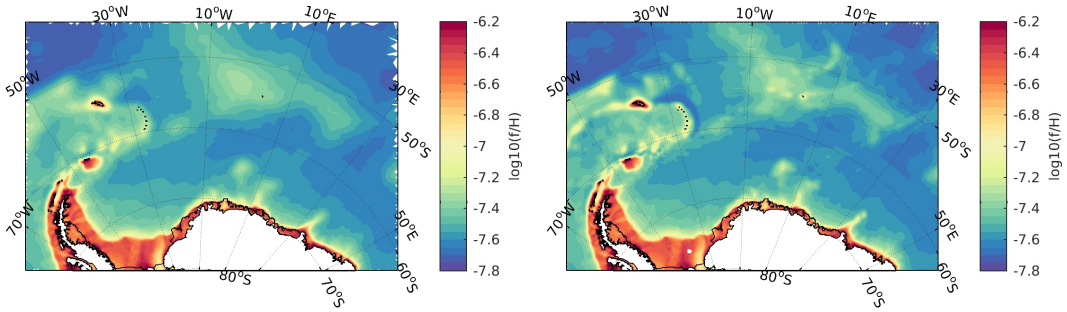

Figure 2.8: f/H contours for mesh LOW (left) and HIGH (right).

stratification becomes particularly clear in the eastern inflow region of the gyre, i.e. around 30°E, where WDW is diverted southward and enters the gyre ($\approx$ 70°S). Even though the resolution is the same, a shift from non-eddy-permitting to eddy-permitting conditions is observed. Although not eddy-resolving, mesh HIGH provides a big step toward eddy-resolving simulations in the Weddell Sea.

The model bathymetry is derived from RTopo-1 (*Timmermann et al.*, 2010) for mesh LOW and from RTopo-2 (*Schaffer et al.*, 2016) for mesh HIGH. The latter primarily focused on improvement around the Greenland ice sheet and only small corrections were applied for the cavity geometry of the Getz, Abbot and Fimbul ice shelf in Antarctica. However, large differences in bathymetry between the two meshes are related to model resolution and the smoothing required by the use of a terrain-following vertical coordinate. Differences are particularly pronounced in the northeastern corner of the gyre, where the Southwest Indian Ridge is located. This is visible in f/H contours, shown for both meshes in Figure 2.8, where f is the Coriolis parameter and H is the depth off the ocean. Generally, ocean currents are strongly steered by topography by following f/H contours in areas of low stratification, due to the conservation of vorticity.

2.2.3 Atmospheric forcing and model set-up

The model is forced with the National Centers for Environmental Prediction Climate Forecast System Reanalysis (NCEP/CFSR, *Saha et al.* (2010)), which is available from 1979 to the beginning of 2011 (only full years are used, i.e. 1979 -2010). The data is provided with a 38 km lateral and a 6 hr temporal resolution. Atmospheric forcing fields used are: zonal wind (u,v), air temperature and specific humidity at 10 m height, as well as precipitation, evaporation, long- and

shortwave radiation.

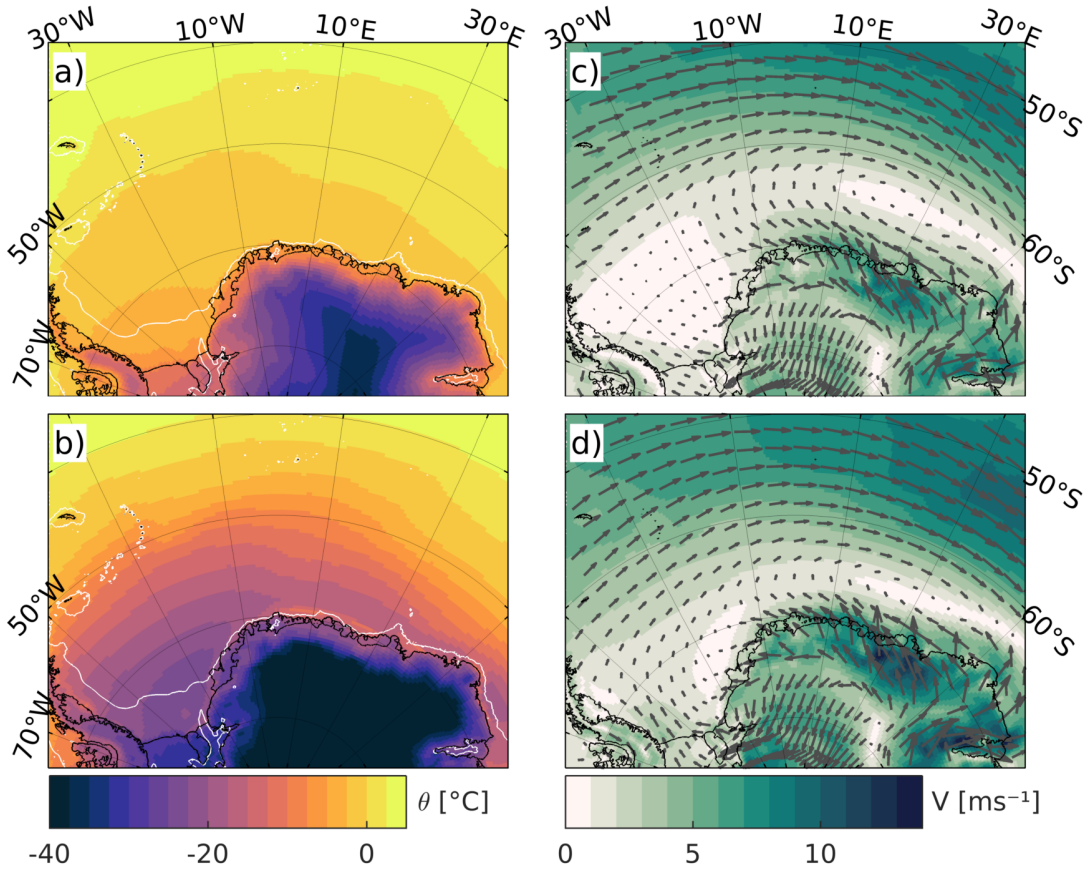

Figure 2.9: Mean summer (Dec-Feb) and winter (Jun-Aug) air temperature (a,b) and wind field (c,d) at 10 m height in the Weddell Sea region from NCEP/CFSR

Climatological mean air temperature and wind field over the Weddell-Enderby basin from the NCEP/CFSR reanalysis are shown for summer (DJF) and winter (JJA) in Figure 2.9. On average, the Weddell Sea is governed by surface temperatures below 0°C all year around, with the southern continental shelf being the coldest area. Here, summer temperatures average −5 °C, while the temperature drops below −20 °C in winter. Over the continent, temperatures colder than −30 °C prevail permanently; only along the margins, temperatures are warmer in summer. The mean wind field is cyclonic, with the centre being located at roughly 65°S. In winter the strong westerlies shift slightly southward and the whole cyclone strengthens, which is for example notable in the western Weddell Sea. Coastal easterlies are particularly strong east of the prime meridian and in the southwestern corner of the Weddell Sea. In the Filchner Trough region katabatic, i.e., offshore winds dominate, and transport cold continental air over the

ocean.

The simulations are initialised with mean ocean temperature and salinity fields from the WOA 2013 (*Locarnini et al.*, 2013; *Zweng et al.*, 2013). For areas with sea surface temperature less than $-1°C$ sea ice concentration is initially set to 0.9 with a sea ice thickness of 1 m.

Hindcast simulations for the time period of 1979-2010 are carried out for both meshes, with monthly mean fields as output. The first 20 years are considered as spin-up time and the last 10 years are used for analysis.

3. The Filchner Trough hydrography inferred from observations

The Filchner Trough is an important bathymetric feature on the southern Weddell Sea continental shelf as the major exchange between the FRIS and the open ocean occurs via the trough. Not only does it provide a pathway for the dense ISW export, ultimately contributing to the WSBW formation but it also serves as a conduit for WDW toward FRIS. Despite its importance, the region is still heavily undersampled and the available oceanographic data has a strong summer bias due to the remoteness and heavy sea ice cover all year around. Therefore, any data set is valuable and should be presented.

3.1 General hydrography of the Filchner Trough

Ship-borne hydrographic data from two Polarstern cruises give a good overview of the general hydrography in the Filchner Trough and the adjacent Eastern Shelf (see map Figure 1.5) in summer time. Figure 3.1 shows the bottom temperature (left) and salinity (right) of all CTD stations obtained during the two cruises. Three different water mass regimes can be found. The whole continental shelf is governed by bottom temperatures close to the surface freezing point, while warmer water is found at the bottom of the continental slope with temperatures higher than -1°C. This is the WDW, which is of circumpolar origin and is transported along the continental slope. WDW, being a derivative of CDW, is associated with high salinities ($S > 34.6$). However, also the much colder water in the Filchner Trough has salinities over 34.6. Hence, one needs both parameters to identify the relevant water masses and they are best identified in θS-space (Figure 3.1c).

On the Eastern Shelf much lower salinities around 34.4 represent ESW, which is sometimes hard to distinguish from WW. Both are typical fresher water masses

found on the continental shelf in the Weddell Sea. The properties in the trough (temperture below surface freezing point plus saline) are characteristic of ISW, the water mass emerging from beneath the FRIS having temperatures below the surface freezing point (dashed line in Figure 3.1c). West of the Filchner Trough, on the Berkner Bank, the highest bottom salinities are found, associated with temperatures around the surface freezing point. This water mass is called HSSW, which is produced due to brine rejection during sea ice formation in winter and is the densest water mass found in the Weddell Sea.

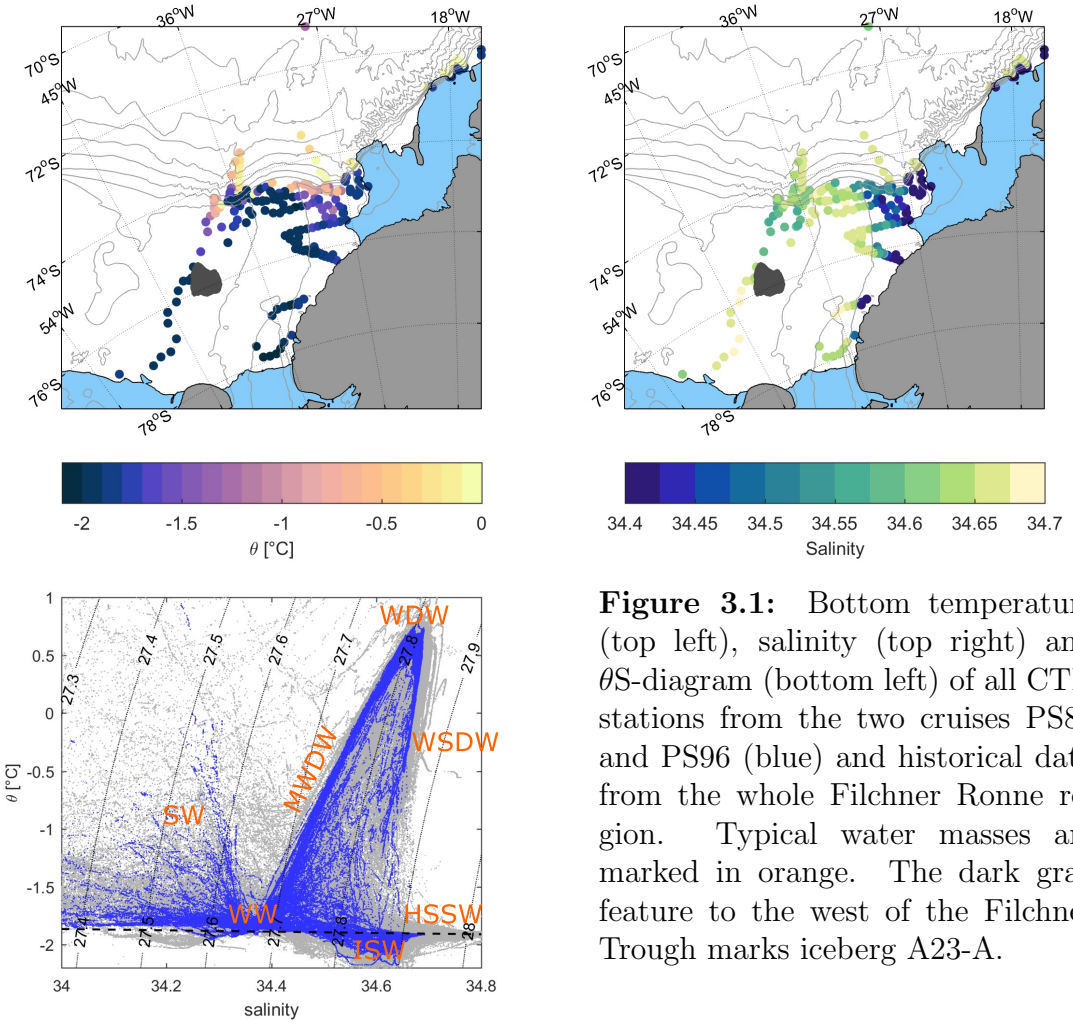

Figure 3.1: Bottom temperature (top left), salinity (top right) and θS-diagram (bottom left) of all CTD stations from the two cruises PS82 and PS96 (blue) and historical data from the whole Filchner Ronne region. Typical water masses are marked in orange. The dark gray feature to the west of the Filchner Trough marks iceberg A23-A.

Figures 3.2 shows hydrographic temperature sections crossing the eastern flank of the trough at different latitudes, starting at the sill down to 78°S. During both cruises the sea ice cover over the western flank was too thick to break through with the ship. The sections show that ISW, marked by the -1.9°C isotherm

(dashed line), fills almost the whole trough. The ISW layer thickness is steadily increasing toward the south due to the deepening of the trough but also the upper boundary of the layer shoals from 300 m depth at the sill to 100 m depth at 78°S, where the ISW layer reaches a thickness of over 1000 m. In agreement with *Darelius et al.* (2014c) I find the coldest ISW in form of isolated lenses located over the eastern slope of the trough at roughly 400 m depth (i.e. stations 14, 78, 70, 57, 96), where it is thought to be transported toward the sill (*Darelius et al.*, 2014a). Unfortunately, no direct velocity measurements were taken, however, the density structure suggests a northward baroclinic flow of the ISW cores in our data. ISW properties will be discussed in more detail at a later point (3.4). Generally, the lowest ISW temperatures are found at mid-depth while slightly higher temperatures -still below surface freezing point- at the bottom are associated with salinities over 34.65, indicating the influence of HSSW.

Being the densest water mass on the continental shelf HSSW will generally be found in the bottom layers. While observations on the western flank of the trough are rare, the common believe is that HSSW water formed on the Berkner Bank during winter will flow down the slope on the western side and fill the bottom of the trough. Selected CTD-stations within the trough and on the Berkner Bank are shown in Figure 3.3. All salinity profiles (Figure 3.3b) in the trough show a well mixed bottom layer. Highest salinities of 34.68 are found -as expected- at two stations south of the iceberg A23-A on Berkner Bank (#31,#35), however, station 61 in the centre of the trough shows the same value.

Looking at the θS-diagram one sees that the associated bottom temperatures at all three stations are very close to the surface freezing point associated with a deviation from the Gade line toward higher salinity, indicating a direct influence of HSSW. Its presence in the deep trough strongly supports the hypothesis that dense waters formed on Berkner Bank indeed make their way into the Filchner Trough. Several stations near the sill show bottom salinities over 34.65 as well with temperatures close to the surface freezing point suggesting the influence of HSSW. Stations 26, 46, 48 and 49 are located on the slope west of the sill and gradually deepen, while the observed salinity gradually freshens. This could hint to a downslope flow of HSSW which slowly entrains and mixes with the surrounding ISW. Furthermore, the temperature section at 75°S (Figure 3.2c) reveals two separate dense cores, one in the centre and one on the western side of the sill. The latter could represent a 'direct' route toward the sill. At 74.5°S, station 49 and 52 might

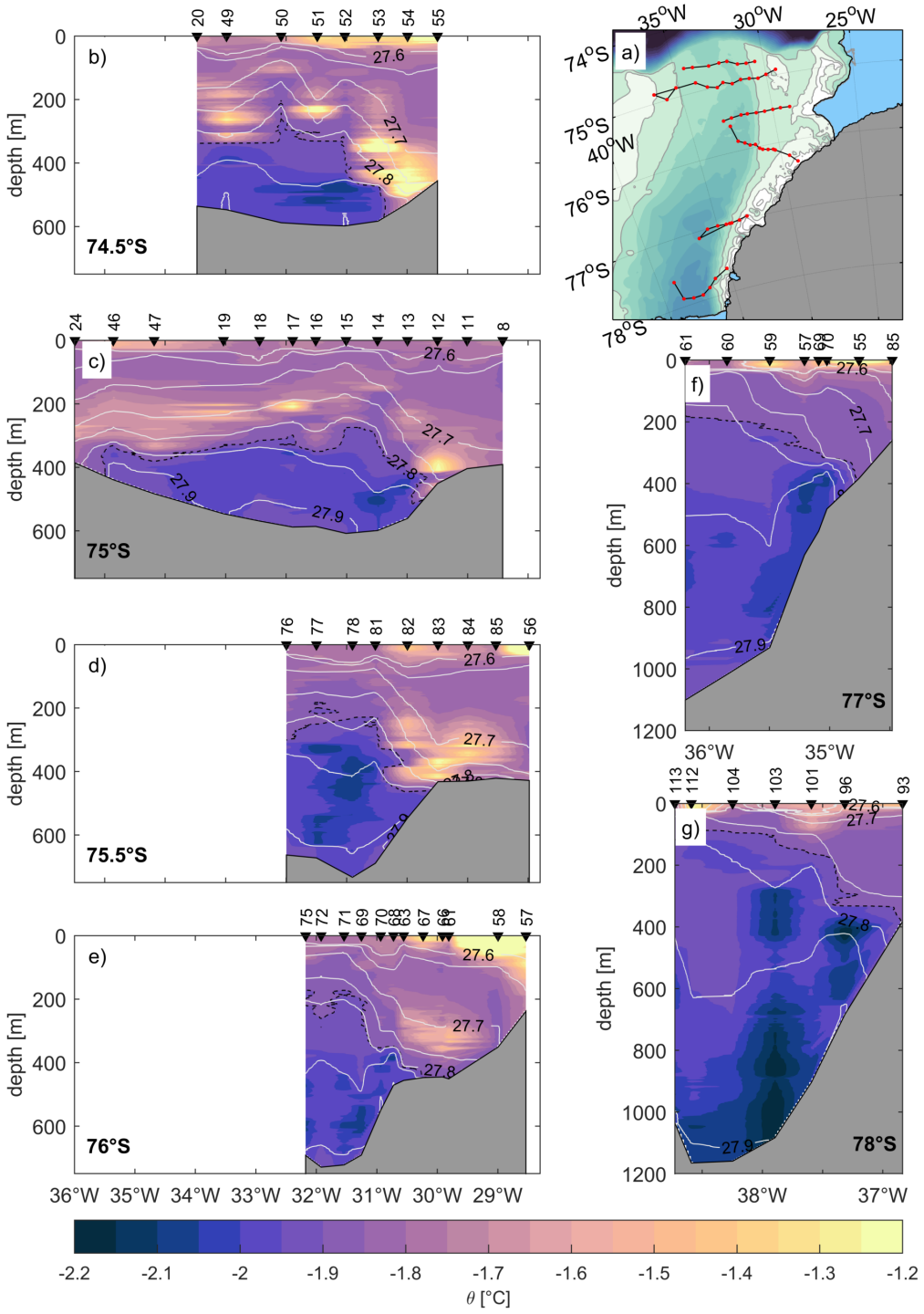

Figure 3.2: Potential temperature along 4 consecutive sections from the Filchner Sill towards the south obtained during PS82 and PS96. The black dashed contour line represents the −1.9°C isotherm, to indicate the upper bound of the ISW layer. The bathymetry is given by the profile depths.

show the remnants of the two cores directly at the sill.

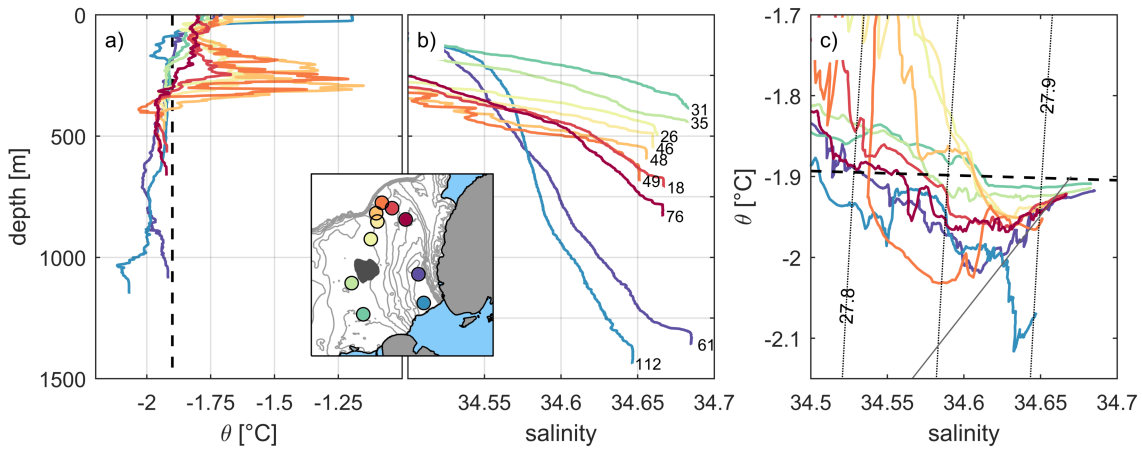

Figure 3.3: Selected potential temperature a) and salinity b) profiles obtained during PS82 and PS96 and the associated θS diagram c). The thick dashed line in a) and c) indicates the surface freezing point temperature and the thin grey line in c) is the Gade line with a source salinity of 34.67. The thin dotted lines in c) give potential density referenced to surface pressure.

In times of global warming and sea level rise the focus has increasingly shifted to studying the heat transport toward ice shelves and glaciers. Our hydrographic sections show how MWDW enters the Filchner Trough along its eastern flank, where it is found up to 76°S. Its potential density ranges from 27.7 to 27.8 kg m^{-3} and is, therefore, lighter than the outflowing ISW, which has generally a density higher than 27.8 kg m^{-3}. At the sill (74.5°S), both water masses are found side by side, i.e at the same depth level, creating a strong horizontal density gradient, inducing a southward baroclinic flow. The sill poses a potential vorticity barrier for the northward flowing ISW, and causes a deflection toward the west, hence allowing a lighter water mass, i.e. the MWDW, to enter the trough in the east. At the sill, we find the highest temperatures around -1°C with densities being at the upper limit of the general range. The off-shelf WDW core is at a depth of roughly 1200 m and has a density above 27.8 kg m^{-3} (see Figure 3.4), which explains that the highest temperatures are associated with high densities. It also shows that the warmest and densest WDW did not enter the Filchner Trough at the time of data acquisition and that work has to be done in order to lift the WDW onto the continental shelf. Only a mixing product of the WDW and the overlaying WW enters the shelf, the MWDW.

Furthermore, warm lenses are observed in the centre of the sill region above

the ISW layer, which has an upper limit of 300 m there. At 75.5°S they are not present any more, which could be associated with a shallower reaching ISW layer ($\approx$ 200 m). It has been suggested before at the mouth of the Filchner Trough intense mesoscale eddy activity plays an important part in the cross-shelf heat exchange (e.g. *Daae et al.* (2017)). The observed lenses could be the manifestation of this, supported by the density structure at i.e. station 51, where a dip in the 27.7 kg m^{-3} isopycnal indicates an anti-cyclonic eddy.

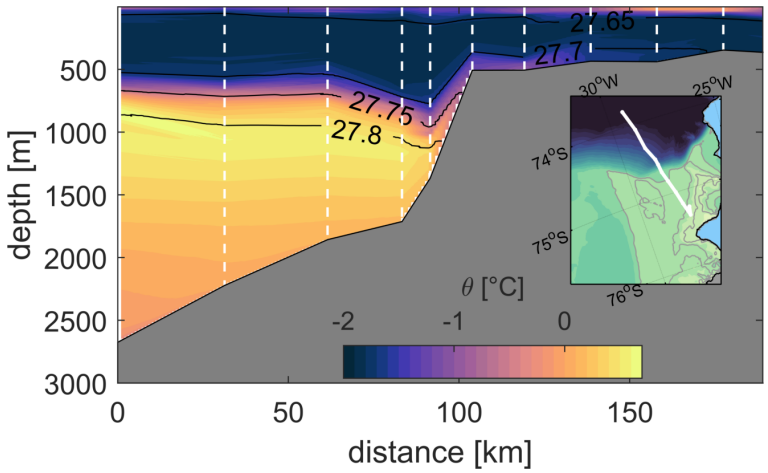

Figure 3.4: Potential temperature section across the shelf break east of the Filchner Trough obtained during PS82. Thin black lines give potential density referenced to the surface. Map inlet shows bathymetry and the section is marked in white.

Focusing on the warm water along the eastern flank, I find that at 76°S only a lighter, cooler product of MWDW is present at mid-depth, overlaying cooler shelf waters. Generally, the bottom waters on the shelf east of the trough become denser from 75°S toward 76°S, where the ISW layer extends onto the shallower shelf. This could essentially block the MWDW found further north at the bottom. Another feature in this section is the downward sloping isopycnals toward the coast, indicating the presence of a warm and fresh coastal current. This part on the continental shelf is one of the few places which is regularly governed by coastal polynyas, allowing a strong heating of the surface waters. *Darelius et al.* (2016) argue that an exceptionally strong boundary current in 2013 was responsible for the southward transport of MWDW on the Eastern Shelf toward the ice front in late summer.

Little is know about the seasonality on the Eastern Shelf, which was the motivation for deploying three moorings across the eastern flank in 2014. In the

following, I will analyse these data with the focus on the seasonal evolution of hydrography.

3.2 Seasonal hydrography on the eastern shelf of the Filchner Trough

Due to the hazardous conditions in the southern Weddell Sea during winter, CTD measurements have a strong summer bias and little is known about the seasonal change on hydrography on the continental shelf. Moored instruments enable us to record data all year around. Our two-year long time series (see data section) revealed a distinct seasonal cycle on the eastern shelf.
[1]

3.2.1 Hydrographic setting

The mooring locations and vertical configurations are shown in Figure 3.5a together with a hydrographic section obtained in January 2016 during the recovery cruise (PS96), providing a spatial reference of the water mass distribution around the moorings at 76°S. The white contour line indicates surface freezing point temperatures, i.e. the water mass boundary of ISW. It shows a thickening of the ISW layer toward the center of the trough, with the coldest water ($\theta < -2$°C) seen just off the bottom near the base of the slope.The density distribution (black isolines) shows dense ISW accessing the shallow shelf east of the trough, where it covers the bottom as a thin layer. Above, MWDW ($\theta > -1.6$°C) is found at intermediate depth ($300 - 400$ m) in the density range of $27.70 - 27.75\,\mathrm{kg\,m^{-3}}$. The layer between the warm summer surface layer and the MWDW consists of Winter Water (WW), which is the remnant water mass of the previous winter mixed layer. In general, the shelf is covered with Eastern Shelf Water (ESW), having a lower salinity than WW due to the downwelling of Antarctic Surface Water (ASW) (*Zhou et al.*, 2014). However, sometimes it is difficult to distinguish between the two.

Mooring $M_{31.5W}$ is located on the eastern slope of the Filchner Trough at 580 m depth, while M_{31W} and $M_{30.5W}$ are deployed on the wider continental shelf east of

[1] This section is part of a publication in the *Journal of Geophysical Research* with the title *Seasonal cycle of hydrography on the eastern shelf of the Filchner Trough, Weddell Sea, Antarctica (Ryan et al., 2017).*

the trough, both at a similar depth around 450 m (see Table 2.1). At $M_{31.5W}$, the lower instrument is surrounded by ISW and the upper instrument is situated in the vicinity of the interface between the ISW and the warmer layer above at the time of deployment. M_{31W} is surrounded by ISW at the bottom but the upper instrument lays within the observed MWDW density range. The latter also is the case for $M_{30.5W}$, however, the bottom is covered by water with temperatures just above the surface freezing point, hence the ISW is not reaching that far onto the eastern continental shelf. The isopycnals on the wide shelf are only slightly inclined, indicating a weak baroclinic flow across the section, compared to the slope.

Figure 3.5b shows the velocity data from all moorings as a progressive vector diagram , with temperature given by the color shading. $M_{31.5W}$ shows a continuous northward flow (only data from January to August 2014) of ISW, confirming the northward flowing ISW plume at the eastern flank of the trough, first suggested by *Darelius et al.* (2014a) and also suggested by our hydrographic sections. The moorings on the shallow Eastern Shelf show a distinct shift in current direction and temperature throughout the year. Warm temperatures are always associated with southwestward flow, which is very persistent for about three months. In winter the current turns westward and then northward while the bottom temperatures are around the surface freezing point or below, indicating the seasonal presence of ISW on the Eastern Shelf.
In the following we will start by focusing on the data of M_{31W}, as it shows the most pronounced seasonality. Our findings will be compared to the time series at $M_{31.5W}$ and $M_{30.5W}$ in section 3.2.4.

3.2.2 Four-phased seasonal cycle

Based on the potential temperature time series from the upper and lower sensors at M_{31W} (Figure 3.6d), we distinguish four characteristic phases that are apparent throughout each of the years of the time series. The phases are marked with different background shadings in Figure 3.6. They will be briefly introduced before being analyzed in more detail.

The first phase lasts roughly from January to mid-March and is seen in all three summer seasons covered by our mooring time series (2014-2016), however in 2016 only the beginning is captured. This phase is characterized by a gradual temperature increase - caused by southward advection of MWDW- at the upper

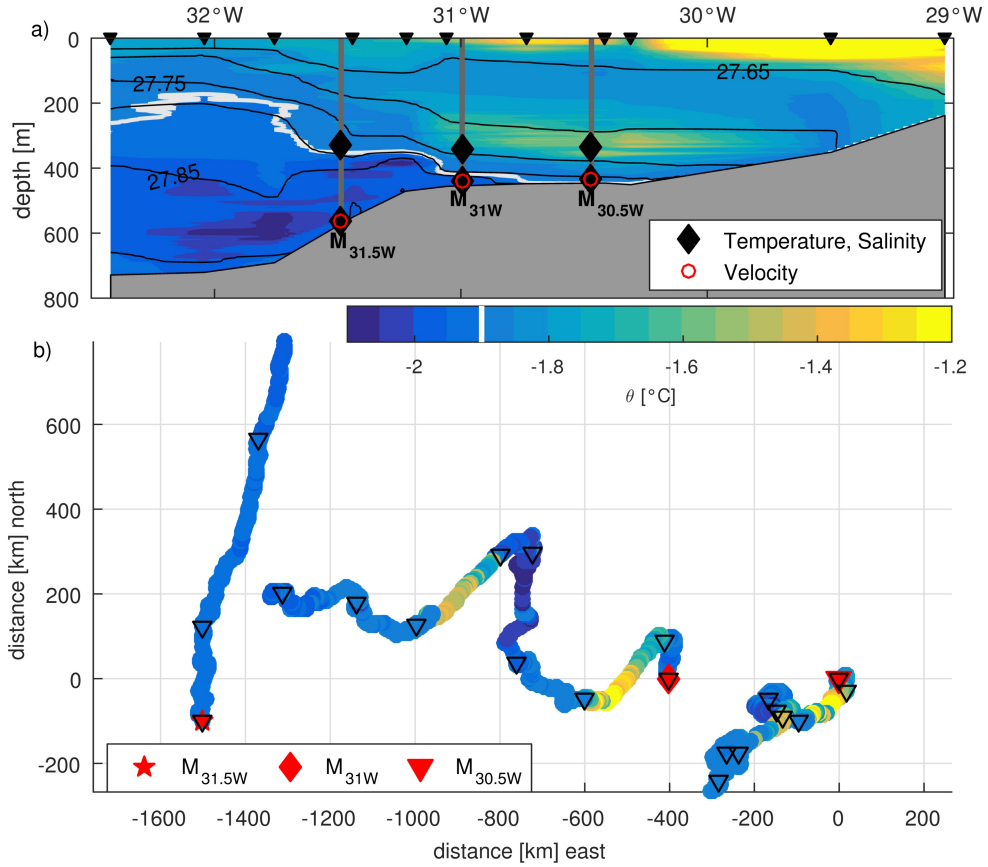

Figure 3.5: a) Hydrographic section obtained during PS96 along 76°S with the three mooring locations. Black thin lines give potential density referenced to the surface pressure. The white line marks the surface freezing point temperature to illustrate the ISW layer. Black downward pointing triangles mark the position of the CTD stations used to interpolate the temperature field. b) Progressive vector diagrams of currents measured at the three moorings. The point of origin is offset for each mooring for clarity. The color shading denotes potential temperature (20 mab) and black upside down triangles mark the transition between the different phases (defined in section 3.2.2).

sensor, while temperatures at the lower sensor remain at the surface freezing point or below. During the second phase, lasting from mid-March to July in 2014 and 2015, the bottom temperature also increases due to advection of MWDW. Maximum temperatures at both sensors are between -1.5°C and -1°C but are reached about one month earlier at the upper sensor, which suggests a deepening of the warm inflow with time. The end of this phase is marked by temperatures decreasing down to the surface freezing point marking the onset of the third phase. With temperatures remaining at the surface freezing point and salinity

increasing gradually, this third phase lasts until October. The forth phase denotes the appearance of ISW at the lower sensor, while the upper layer salinity decreases and temperature stays constant until it starts to increase in January (Phase 1). A schematic in Figure 3.9 visualizes the four phases.

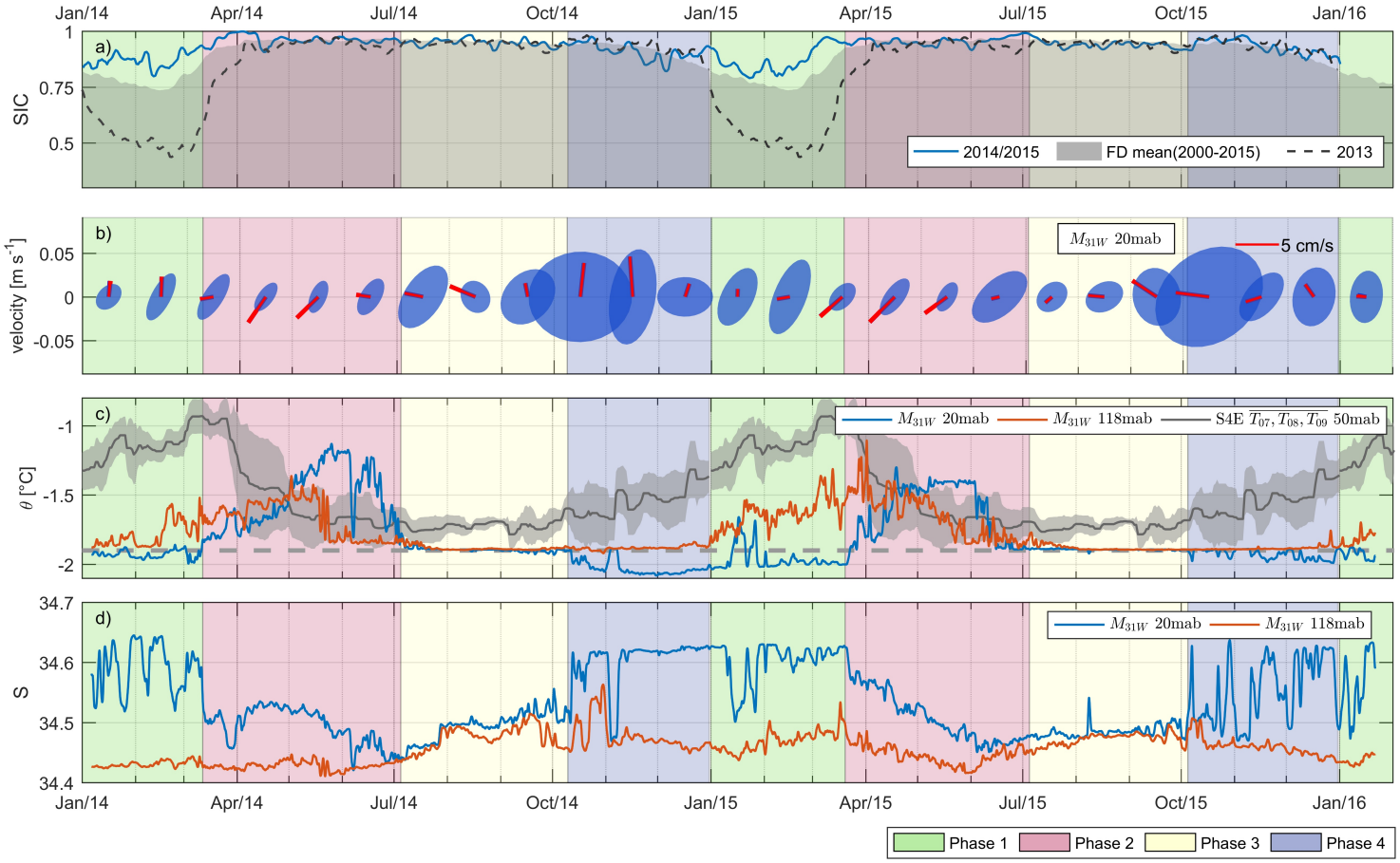

Figure 3.6: a) Daily sea ice concentration (SIC) from the Integrated Climate Data Center (ICDC) averaged over 25°W-40° W and 74.5°S-78.5°S. b) Monthly mean current speed from M_{31W} at 20 mab with variance ellipses derived from low-pass filtered (34h) data. The ellipses are centered around zero. c) Low-pass filtered (34h) potential temperature from both sensors of M_{31W} in color and a mean seasonal evolution of temperature with standard deviation (shaded) at 50 mab (419 m) from the mooring S4E at the shelf break. d) Low-pass filtered (34h) salinity from both levels at M_{31W}.

Phase 1 + 2: MWDW inflow in summer

In this section we assess the seasonal evolution of the inflow of MWDW onto the eastern continental shelf, which can be separated into two phases. The first phase is characterized by the first appearance of MWDW at intermediate depth, while the bottom is covered with ISW. The second phase is defined by the onset of inflowing MWDW at the bottom, occurring one or two months after increasing temperatures are observed at the upper instrument.

During the first phase, salinity of the advected water increases slightly with small fluctuations, while the cold layer below shows large variations when the salinity is generally much higher. These variations close to bottom seem to be related to intermittent pulses of denser ISW onto the Eastern Shelf, as the drops in salinity are associated with raises in temperature. The flow at the lower instrument is shown as monthly mean variance ellipses with a mean current vector in Figure 3.6b. The data has been low-pass filtered with a 34 h cutoff frequency in order to remove the effect of semi-diurnal and diurnal tides. While the mean flow is directed westward and then northward in the first phase, it becomes a stronger southwestward flow, associated with the warming at the bottom and a decrease in salinity in Phase 2. The current vector clearly exceeds the variance of the residual flow, indicating a persistent inflow. It can only be assumed that the warming in the intermediate layer is also associated with a southward advection of MWDW from the shelf break.

The temperature-salinity diagram (θS-diagram) in Figure 3.7 shows the evolution of the properties of the warm inflow (black arrows in c and d). While at the upper instrument (Figure 3.7 a,b) the warming occurs predominantly along the mixing line between the fresh WW and denser WDW, which we call MWDW mixing line in the following, the water at the bottom is much more saline when the warming begins. The bottom salinity at the beginning of summer is determined by the density of the cold water occupying the bottom layer during winter and spring. As shown in Figure 3.6, bottom temperatures reach their maximum in May during the second phase. They are found on the MWDW mixing line in the θS-diagram, being slightly denser than the water above, which shows maximum temperatures about one to two months earlier (transition Phase 1 to Phase 2). At both sensors the cooling toward the end of Phase 2 occurs along the MWDW line, hence is caused by the admixture of WW/ESW. The time series in Figure 3.6 shows that the temperature drop often occurs within a few days from over -1.5°C

to the surface freezing point and happens earlier at the upper sensor than at the lower.

Darelius et al. (2016) find a strong correlation between the warm inflow at 77°S and the wind along the main wind direction (easterly) at Halley Research Station. Performing the same analysis with our mooring data does not give a significant correlation during the inflow period or the warm period in general.

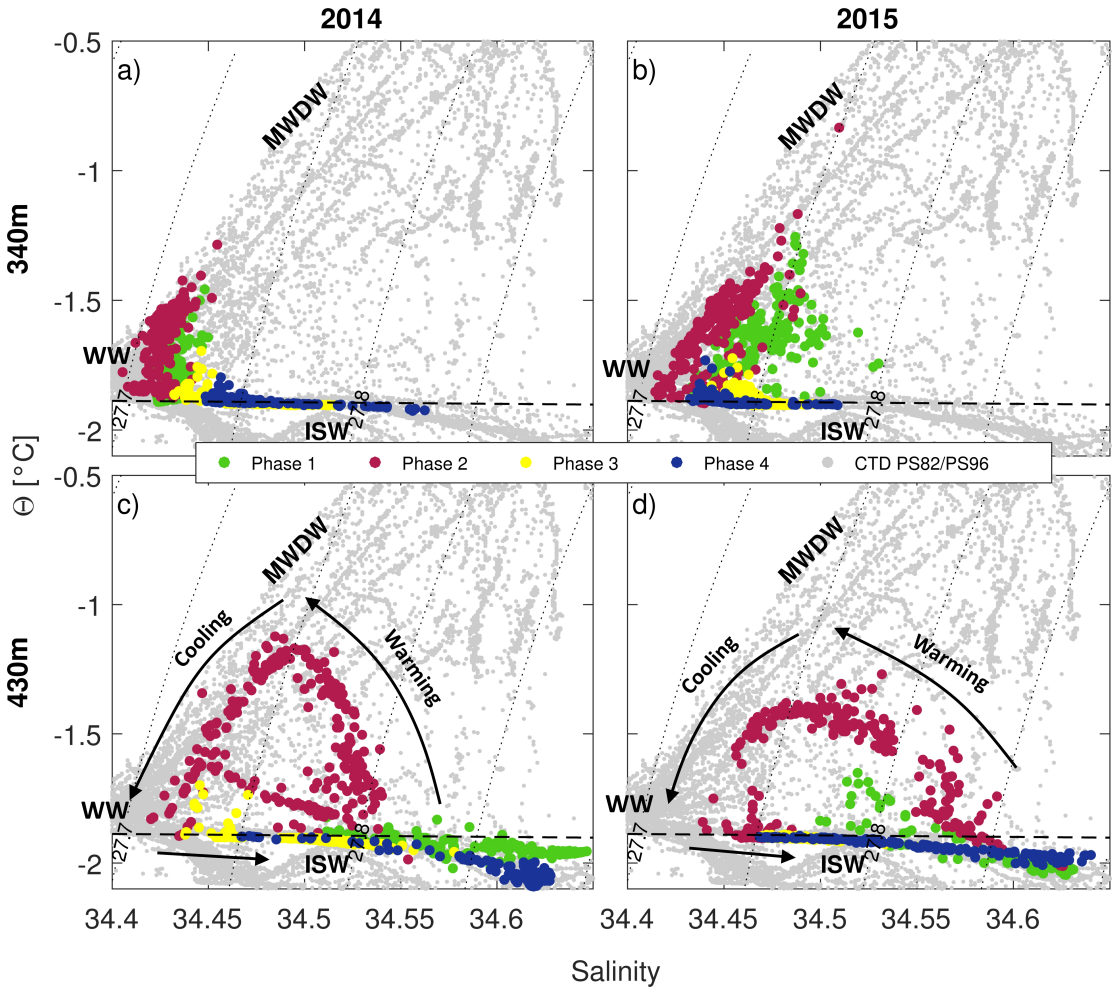

Figure 3.7: θS-diagrams showing data from the upper (118 mab) and lower (20 mab) sensor at M_{31W} (upper and lower panels, respectively) in 2014 (left panels) and 2015 (right panels). The color code indicates the different phases of the seasonal cycle. Data from CTD-profiles obtained during PS82 and PS96 are shown in gray. The thin dotted black lines are potential density lines referenced to the surface and the thick dashed lines are the surface freezing point. Characteristic water masses are labeled in each panel. Arrows in c) and d) indicate time evolution.

Phase 3: winter time convection and shifting circulation

The onset of the third phase is marked by temperatures around the surface freezing point measured at both sensors, with a marginal difference in salinity (~ 0.01). This weak stratification is consistent with observed (*Årthun et al.*, 2013) and modelled (e.g. *Petty et al.* (2014)) deep mixed layers in winter, reaching the bottom of the continental shelf ($\sim 500\,\mathrm{m}$ depth).

Simultaneously to the end of the warm inflow and the development of weakly stratified water column, we observe a change in circulation at M_{31W}, where the mean current shifts to easterly flow ($0.02\,\mathrm{m\,s^{-1}}$) in June and stays easterly to southeasterly during this phase. *Årthun et al.* (2012) observe a salinity gradient of 0.16 between the northern and southern Eastern Shelf (300 km) in the upper 300 m during winter. This gives a density gradient that could potentially drive the westward flow. The magnitude of the baroclinic forcing is however small, and the resulting current ($u_{bc} = -\frac{1}{f\rho_0} gh\frac{\Delta\rho}{\Delta y}$) would be less than $1\,\mathrm{cm\,s^{-1}}$ at the bottom, which is less than half of our observed current. Hence, there must be a barotropic westward component as well.

The filtered variance ellipses are larger and more circular,compared to Phase 2, indicating a variable flow with westward residual currents on the eastern continental shelf in winter, which in some months also exceed the variance ellipses.

Once the temperatures have reached the surface freezing point temperature, the salinity starts to increase steadily at both levels for about three months (longer at the upper sensor). A maximum increase of 0.095 is observed at the upper sensor in 2014 and a minimum increase of 0.046 at the lower sensor in 2015. The maximum salinity reached toward the end of the phase is around 34.51, which is less saline than the ISW filling the Filchner Trough. The increase in salinity is in agreement with the results of *Årthun et al.* (2013) who derive local sea ice formation rates from seal data at 78°S in 2011.

Phase 4: ISW outflow

From October onward ISW appears at the lower instrument of M_{31W} and a rapid increase in salinity from 34.5 to over 34.6 is observed. The persistent presence of the ISW, as observed in 2014, is associated with a northward flow which is especially strong in October and November with a mean velocity of $0.05\,\mathrm{m\,s^{-1}}$ and short events with velocities of $0.1 - 0.2\,\mathrm{m\,s^{-1}}$. The westward mean flow is maintained only if pulses of ISW enter the shelf (i.e. 2015). In both years, October

is the month with the highest variance, especially in east-west direction compared to the rest of the year.

Temperature at the shallower instrument at M_{31W} stays around the surface freezing point, while salinity gradually decreases (see Figure 3.6a). Surface sea ice melt begins in this phase, however, our measurements are too deep to be directly influenced by this.
The θS-diagram in Figure 3.7 shows the transition from WW to ISW at the lower sensor and the different ISW properties for each year. The whole water column stays cold and dense during this phase.
The seasonal appearance of ISW on the eastern shelf could be associated with e.g. a seasonal change in the ISW layer thickness in the Filchner Trough or a horizontal shift of the ISW interface above the eastern slope of the trough, however, this needs further investigation.

3.2.3 Link to ASF

We mentioned in the introduction that the ASF plays a crucial role in controlling the access of MWDW onto the shelf, which is why we compare the presented data to available mooring data at the shelf break in this section.

The seasonal inflow of MWDW, evident in our time series, agrees with *Årthun et al.* (2012) who present mooring data at the shelf break (see Figure 2.1, S4E) and find that MWDW crosses the sill along the 400 m isobath between January and May, with strong interannual variability with respect to the length of the inflow period. Our constructed mean yearly temperature time series (see section 2.1.2) from S4E (2007-2009) is plotted in gray in Figure 3.6c with the associated standard deviation in gray shading and it is repeated for each year of our time period. A steady increase in temperature can be seen between January and April, roughly covering the first phase, where the warming shows a very similar gradient but the temperatures at the shelf break are roughly 0.5°C higher, which is to be expected as WDW mixes with shelf waters once entering the shelf region to form MWDW. The shelf break mean temperature drops rather abruptly in April by 0.5°C, however, the high standard deviation (STD) indicates the interannual variability of the length of the inflow period and the drop occurs between April and May.

The maximum bottom temperatures at 76°S are reached in May, i.e 1 to 2

months after the maximum at S4E. An estimation of the advective time scale based on the distance between S4E and the moorings at 76°S (150 km) and the observed mean inflow speed at M_{31W} between April and July ($2.7\,cm\,s^{-1}$) yields just over 60 days, which is in rough agreement with our observations of a 1 to 2 months delay.

In Figure 3.8a we additionally compare the mean time series at S4E with data at M3, which is located on the continental slope just east of the entrance to the Filchner Trough (see Figure 2.1) at the 725 m isobath. During the period of overlap (6 months in 2009) the temperature evolution at S4E is similar to what is observed at M3, although temperatures are slightly lower at S4E. The sudden drop in temperatures in April is manifested at S4E 419 m and M3 570 m depth, while the shallower record from M3 (417 m depth) shows a much more gradual decrease and significantly lower temperatures. This suggest that the water at S4E (419 m) originates from a depth below 500 m.

During Phase 3 the temperature at the shelf break remains around −1.7°C, i.e. little or no MWDW is able to enter the shelf during this phase. *Årthun et al.* (2012) suggest that a stronger negative wind stress curl in winter causes stronger Ekman downwelling at the shelf break, which in turn depresses the isopycnals, leading to a seasonal change in density over the upper part of the continental slope (*Darelius et al.*, 2014b). The seasonal evolution of the shelf break isotherms is also indicated in the schematic in Figure 3.9.

It is unclear what role sea ice plays in the ocean dynamics at the shelf break. Sea ice influences the atmosphere-ocean momentum transfer (*Andreas et al.*, 2010) and its formation/melting can change the θ-S properties of the upper ocean and affect the shape and position of the slope front, which in turn plays a role in controlling the access of MWDW onto the shelf (*Nøst et al.*, 2011). *Daae et al.* (2017) find in an idealized model study, that the establishment of an upper eddy overturning cell in summer, which is associated with the fresh water layer due to sea ice melt, leads to a relaxation of the thermocline and thus to a stronger inflow of MWDW onto the continental shelf. Figure 3.6a) shows the onset of sea ice melt is in November and lasts until February. During that time a fresh surface layer would be present and could contribute to the heaving of the isopycnals.

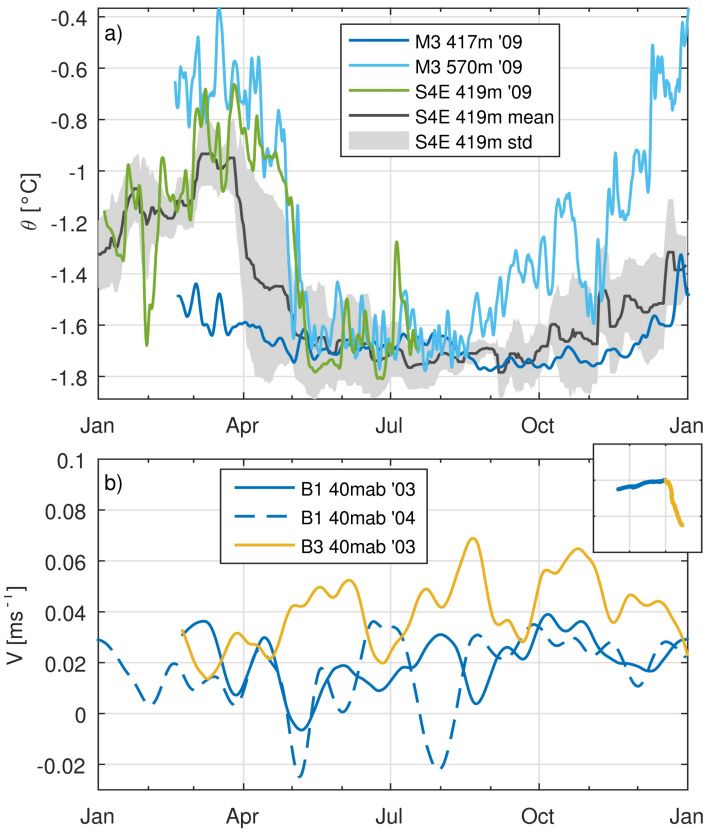

Figure 3.8: a) Potential temperature time series (low-pass filtered 7 days) at M3 (blue) and S4E (green) from 2009. In gray the constructed mean annual temperature time series at S4E (2007-2009) is shown with the associated standard deviation (gray shading). b) Low-pass filtered (28 days) velocity in the mean flow direction at moorings B1 and B3. The mean flow direction is shown in the small sub-panel as progressive vector diagram.

3.2.4 Interannual and spatial variability

In order to evaluate the robustness of the seasonal cycle, we analyze the year-to-year and the spatial variability of the described phases on the Eastern Shelf.

Figure 3.10 shows hydrographic potential temperature sections at 76°S from the years 2013 (ES060), 2014 (PS82) and 2016 (PS96). All sections have been obtained in January (see Figure 3.10 for dates). A clear difference can be seen in the presence of MWDW on the shelf at this time. In 2013, warm water is found all along the eastern flank of the trough with a density of 27.75 kg m^{-3}, overlaying the ISW layer over the slope and extending to the bottom on the eastern shelf (30.6°W). In contrast to that, only a small trace of advected MWDW can be

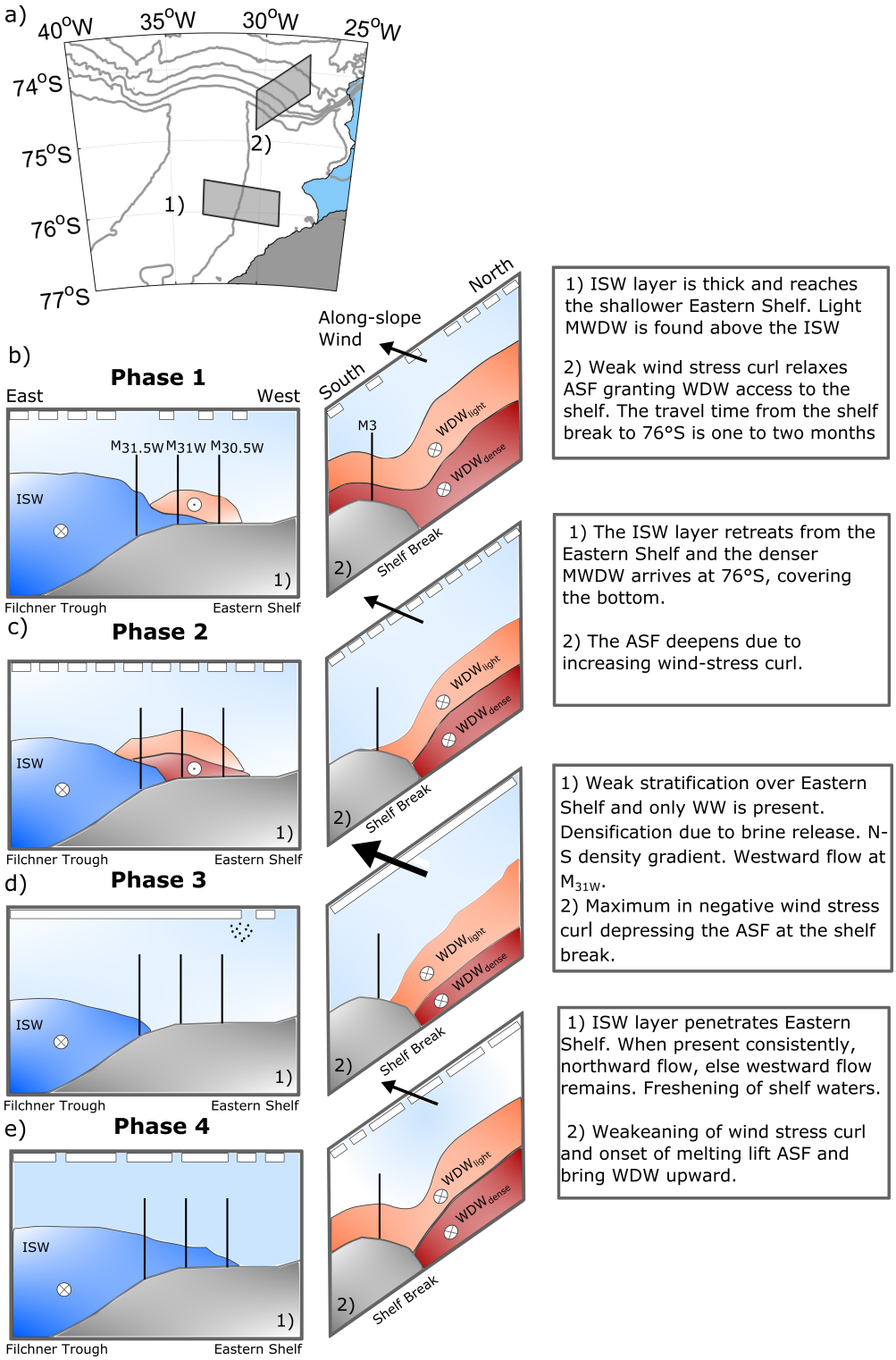

Figure 3.9: Summary sketch of the four defined phases along two representative sections. 1) Section at 76°S comprising our moorings showing the seasonal changes of the water masses along the eastern flank of the Filchner Trough 2) Cross-section at the shelf break to describe the seasonal evolution of the Antarctic Slope Front.

seen in 2014 over the shelf above the 27.7 kg m^{-3} pycnocline. Two years later, MWDW is observed in the intermediate layer (σ_θ < 27.75 kg m^{-3}), while the bottom is still covered with ISW. This shows that there is a strong interannual variability regarding the onset and strength of the flow of MWDW onto the shelf, in agreement with *Årthun et al.* (2012).

Figure 3.11 shows temperatures (a,b), salinities (c,d) and monthly mean velocity vectors (e) of the three moorings at 76°S ($M_{30.5W}$, M_{31W}, $M_{31.5W}$) and the mooring at 77°S ($M77_5$). Comparing the time series at M_{31W} for 2014 (dark gray) and 2015 (light gray) shows that there is interannual variability of the temperature evolution during Phase 1 and 2, especially at the upper instrument. Here, the warming starts earlier in 2014 and shows a gradual increase in temperature until April, followed by a gradual decrease, whereas in 2015 maximum temperatures are reached in May and drop within a short period of time, similar to the bottom observations in both years. Similarly, Figure 3.8 shows an abrupt drop in temperature at the deeper level at M3 (570 m), while the shallower record (419 m) shows a gradual decrease. This might hint toward a deeper source (i.e. 570 m depth) for the water at the upper sensor at 76°S in 2015, which is otherwise supplied by the shallower waters (i.e. 400 m depth) at the shelf break.

Furthermore, it can be seen that the warming signal at M_{31W} (dark and light gray) is shifted forward in time compared to $M_{30.5W}$ (dark and light blue) at both instruments. The shift is more pronounced at the bottom. This suggests that the MWDW reaching M_{31W} is advected from the shallow continental shelf east of the trough rather than along its eastern slope. We correlated the low-pass filtered (34 h) temperature time series from the lower instruments for Phase 1 and 2 and find the highest correlation between M_{31W} and $M_{30.5W}$($r = 0.79$) at a lag of 9.5 days. We use this time lag and the distance between both moorings (14 km) to derive a mean advective velocity scale for the signal, yielding 0.016 m s^{-1}. This number lies within the mean absolute velocities of M_{31W} (0.017 m s^{-1}) and $M_{30.5W}$ (0.01 m s^{-1}). In Phase 1 the MWDW coming from the shelf cannot reach M_{31W} due to the presence of the ISW. Only when the ISW layer retreats, can the MWDW reach M_{31W}.

The moorings $M_{31.5W}$ (580 m depth) and $M77_5$ (500 m depth) are located at the eastern flank of the Filchner Trough compared to M_{31W} and $M_{30.5W}$, which are on the flatter Eastern Shelf. The bottom is generally covered with ISW over the slope (see Figure 3.11b, red, orange and green). However, as shown by *Darelius*

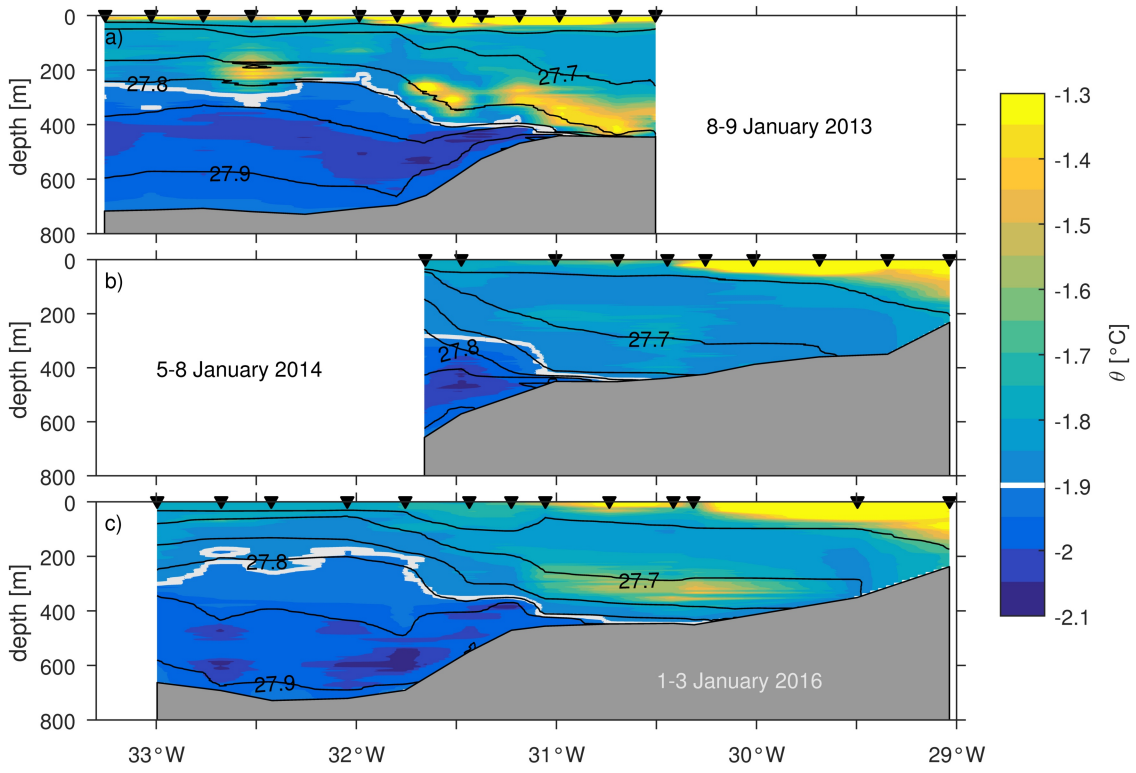

Figure 3.10: Potential temperature sections along 76°S obtained during three cruises: 2013 (a, ES060), 2014 (b, PS82) and 2016 (c, PS96). Black isolines are potential density lines referenced to the surface. The white line indicates the -1.9°C isotherm to visualize the ISW layer ($\theta < -1.9$°C).

et al. (2016), in 2013 MWDW was observed in the vicinity of the Filchner Ice Shelf front, which is manifested in the two warm peaks in April and May in Figure 3.11a (green) and which they attribute to exceptionally strong winds and little sea ice during this year. The salinity evolution at $M77_5$ is very similar to M_{31W}, while at $M_{31.5W}$ it is more or less constant at over 34.6 (Figure 3.11).

Both intermediate instruments over the eastern flank of the trough (Figure 3.11a, $M_{31.5W}$ & $M77_5$) show ISW at the beginning of the year but a warming is observed from February on, together with a decrease in salinity, similarly to the upper instruments on the Eastern Shelf. In agreement with the definitions of Phase 1 and 2, also at $M77_5$ the warming starts earlier at intermediate depth compared to the bottom. By June, temperatures have dropped below -1.8°C and stay close to the surface freezing point for several month while salinity in-

creases, matching the Phase 3 definition. Also a sudden shift from southward to north-/northwestward flow is observed at both depth at $M77_5$, suggesting a general change in circulation on the shelf in winter (will be discussed in more detail). The bottom instrument at $M_{31.5W}$, being deeper than the instrument at $M77_5$, is governed by the outflowing ISW all year around, without a strong influence from the processes observed on the adjacent shallower shelf.

We defined Phase 4 by the appearance of ISW at the lower instrument on the Eastern Shelf (M_{31W}), which we attributed to a seasonal change of the ISW layer thickness over the eastern flank of the trough. Also at $M77_5$ short pulses of ISW are detected at the intermediate instrument starting in October, suggesting that the ISW layer rises to shallower depth. This again is confirmed by our results at M_{31W}.

Furthermore, the ISW observed at M_{31W} has very similar properties to the ISW at $M_{31.5W}$, which emphasizes the hypothesis that the ISW layer penetrates across the Eastern Shelf during this phase. In 2014 it even reaches $M_{30.5W}$, however, here the properties suggest an admixture of warmer and fresher shelf water. Hence, the ISW layer is fading out in this region.

[2]

3.3 Pathways of Modified Warm Deep Water

The mooring data confirm the seasonal warm inflow along the eastern flank of the Filchner Trough as suggested by other studies before and I could shed light onto the general seasonal cycle, which revealed to be very distinct and driven by several different forcing mechanisms. Furthermore, it is important to understand the pathways MWDW takes onto the continental shelf. The hydrographic sections in Figure 3.2 show the presence of MWDW along the eastern flank of the Filchner Trough at roughly 400 m depth. This inflow is driven by the conservation of vorticity; when the westward flowing ASC encounters the mouth of the trough it faces a deepening of the bathymetry, as the shallower isobaths turn southward into the trough. In order to conserve its vorticity, the flow has to turn south (increasing magnitude of f). Due to the sloping isopycnals in the trough, a horizontal density gradient over the eastern flank can set up a southward baroclinic current (thermal wind) that transports MWDW further south toward the ice shelf front.

[2] The part of publication (*Ryan et al.*, 2017) finished here.

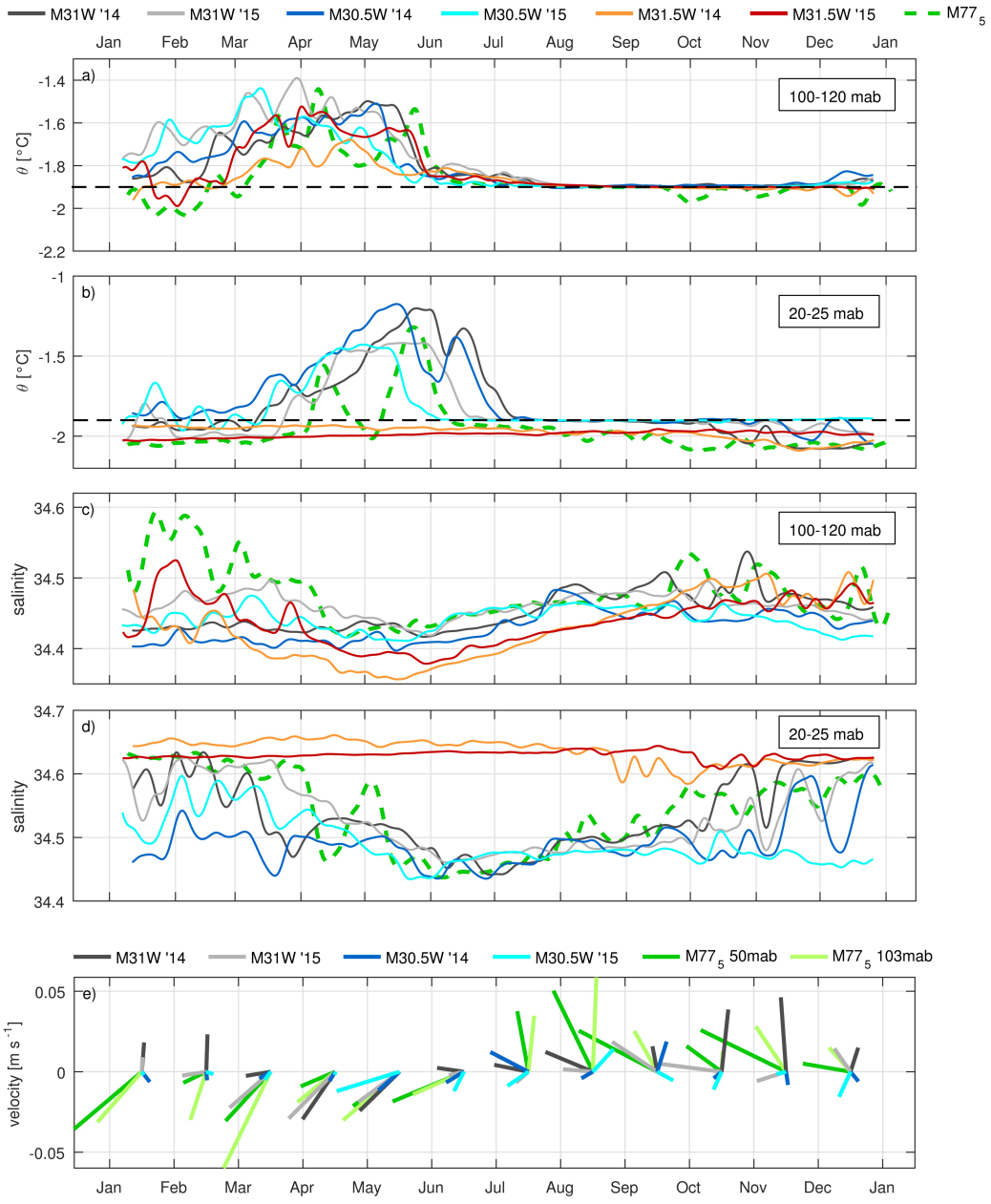

Figure 3.11: Time series (low-pass filtered 14 days) for different years of potential temperature and salinity near the bottom (b,d) and roughly 120 mab (a,c) and monthly mean current vectors (d) from different depths (50 & 103 mab) at $M77_5$ and the moorings at 76°S.

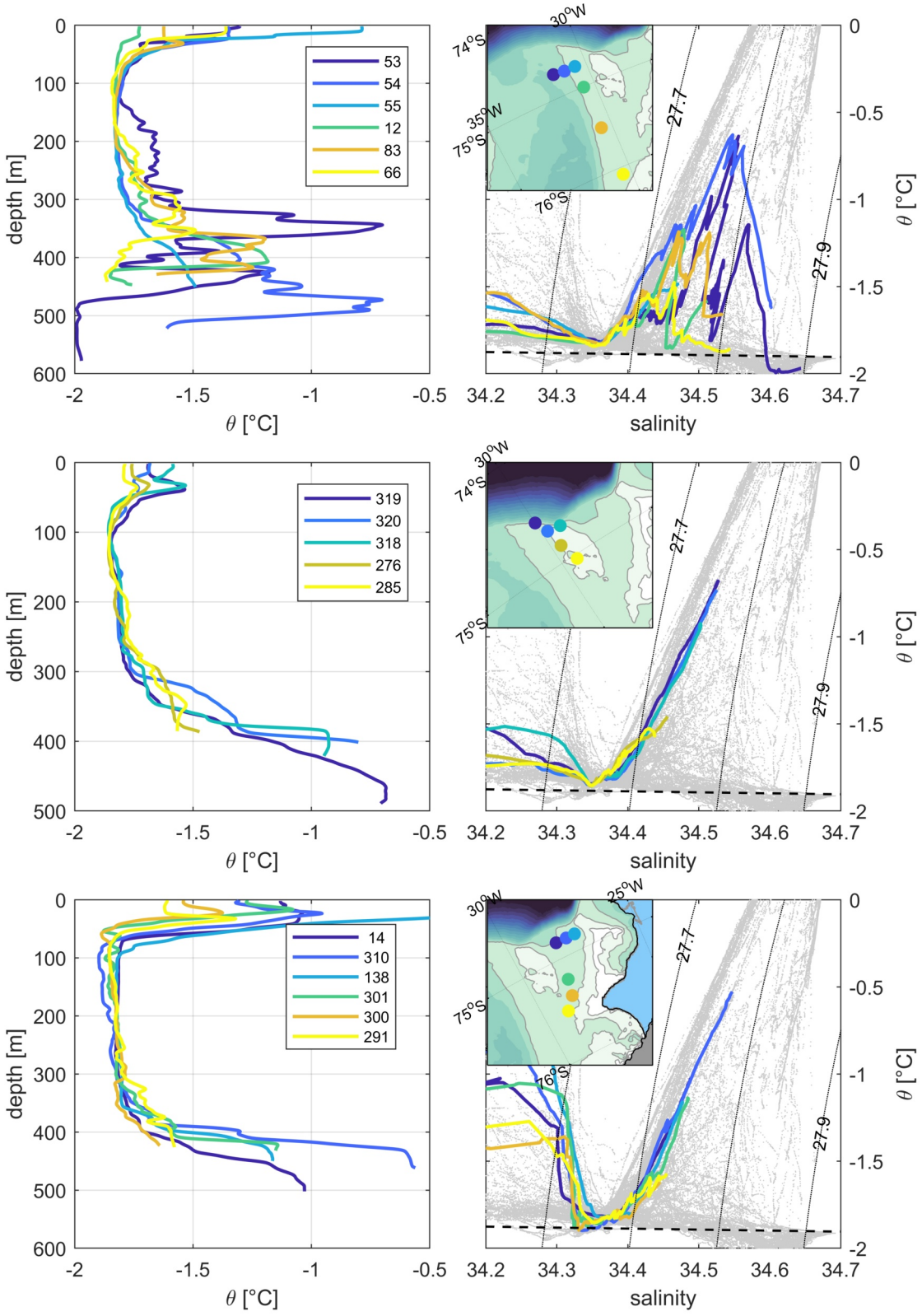

Figure 3.12: Selected CTD stations along the eastern slope of the Filchner Trough (a) the bank (b) and the eastern channel (c). Grey dots in background are all CTD station from PS82 and PS96 as a reference. The thick, dashed line indicated the surface freezing point and thin, dotted lines give potential density referenced to the surface in 0.1 kg m^{-3} intervals.

Figure 3.12a shows vertical temperature profiles and a θS diagram of selected stations along the eastern slope of the trough. The temperature of the MWDW is gradually decreasing from the sill toward 76°S and additionally freshening, which indicates mixing with fresh shelf waters. All stations show the influence of ISW at the bottom, i.e., WDW does not enter the trough along the bottom at the time of measurements. As shown earlier, the moorings at 76°S show a delayed warming and southward flow along the bottom, starting in March. Generally the water column is very disturbed and different water masses with similar densities are found close to each other. This is especially visible at station 53, which is located in the area of steep isopycal interfaces (see Figure 3.2b), where mixing is likely to occur. Hence, the warm water entering via the centre of the trough is prone to undergo significant modification due to the immediate presence of ISW.

The inflow via the eastern flank of the trough is regarded as the main inflow path of MWDW. Temperature profiles east of the trough's mouth suggest that MWDW also reaches onto the continental shelf there, where a little rise is found with depth shallower than 400 m (see Figure 3.12b). The profiles show an increase around 300 m depth with maximum temperature at the bottom. A similar picture, where all profiles indicated the influence of WDW below 350 m depth, is observed east of the rise. Here, bathymetry shows a small channel with a depth of up to 500 m at the shelf break, however, becoming shallower toward the south ($\approx$ 400 m), which could prevent a permanent onshore flow. In θS space, a clear MWDW signature can be seen and compared to the profiles at the sill no mixing with denser water has taken place, as only the much fresher/lighter ESW is present. This hints toward pathways that transport 'purer' MWDW across the continental shelf to the south, especially when the depth of the ASF decreases during summer as shown earlier. A time lag between the moorings $M_{30.5W}$ and M_{31W} already indicated a southward propagation of the MWDW over the shallower shelf instead of along the slope of the trough.

Additional evidence of a warm inflow across the shallower shelf east of the Filchner Trough is provided by temperature profiles obtained by a Weddell seal in March/April 2014 (see Figure 3.13). All profiles show temperatures above -1.5°C in the lower layer, which is higher than the maximum temperatures observed earlier in the year on top of the rise. This is consistent with the maximum temperatures observed in March at the shelf break as shown earlier (Figure 3.6) and also lays in the temperature range of the maximum temperatures in the mooring time

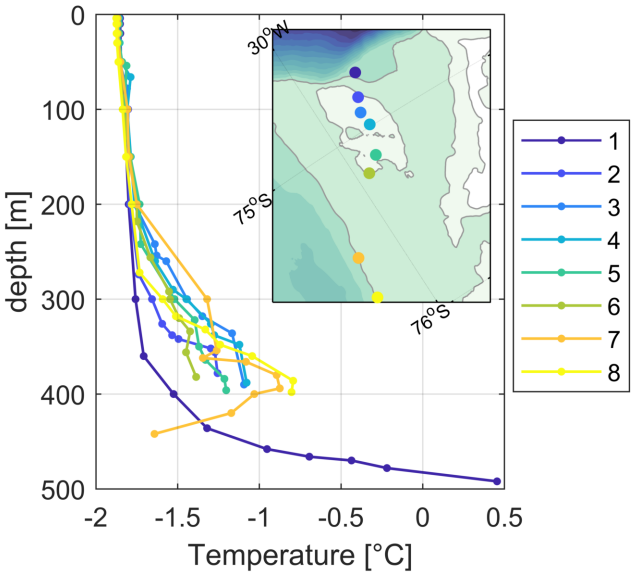

Figure 3.13: Selected temperature profiles from a CTD-tagged Weddell seal between 25th March and 14th April 2014. Bathymetry is shown in 100 m intervals with thin grey contours between the 500 and 0 m isobath.

series at 76°S. The warmest temperatures (T> −1°C), however, are found at the seal profiles 7 and 8, located above the 500 m isobath with the maximum in 400 m depth, overlaying much colder water which is likely a mixing product of MWDW and ISW. These temperatures exceed the maximum values at the moorings, which are placed over shallower (M_{31W} & $M_{30.5}$, ≈ 450 m) and deeper ($M_{31.5W}$, 580 m) isobaths. Seal profiles at 76°S close to the 500 m isobath show a similar distribution (see Figure 2.3) and a comparison to the mooring measurements at the same time suggest that either the warm core lays below the upper instrument and is not capturing the warmest water or a warmer core of MWDW is located over the 500 m isobath generally, hence, between our mooring locations. Whether this warm water flows south or north as part of a suggested recirculation cannot be inferred from this data.

3.4 Ice Shelf Water outflow

The ISW outflow has long been the main study focus in the Filchner region because of its importance for the deep water formation in the Weddell Sea and, ultimately, the global ocean. While the focus has slightly shifted toward the MWDW inflow and its threat for FRIS, pathways and variability of ISW are still

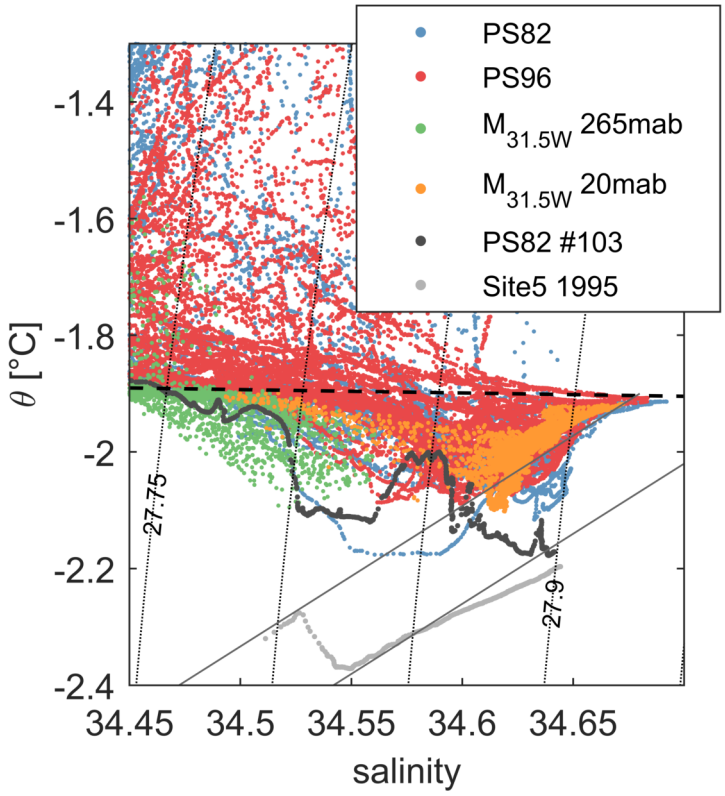

Figure 3.14: θS diagram comprising all CTD data from PS82, PS96 and from mooring $M_{31.5W}$ upper and lower microcat. Grey dots are from a CTD profile through a bore hole south west of Berkner Island in 1995. The thick black dashed line, indicates the surface freezing point temperature and thin grey lines in are Gade lines with a source salinity of 34.68 and 34.78. Thin black dotted lines represent potential density referenced to surface pressure.

not fully understood due to the sparse data coverage. Especially, the processes controlling the ISW outflow across the ice shelf front are poorly understood. as well as the hydrography along the western flank of the trough, where heavy sea ice cover all year around does not allow for direct ship measurements. In this section, I will use recent and historic hydrographic data, including ship-based and seal-tag CTD data as well as oxygen isotopes, to perform a more detailed analysis of the ISW observed in the Filchner Trough. Amongst the remaining questions is the one about the source region of the ISW water found in the Filchner Trough. The concept of the Gade line gives information about the salinity of the source water mass of ISW and, hence, its formation region (see section 2.1.5). Figure 3.14 shows a θS diagram of CTD data from PS82 and PS96 together with mooring data from $M_{31.5W}$, whose lower instrument was surrounded by ISW all year around. The

ISW water properties are very similar throughout all data sets and the majority of the data lie on the Gade line with a source salinity of 34.67. This indicates that HSSW formed on the Berkner Bank is the source water mass for most of the ISW filling the trough. The mooring data shows no large deviations from the Gade line throughout the year. Close to the surface freezing point line data from both cruises shows deviation from the Gade line toward higher salinities, which implies the direct influence of HSSW. It was discussed earlier that HSSW is found at the bottom of the Filchner Trough.

Furthermore, I added data from a CTD profile taken through a hot-water drilled hole southwest of Berkner Island (Site 5) recorded in 1995 (*Nicholls et al.*, 2001). the CTD-profile shows a two layer system with the upper layer laying on the same Gade line as our data and a lower layer with higher source salinities around 34.75, indicating a source in front of Ronne Ice Shelf. This implies that the majority of ISW present in the Filchner Trough during our two expeditions is related to the upper layer at Site 5. However, there are a few profiles obtained during PS82, which hint toward ISW with higher source salinities. One profile in particular (#103, dark grey in Figure 3.14) shows bottom values that lie on the same Gade line as the lower layer at Site 5. This profile is from our most southern section in the centre of the basin, where an ISW plume is found below 1000 m depth (see Figure 3.2, station 103). Geostrophic velocity estimates (not shown) suggest a southward flow of this core, which would be consistent with a cyclonic bottom circulation described by others (*Carmack and Foster*, 1975; *Darelius et al.*, 2014a).

As the hydrographic sections show, the whole Filchner Trough is filled with ISW, however, extra cold lenses are found over the eastern slope. This is in agreement with *Darelius et al.* (2014a) who showed the existence of a cold ISW plume flowing north over the eastern flank, which prior had thought to be located mainly along the western side of the trough. Oxygen isotope measurements from PS96 show lower values associated with these cold lenses in the sections at 76°S and 75°S (see Figure 3.15 a) and b) respectively), suggesting that they contain 'purer' ISW than the surrounding water, since glacial ice is strongly depleted in δ^{18}O. This hints toward a more direct pathway from the cavity of these plumes, where less mixing with surrounding waters occurs. *Darelius and Sallée* (2018) suggest a persistent outflow of ISW at the eastern side of the FIS front. Generally, the whole ISW layer is governed by much lower values, than other water masses

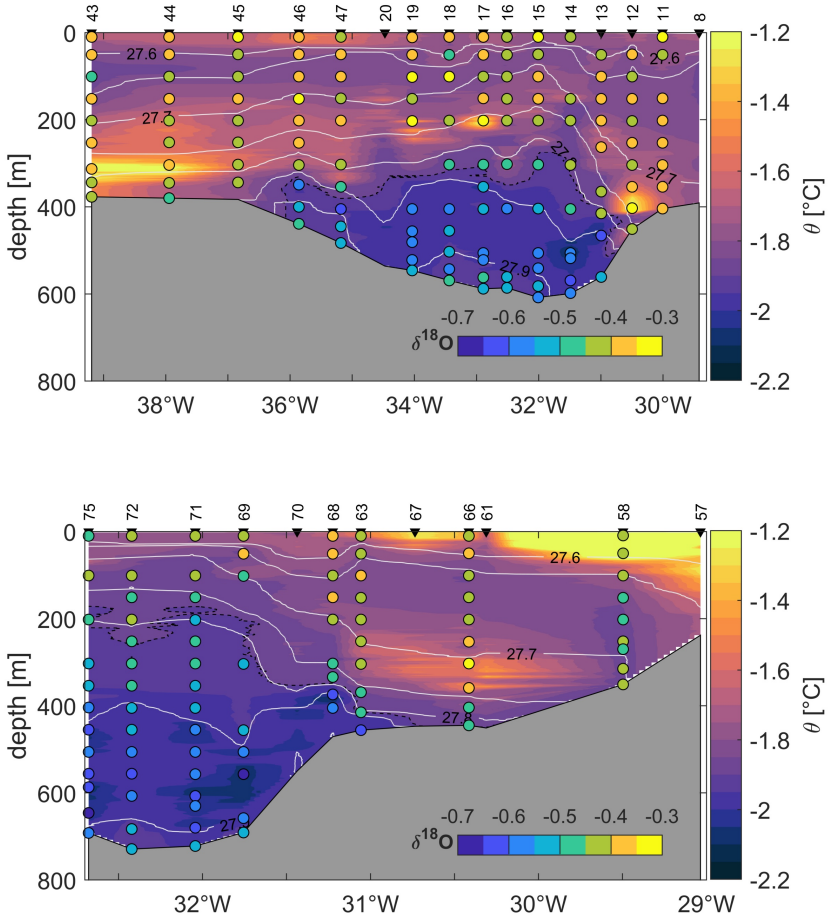

Figure 3.15: Potential temperature section from PS96 at a) 75°S and b) 76°S with δ^{18}O data as scattered dots. Thin white contours represent potential density referenced to surface pressure in 0.05 kg m^{-3} intervals and the thin dashed black lines indicates the surface freezing point temperature to mark the Ice Shelf Water (ISW) boundary. The hydrographic stations used are marked by small triangles and the associated station numbers.

present in the region, demonstrating how suitable δ^{18}O is to trace ISW.

Furthermore, the isotope data show increased values in the bottom layer for densities higher than 29.7 kg m^{-3}, which further expresses the direct influence of HSSW, likely formed on the Berkner Bank, in the trough. This signal is especially strong at the 75°S section; CTD data presented above suggested that some HSSW flows directly from the bank toward the sill being only slightly mixed with the surrounding ISW. HSSW found in the deep trough is likely trapped there and is part of the cyclonic bottom circulation proposed by *Carmack and Foster* (1975).

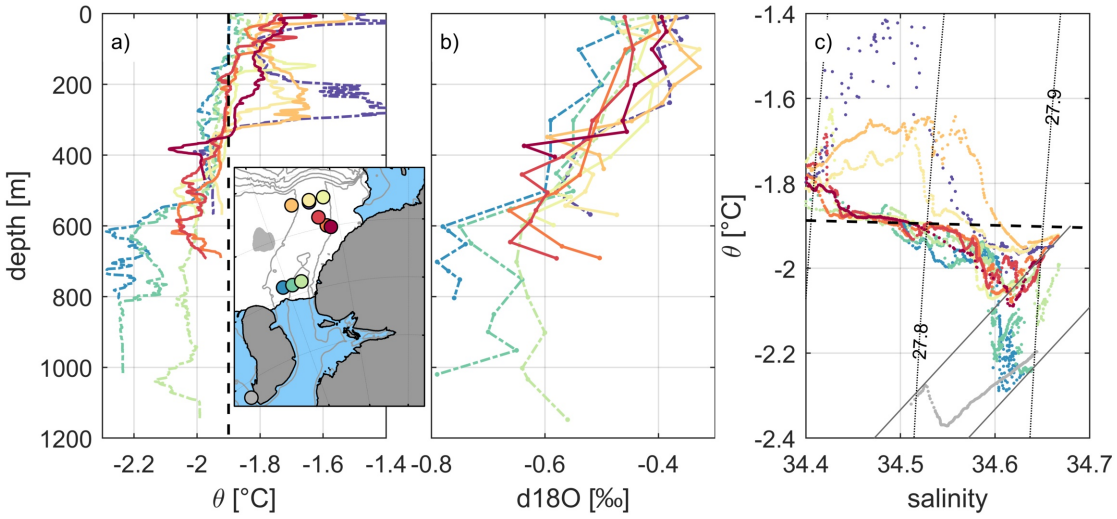

Figure 3.16: a) Profiles of potential temperature θ and b) δ^{18}O from two RV *Polarstern* cruises ANT XII/3 (dashed lines) and PS96 (solid lines) with the positions shown in the map (bathymetry contours in 500 m intervals) c) θS diagram of the same stations as a) and b) except for the grey dots, which are from a CTD profile through a bore hole south west of Berkner Island in 1995. Thick black dashed lines (a,c) indicate the surface freezing point temperature and thin grey lines in c) are Gade lines with a source salinity of 34.68 and 34.78. Thin black dotted lines in c) represent potential density referenced to surface pressure.

δ^{18}O measurements are costly and are not a standard oceanographic tool. *Grosfeld et al.* (2001) recorded a hydrographic section, including δ^{18}O measurements, along the edge of a fast ice field in front of the Filchner Ice Shelf front in 1995. As, unfortunately, no δ^{18}O data are available for PS82, where stations south of 76°S have been profiled, we compare the PS96 data to the 1995 data. Both campaigns obtained samples along 75°S and the δ^{18}O profiles compare well (see Figure 3.16). Thus, I think it is justifiable to compare both data sets despite the time difference.

In 1995, values below $-0.75‰$ where found for the coldest ISW core ($<$ -2.2°C), located at the western slope of the trough between $600 - 800$ m depth (see Figure 3.16a and b, blue dashed line). The three southern profiles from 1995 (dashed lines) exhibit a two layer structure, with lower temperatures and decreased δ^{18}O values below 500 m, being most pronounced the further west the profile is located. The θS diagram reveals that the lowest temperatures represent ISW with source salinities above 34.75, hence originating off Ronne Ice Shelf and furthermore having similar properties as the lower layer at Site 5. The interface

depth in the profiles coincides with the approximate ice shelf draft of the Filchner Ice Shelf front (Bedmap2,*Fretwell et al.* (2013)) and, thus, hints to a direct outflow of ISW at this location. This is consistent with mooring observations from *Darelius and Sallée* (2018), who found a seasonal (summer) outflow of Ronne sourced ISW at this position.

The eastern profile reveals a cold core below 1000 m, which shows isopycnal interleaving in the θS diagram toward higher source salinities as found further west, however, the δ^{18}O values are not as low. The profile was recorded close to the position of station #103 during PS82, where, similarly, a core was observed below 1000 m revealing traces of higher source salinities (see Figure 3.2g). I suggest that this core is part of the cyclonic bottom circulation of the trough. Little is known about the pathways of the seasonal cold outflow within the trough. I hypothesise, that the ISW flows north along the western flank, while it is modified by mixing with HSSW flowing down the slope of Berkner Bank, becoming part of the cyclonic bottom circulation. In the θS diagram the data lie on a straight line between the cold ISW observed in the west and the HSSW formed on Berkner Bank, indicating direct mixing.

No traces of the Ronne sourced ISW are found at 76°S or anywhere along the eastern flank of the trough, supporting the just proposed circulation. Unfortunately, no data is available from the western slope of the trough, due to the impenetrable ice cover all year around. Again, the seal data is of use, as the same seal introduced earlier also recorded profiles on the western flank of the trough just east of A23-A (Figure 3.17). All three profiles at 76°S were obtained within a time frame of 24 hrs, hence presenting a near synoptical picture (29th/30st June 2014). ISW is found between 300m and 500m depth with two profiles clearly exceeding -2°C and the coldest core being found just below 300 m. The profile further to the north (21st July 2014) only shows a small trace of ISW at this depth, being consistent with our hydrographic section at 75°S showing ISW fading out toward the west (Figure 3.2c). All profiles show increasing temperatures at the bottom associated with an increase in salt, manifesting the presence of HSSW along the western flank during winter. Furthermore, the two profiles upslope of the 500 m isobath show almost uniform high salinity throughout the whole water column, indicating active winter convection. As shown in Figure 2.3 salinity data from seal-tags have bias toward higher salinity, therefore the absolute values in Figure 3.17 are likely too high, in particular at the green profile. However, the

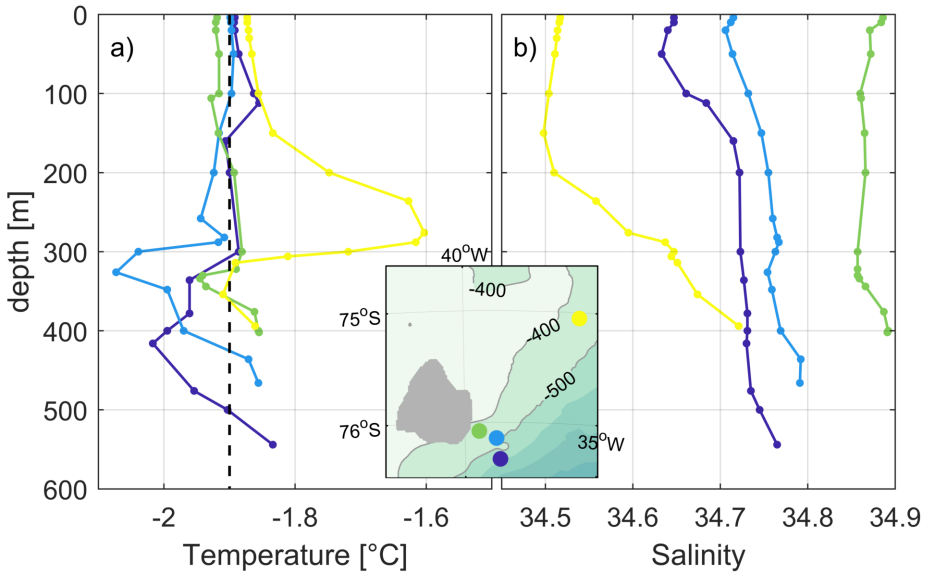

Figure 3.17: In-situ temperature a) and salinity b) profiles (6 hrs mean) from a CTD-tagged Weddell seal (f04) in austral winter 2014 at the western flank of the Filchner Trough. The iceberg A23-A is shown in grey on the map inlay.

validation with mooring data showed that the vertical structure of the profiles is reliable.

3.5 Discussion

The Filchner Trough is an eminent bathymetric feature in the southern Weddell Sea and its role is twofold: by interacting with the ASC it steers warm water of circumpolar origin south toward the FRIS. However, it is much longer known to play a major part in the deep water formation by providing a pathway for the dense ISW into the deep ocean. The hydrographic data presented here integrate into the general understanding of the regional hydrography (*Carmack and Foster*, 1975; *Foldvik*, 2004; *Darelius et al.*, 2014a), which is, however, patched together from various observation programs over a long time span. Beyond this, the data give additional insight.

Consecutive sections from north to south along the eastern flank of the trough provide an overview of the summer hydrography. MWDW enters the trough at the sill where it is hugging the outflowing ISW, creating strong horizontal density gradients. Toward the south, the ISW layer thickens and extends onto the shelf east of the trough, hence blocking a warm inflow along the bottom at this time

and pushing it further onto the shallower shelf, away from the eastern slope of the trough. Only the lightest MWDW is found at 76°S at the beginning of summer. The comparison to a cross-shelf temperature section (3.4) shows, that the warmest WDW off-shelf is located at the continental slope below the 27.8 kg m^{-3} isopycnal, which is found at roughly 1000 m depth just east of the Filchner Trough and therefore below the sill depth. Furthermore, ISW exiting the trough has the same or higher density; hence, it would block the warmest WDW from penetrating the continental shelf, if it were shallow enough. The presented mooring data from 76°S sheds light into the seasonal evolution of this warm southward flow, which will be discussed in the following.

[3]

In this study, I confirm the seasonal inflow of MWDW towards the Filchner Ice Shelf front as suggested by *Foldvik et al.* (1985b), *Årthun et al.* (2012) and *Darelius et al.* (2016). Several studies have pointed out the connection between the warm inflow and a seasonal heaving of the isopycnals at the shelf break, enabling MWDW access to the continental shelf (*Årthun et al.*, 2012; *Darelius et al.*, 2016). I show that the seasonal warming at 76°S can be linked to the temperature evolution at the shelf break.

Whether the MWDW can enter the shelf or not, is not solely controlled by the position of the thermocline at the continental slope but also depends on the water mass density on the Eastern Shelf itself. I show that the seasonal presence of ISW on the Eastern Shelf and the development of a deep, weakly stratified water column in winter cause significant changes in the shelf density structure. Based on results from idealized modelling, *Daae et al.* (2017) suggest, that the southward transport of MWDW is increased for denser outflowing ISW and a higher shelf salinity. The denser water exported from the continental shelf lifts the shelf break isopycnals and connects the warmer WDW over the slope with the shelf, forming a v-shaped front (*Stewart and Thompson*, 2016). Temperatures at the shelf break start increasing at the end of winter, however northward-flowing ISW appears along the bottom at M_{31W} during this time, which will not allow a MWDW inflow at the bottom and no warming is observed yet at the upper

[3]The following part of the discussion is part of a publication in the *Journal of Geophysical Research* with the title *Seasonal cycle of hydrography on the eastern shelf of the Filchner Trough, Weddell Sea, Antarctica (Ryan et al., 2017).*

instrument. We do observe a denser shelf at the beginning of Phase 1 in 2015 ($S = 34.47$) and an earlier warming at the upper instrument compared to the previous year ($S = 34.43$), which would agree with results of *Daae et al.* (2017) and *Stewart and Thompson* (2016). For comparison, salinities in 2013 when the inflow started even earlier and reached the ice front were at 34.43, while they were about 0.05 lower in 2011 (*Darelius et al.*, 2016), where the MWDW did not reach the ice front (*Årthun et al.*, 2013), however, no information is available about the start of the inflow. Observations from the sill (*Darelius et al.*, 2014b) show that in general the density of the outflowing ISW is largest from February until June, which is consistent with the observed inflow period. The results of *Daae et al.* (2017) focus on the Filchner Trough rather than on the Eastern Shelf which is over 100 m shallower and is likely governed by different dynamics.

While the isotherms keep shoaling at the shelf break (and temperatures increase) during Phase 4, the density at the upper instrument decreases gradually until at some point the warming at the upper sensor, hence Phase 1, starts. Only when the ISW retreats in March, does slightly denser and warmer MWDW from greater depth enter the shelf along the bottom. This seasonal change in the ISW layer over the eastern flank of the trough seems to play a considerable role in controlling the warm inflow, next to the seasonal heaving of the shelf break isotherms, even though the forcing is not yet understood.
The interplay between these two factors can drive some of the observed interannual variability of the onset and the strength of the warm inflow in addition to the shelf salinity as discussed above. Weak easterly wind stress at the end of 2012 caused less suppression of the isotherms at the shelf break, allowing an early inflow in 2013 (see Figure 3.10, *Darelius et al.* (2016)). It was suggested that strong wind events with a southward component set up a strong barotropic coastal current, which transported the MWDW on the shelf further south, where it was observed in the vicinity of the Filchner Ice Shelf front in April in that year (*Darelius et al.*, 2016). Their time series at $M77_5$ concurs with our defined phases, which shows that our definition is representative of the hydrography on the Eastern Shelf.

We have discussed the important role of the isotherm depth at the shelf break, which is influenced by the wind stress curl in the region. Additionally, sea ice can influence the position of the ASF by changing the momentum transfer of the wind stress on the ocean (*Andreas et al.*, 2010) and the TS-properties in the upper layer. In 2013 the sea ice concentration was exceptionally low, when the strong

warm inflow occurred (*Darelius et al.*, 2016). These observations are consistent with the results of *Daae et al.* (2017), who suggest that a fresh surface layer in summer leads to a shallow eddy overturning cell that causes a relaxation of the thermocline. Hence, in a year with strong sea ice melt like 2013, a thicker fresh surface layer would develop and cause a stronger lift of the isotherms, leading to the exceptional warm inflow and vice versa. As shown in Figure 3.6, the minimum sea ice concentration during the deployment of our moorings was higher than the 16-year mean and was reached about two to four weeks earlier. The mean sea ice concentration of 2013 was plotted as a reference. If the *Daae et al.* (2017) theory is correct, it would mean than in 2014 and 2015 the inflow was weaker/cooler than the average.

It was found that at 76°S the southward flow of MWDW occurs over the shallow shelf, rather than along the slope of the Filchner Trough as the warm signal appears at M_{31W} with a delay of several days compared to $M_{30.5W}$.
I show that the termination of the inflow is followed by a sudden shift from southwestward to westward/northward flow, which I observed at 76°S and 77°S in June/July (Onset of Phase 3). The fact that there is a distinct current shift from inflow to north-/northwestward flow observed also at $M77_5$, suggests that a change in circulation occurs along the whole eastern flank of the Filchner Trough and the Eastern Shelf during Phase 3 and 4.

The densities on the shelf hint to a weakly stratified water column during winter, which agrees with modelled (*Petty et al.*, 2014) and observed (*Årthun et al.*, 2013) deep mixed layers on the Eastern Shelf. My results suggest that changes in the shelf hydrography might set up a different circulation in winter, preventing a continuous southward flow along the eastern flank of the trough. These observations disprove the suggestions of *Årthun et al.* (2012) of a permanent inflow along the shelf, whose properties depend on the position of the isotherms at the shelf break.

The doming of the ISW layer in the Filchner Trough, as seen in Figure 3.10, creates large horizontal density gradients over the eastern flank, driving a strong baroclinic flow. In winter the ISW layer interface deepens and the upper water column becomes less stratified, hence the horizontal density gradient would weaken significantly and the baroclinic current decline. It is then, that a N-S density gradient could be able to set up a westward flow. During Phase 4, when the ISW layer is thickest and penetrates the shelf the associated northward flow

dominates over the westward flow. If, however, the ISW layer only reaches M_{31W} intermittently, the westward flow remains.

The water flowing westward must be replenished from the east. $M_{30.5W}$ shows a much more sluggish flow at the bottom in winter, suggesting that the westward flow is not as persistent over the whole shelf as seen at M_{31W}. One possibility would be that a stronger coastal current in winter compensates for the westward flow, and indeed observations along the Brunt Ice Shelf (Figure 3.8) in 2003 show a tendency for stronger flow during winter. Another possibility is a weak southward flow over the whole shelf, east of our moorings as compensation. *Carmack and Foster* (1975) suggest a southward baroclinic flow -based on summer data- across the whole Eastern Shelf from the dynamic topography of the 50/300 dbar surface.

Darelius et al. (2014a) show velocity sections obtained with the lowered Acoustic Doppler Current Profiler crossing the eastern slope of the trough at 76°S and 77°S. They confirm a southward flow over the shallow Eastern Shelf, extending over the whole water column. Adjacent to it they observe northward flow over the eastern slope of the trough, which has a velocity maximum within the ISW layer. If this pattern moved seasonally up and down the slope it could cause the observed change in current direction and maybe produce a westward flow in the transition zone. However, it is questionable if in that case the flow would be as persistent as observed. Furthermore, a westward flow would likely turn northward once it reaches the sloping bathymetry of the trough, driven by the conservation of potential vorticity.

The most severe limitation to our our data set is the vertical resolution. With only two instruments recording temperature and salinity and only one current meter at the bottom, our interpretation of measurements is limited to a comparatively coarse-scale view. Specifically, we have no information about the vertical shear in the water column, which would be particularly interesting during Phase 1, when MWDW is observed above the northward flowing ISW. In general only sparse data are available for the eastern shelf.

The mooring time series from different locations which have been used additionally do not overlap in time with our measurements but still remain useful to help to set my data in the broader context of this complex system. My results show that 76°S is a good location to monitor the warm inflow, which seems to reach this location every year, while only under favorable conditions it can penetrate further south. Furthermore, the mooring above the eastern slope ($M_{31.5W}$),

shows the permanent presence of ISW. Changes towards the future projections of *Hellmer et al.* (2012) and *Hellmer et al.* (2017), where MWDW fills the whole Filchner Trough and flows underneath the Filchner Ice Shelf, causing dramatically increased basal melt, will be detected at this location. Whether or not the MWDW observed at 76°S reaches the ice front, can only be assumed from the time it appears at this location. As shown in Figure 3.10 the MWDW arrived at 76°S earlier in 2013 than the following years. In general, I believe that exceptional forcing (*Darelius et al.* (2016)) is needed to transport the MWDW towards the ice front before it is eroded from above in winter.
[4]

There are several reasons why 76°S is a good location to monitor the southward flow of MWDW:

- The mooring observations suggest that MWDW reaches this latitude every year. With the knowledge gained in this study and the work of (*Darelius et al.*, 2016) one can conclude from the timing and the strength of the warm pulse observed at 76°S, whether this water is favoured to reach the ice shelf front or not. Too little is known about the cross-ice shelf front processes in order to say whether it can directly enter the cavity if it would reach this far south.

- The continental shelf becomes narrower at this location. It was shown, that there are indications for MWDW to enter the shallower shelf directly, east of the Filchner trough. Independent of the pathways, all MWDW that possibly enters the continental shelf at different locations would likely be merged into one plume at this point. This allows an easier estimation of the southward heat transport in the future. Due to the low vertical resolution of the mooring data, heat budget calculations have not been performed in this study. However, the moorings have been redeployed with three additional temperature sensors between the upper and lower instruments at each mooring, which will make it possible to analyse heat transport on the Eastern Shelf.

- Furthermore, it was shown that the ISW layer thickens toward the south and also extends onto the Eastern Shelf in winter, where it persists throughout most of the summer. A seasonal change of the thickness or a shift of the

[4]The part of publication *Ryan et al.* (2017) finished here.

interface has been proposed, which is studied in more detail and further supported by *Darelius and Sallée* (2018). The mooring array at 76°S would capture changes, such as a recession or a change in density of the ISW layer, which likely allow a stronger warm inflow. As proposed by modelling studies (*Hellmer et al.*, 2012, 2017), such a development is possible due to reduced sea ice production on the southern Weddell Sea continental shelf and, hence, less HSSW production in the light of the predicted climate change.

So far, there are no indications for a significant lightening of the ISW in the Filchner Trough. Nevertheless, many questions remain to be answered, particularly about the flow across the ice shelf front and the pathways of the ISW within the trough. While a northward flow of ISW over the eastern slope of the trough is meanwhile an accepted feature, it is unclear whether there is also a northward flow over the western slope or not,although its existence used to be commonly believed (*Foldvik and Gammelsrød*, 1988; *Foldvik et al.*, 2001; *Nicholls et al.*, 2001) before the findings of (*Darelius et al.*, 2014a). The first recorded time series in the vicinity of the western FIS front, presented by *Darelius and Sallée* (2018), reveals a seasonal outflow of ISW of Ronne origin in the late summer. No traces of this water, however, are found in the northward flow in the east and while no data is available on the western side, due to the thick sea ice cover.

Three seal profiles, presented in this thesis, do show ISW at the western side (in winter), below 300 m depth and, furthermore, they show the presence of HSSW at the bottom. It is generally thought, that HSSW formed on Berkner Bank enters the trough along its western slope, however, this is only based on a few recent direct observations. *Nøst and Østerhus* (1998) show that the grounding of three tabular icebergs on the Berkner Shelf in 1987/1988 has blocked the direct drainage of HSSW into the Filchner Trough. Today, only one of the icebergs is left (A23-A) and the seal data show that HSSW is able to enter the trough again. By a direct comparison to mooring data, it was shown that the seal salinity data has a large bias of $\mathcal{O}(0.1)$, but it was a consistent error and the profile still captured the correct vertical distribution. Hence, even though the absolute salinity value might be off by $0.1 - 0.15$, the profiles clearly show a temperature decrease associated with a salinity increase toward the bottom, and the properties are within the HSSW range. This once more shows how valuable seal data can be; generally, the oceanographic community has grown more fond of using seals in the last decade (e.g. *Årthun et al.* (2012, 2013)).

Profiles from different years at the eastern side of the deepest part of the trough showed a deep ISW core below 1000 depth, which is likely part of the cyclonic bottom circulation, hence flowing southward. The core's properties lie on a line , in θS space, between the coldest ISW found on the western side of FIS and HSSW of salinities around 34.65, indicating this deep core to be a mixture of both. Based on these results, I hypothesise that the cold seasonal outflow in the west proceeds north along the western flank of the trough. Once the dynamical barrier at the ice front is crossed, there is no obvious process that would deflect the ISW core to the east. The western ISW encounters HSSW flowing down the slope and gradually mixes with it, becoming denser. Due to the trough's geometry, which prevents the dense water to cross the sill, it turns southward, to form a cyclonic bottom circulation.

3.6 Summary

Hydrographic temperature sections along the eastern flank of the Filchner Trough were obtained during two *RV Polarstern* expeditions (PS82 & PS96). The data show a doming ISW layer filling the Filchner Trough, whose thickness is increasing from the sill ($\approx 300\,\mathrm{m}$) toward the FIS front ($\approx 1000\,\mathrm{m}$). A cold ISW is present above the eastern slope of the trough south of 75°S. At the sill, MWDW is found above the eastern slope at the same depth as the outflowing ISW, which is being deviated to the east once encountering the sill, due to potential vorticity conservation. The observed thickening of the ISW layer toward the south, pushed the MWDW up-slope onto the Eastern Shelf. Mooring time series of temperature, salinity and velocity at 76° from 2014 to 2016 reveal a strong seasonal cycle of hydrography on the Eastern Shelf, characterised by four phases. A distinct warm inflow period from summer through to autumn can be described as two phases. At the beginning, MWDW is observed at mid-depth only, while the bottom layer is covered with ISW that extends onto the Eastern Shelf. Toward the end of summer, this ISW layer retreats and a persistent southwestward flow governs the bottom layer. In winter, no MWDW is found on the continental shelf and winter convection creates a weakly stratified water column with temperatures being at the surface freezing point. The seasonal inflow at 76°S is related to the seasonal heaving of the ASF along the continental shelf break, which suppresses the off-shelf WDW below the shelf break depth during winter. An abrupt change in

current direction towards westward flow occurs at the beginning of winter, which is suggested to be driven by a north-south density gradient across the continental shelf. From spring through to summer the ISW layer in the trough extends onto Eastern Shelf, covering the bottom layer at our moorings until the warm inflow starts again. Ship-based and seal-tag CTD data suggests that MWDW can not only enter the continental shelf via the Filchner Trough, but also to the east of the trough toward the end of the summer, when the ASF reaches its shallowest point. Furthermore, the hydrographic data gave further insight into the ISW circulation within the Filchner Trough, suggesting that ISW exiting the FIS cavity at the western side proceeds further north along the western flank of the trough, where it entrains HSSW formed on Berkner Bank in winter and becomes denser. The sill in the north forms a barrier for this dense water, which the follows the isobaths, ultimately forming a cyclonic bottom circulation. This circulation has beed proposed before, however, mainly based on numerical simulations.

4. Model performance: Weddell Gyre circulation and ASF properties

"Essentially, all models are wrong, but some are useful"
George E.P. Box

The observations presented in the previous Chapter gave new insight into the general hydrography of the Filchner Trough with particular focus on the seasonal MWDW flow onto the continental shelf along the eastern flank of the trough. However, it was only the first step in identifying the processes that control the MWDW flow toward FRIS and their seasonality. As the data coverage remains very sparse in this region, it is desirable to use numerical models to improve our understanding.

It was shown in section 3.2.3, that the observed seasonal cycle at 76°S is connected to the ASF properties present at the shelf break. The properties of MWDW associated with the ASF are likely derived further upstream, where WDW enter the Weddel Gyre along its eastern boundary (*Schröder and Fahrbach*, 1999; *Ryan et al.*, 2016). Therefore, I believe it is necessary to model's skill to simulate a realistic large scale Weddell Gyre circulation before studying the cross-shelf exchanges in the southern Weddell Sea.

In section 2.2.2 a newly compiled high-resolution mesh was presented. In the following, I will give an overview of the HIGH simulation with respect to sea ice in the Weddell Sea and basal melt rates around Antarctica and under FRIS. Thereafter, a more detailed analysis of the modelled Weddell Gyre will be presented, with comparisons of low- and high-resolution simulations.

4.1 Sea ice concentration and extent in the Weddell Sea

As mentioned in section 1.4, sea ice modulates the ocean-atmosphere interaction, such as air-sea heat fluxes and momentum exchange. As a results, it influences the upper ocean stratification and water mass properties in the Weddell Sea. In this section, I will briefly assess the seasonal variability of the modelled sea ice in the Weddell Gyre and compare the results to satellite observations.

Figure 4.1 shows maps of climatological mean (1979-2010) seasonal sea ice concentration (sic) in the Weddell Sea in run HIGH (Figure 4.1,b-e) and satellite data (Figure 4.1f-i) from the NOAA/NSIC Climate data Record of Passive Microwave Sea Ice Concentration (*Zwally et al.*, 2002; *Parkinson and Cavalieri*, 2012). Observations show that the Weddell Sea sea ice concentration and extent (Figure 4.1a) undergo a large seasonal cycle, from being fully ice covered during winter (JJA) and spring (SON) to strong melting in summer (DJF), where only the southwestern corner of the Weddell Sea remains ice covered.

The minimum sea ice extent (for sic$>$ 15%) is observed in February with a mean area about $1.5\times10^6\,km^2$, which increases to maximum of roughly $7\times10^6\,km^2$ in September (see Figure 4.1a). The model represents the range and seasonality of the extent well with a slight overestimation of the extent in summer, where the ice covered area remains larger than $2\times10^6\,km^2$. The differences can be seen in Figure 4.1 b) and f) where the modelled field depicts higher concentrations extending toward the centre of the gyre, while observations shows high concentrations being limited to the southwestern corner of the Weddell Sea.

While the modelled sea ice extent in winter agrees well with observations, sea ice concentrations toward the eastern boundary of the gyre are higher in the model with being over 98 % everywhere, compared to observed concentrations between $85-99\,\%$.

4.2 Basal melt rates

One strength of FESOM is the integration of ice shelf cavities. It allows the interaction of the ocean with the ice shelf base and incorporates the resulting modification of water masses that enter ice shelf cavities. These water masses, such as ISW, constitute significantly to the deep and bottom water formation

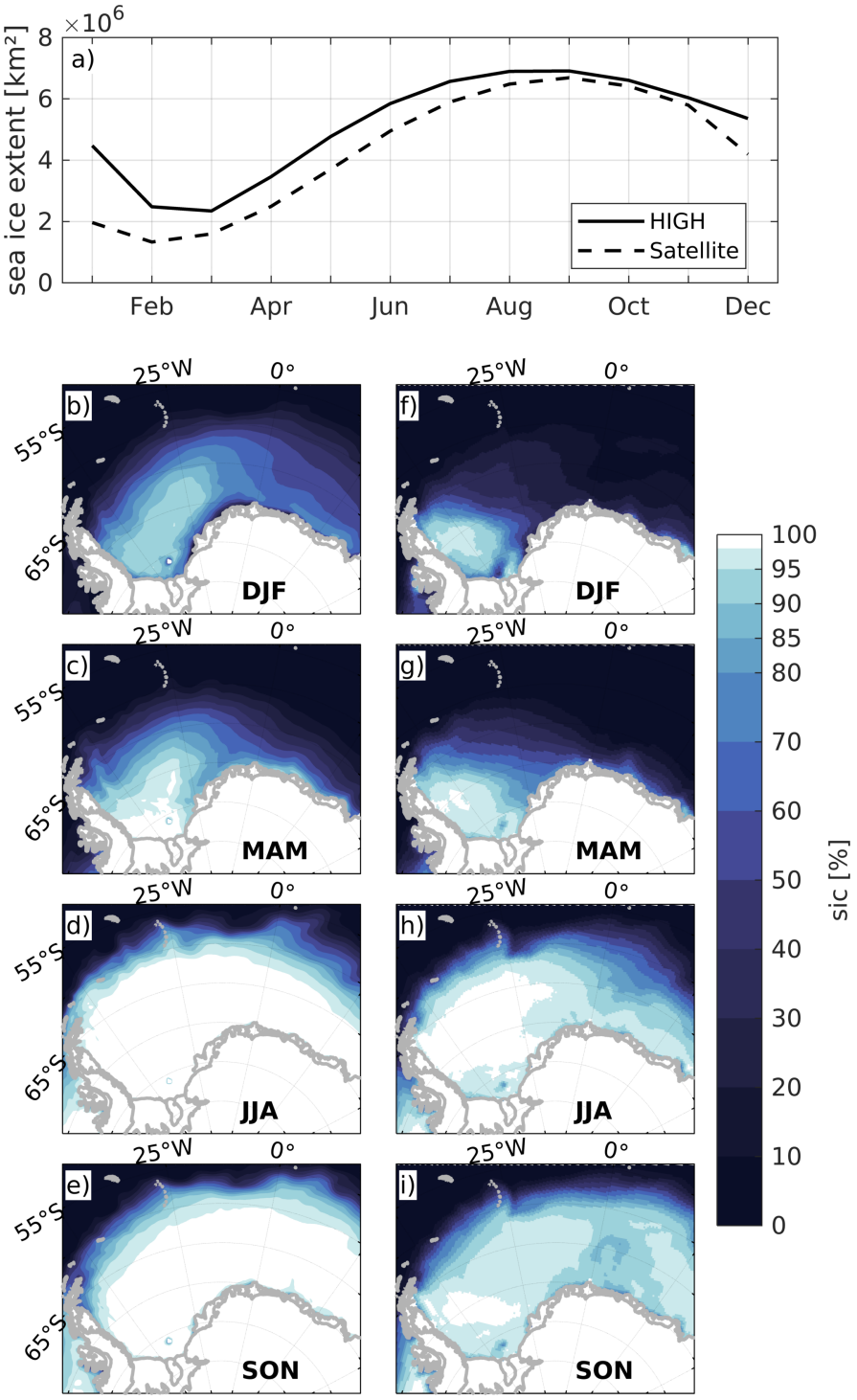

Figure 4.1: Climatological mean (1989-2010) seasonal sea ice extent (a) between 20°E−60°W (for sic> 15%) and concentration in the Weddell Sea for run HIGH (b-e) and observations (f-i). Observed concentration and extent from the NOAA/NSIDC Climate Data Record of Passive Microwave Sea Ice Concentration (*Zwally et al.*, 2002; *Parkinson and Cavalieri*, 2012). Sea ice extent includes areas with a concentration above 15%. Be aware of non-linear colorbar.

in the Weddell Sea (*Foldvik et al.*, 1985a). Furthermore, basal melt rates play a major role in the mass loss from the Antarctic ice sheet, by accounting for roughly 20% (*Rignot et al.*, 2013). It is, therefore, important to have an adequate representation basal melt in an ocean model. This section is meant to give a short overview of basal melt rates on a circumpolar scale and underneath FRIS.

Mesh HIGH comprises a total area of $1,516,568\,\mathrm{km}^2$ of ice shelves around Antarctica, with a total mean basal melt of $1596\,\mathrm{Gt\,a}^{-1}$ for the years 2000 to 2010, which corresponds to the upper end of the range, suggested by *Rignot et al.* (2013) ($1325 \pm 235\,\mathrm{Gt\,a}^{-1}$ for an area of $1,553,978\,\mathrm{km}^2$). The numbers agree with results from *Timmermann et al.* (2012), who obtained a circumpolar basal melting of about $1600\,\mathrm{Gt\,a}^{-1}$ for a total ice shelf area of $1,510,000\,\mathrm{km}^2$.

FRIS covers an area of $432114\,\mathrm{km}^2$ in HIGH and mean basal melt rates are shown in Figure 4.2. The melt rates depict a strong seasonal cycle with a maximum in February and a minimum in October. Annual mean melt rates (2000-2010) are $196\,\mathrm{Gt\,a}^{-1}$, with monthly means of $149\,\mathrm{Gt\,a}^{-1}$ and $322\,\mathrm{Gt\,a}^{-1}$ being found for October and February, respectively. While the summer value, and as a result also the total annual mean value, exceed all estimates for FRIS, the winter melt rate agrees with the results of *Rignot et al.* (2011) ($155\,\mathrm{Gt\,a}^{-1}$). The general spatial pattern of melting agrees with results from *Makinson et al.* (2011), with increased melting at the grounding lines and at the ice front, while refreezing is observed in the centre of the Ronne Ice Shelf.

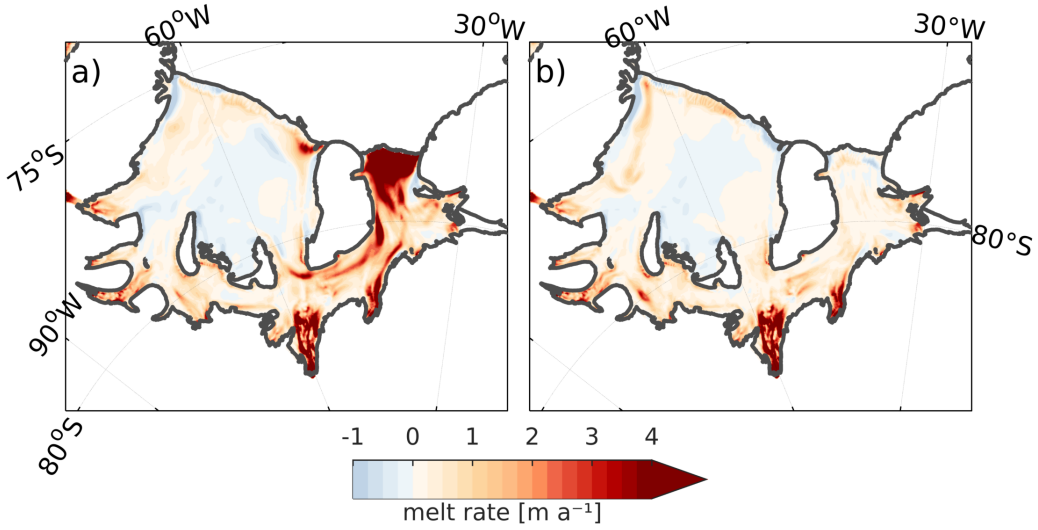

Figure 4.2: Modelled multi-year monthly mean (2000-2010) basal melt rates below the Filchner Ronne Ice Shelf in February a) and October b) for run HIGH.

Large discrepancies are found at the Filchner Ice Shelf front, possibly causing the overestimation of summer melt rates. Here, observations by (*Joughin*, 2003) and (*Rignot et al.*, 2013) show strong refreezing along the western side of the Filchner Trough, associated with the ISW northward flow of ISW, while the model shows strong melting in summer across the whole front. Later results will show that surface water can enter the ice shelf cavity at the ice shelf front in summer, which is likely related to the smoothing of the ice shelf front in FESOM (not shown), which is also suggested by *Naughten et al.* (2018). Furthermore, the used simulations produce a spurious southward flow of MWDW along the western flank of the Filchner Trough in summer, that enters the cavity. In winter, the modelled melt rates are more realistic. This pattern of strong melting at the Filchner front resembles the results of *Timmermann and Goeller* (2017) for an applied A1B scenario, but may be unrealistic under present day conditions.
I conclude, that despite some shortcommings, the model is able to reproduce plausible basal melt rates on circumpolar and the general pattern of melting below FRIS, however, it likely overestimates summer melt rates at the FIS front.

4.3 Modelled Weddell Gyre: structure and hydrography

In the following, I will assess the large-scale Weddell Gyre circulation with focus on its structure and strength in run LOW and HIGH. It will, by no means, be a complete analysis of the gyre dynamics and can, therefore, contain speculative comments or have purely informative character in some parts. However, I believe that it is necessary to address the question as to how well the Weddell Gyre is represented in the model, because it will affect the water masses reaching the southern continental shelf.

First, the structure of the gyre is analysed by looking at modelled sea surface height (SSH) in both simulations. Thereafter, the full-depth structure and hydrography along two representative sections (Prime Meridian & SR04 (WOCE)) will be investigated, with the aim to assess differenced between LOW and HIGH and their implication on the WDW transport to the southern Weddell Sea.

4.3.1 SSH fields

The purpose of this section is to assess the lateral structure of the modelled Weddell Gyre. This is important because the Weddell Gyre decouples the Weddell Sea from the direct influence of the ACC and, therefore, the global ocean circulation. The properties of the water masses ultimately reaching the southern Weddell Sea continental shelf, likely depend on the gyre's structure and its interaction with the ACC.

The negative wind stress curl over the gyre and the resulting surface flow divergence, induce upwelling in the centre of the gyre and downwelling along the coast. As a result the sea surface height (SSH) shows a minimum in the centre of the gyre. Generally, the SSH field describes the geostrophic flow of the upper ocean layer, however, a weakly stratified (compared to lower latitudes) water column within the Weddell Gyre suggest a strong barotropic gyre component. Furthermore, SSH has been compared to vertically integrated transports, along the prime meridian and reflects the general structure, i.e. the center and boundaries, of the gyre throughout the model simulation (see Figure A.1).

Figure 4.3 shows annual mean modelled SSH fields from the first (1979) and the last (2010) year of the model simulation, as well as the differences of both fields (2010 minus 1979) for HIGH (Figure 4.3a,c,e) and LOW (Figure 4.3b,d,f). Both simulations show a realistic gyre structure in 1979, which is the imprint from the initialisation data. The fields show an elongated axis of the gyre, which, following the Southwest Indian Ridge (see white contours), spans from the southwest to the northeast, indicated by the trough in SSH (see -1.9 m isoline). This trough depicts two cores at either side; one stronger core (SSH< -1.9 m) in the northwastern corner of the gyre (at $\approx 0°$) and one weaker core toward the Antarctic peninsula. The latter is not distinct in LOW (Figure 4.3b), however, the -1.9 isoline indicates the the two-core structure. Generally, LOW produces a weaker gyre and a smoother SSH field.

The gyre's eastern boundary is located at roughly 30°E, where the SSH-contours divert to the south. The closed contours in Figure 4.3a,b show two pathways from the eastern boundary to the southern Weddell Sea; one direct path, indicated by the -1.85 m contour and one elongated, that extends further to the east, which is indicated by the -1.8 m contour in HIGH and -1.75 m contour in LOW.

The initial modelled structure, including the two cores, agrees with observa-

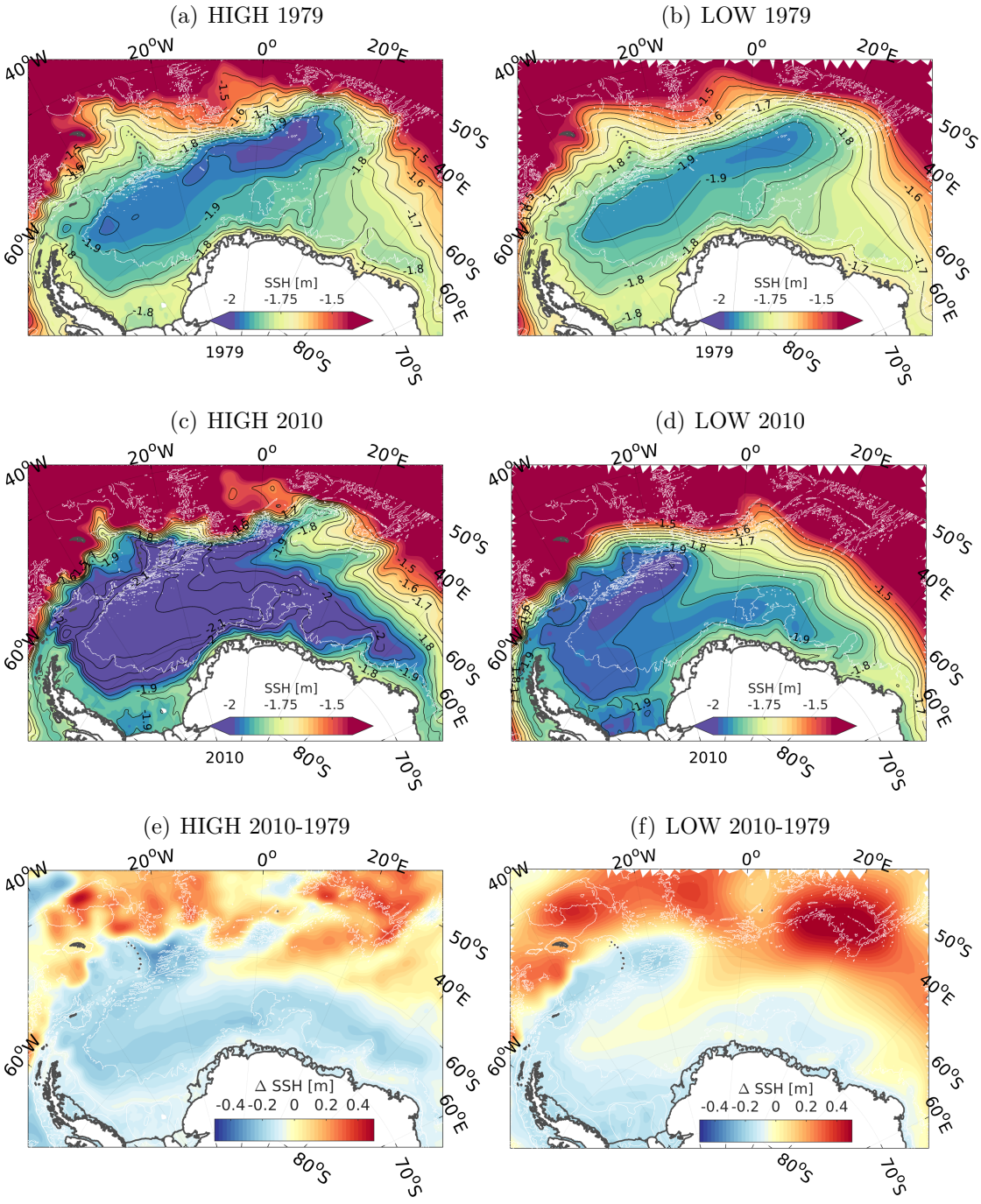

Figure 4.3: Modelled annual mean sea surface height (SSH) over the Weddell Gyre in 1979 (top) and 2010 (middle) and the difference year 2010 minus year 1979 (bottom) in run HIGH (left) and LOW (right).

tions (dynamics topography, *Orsi et al.* (1993)) and model results (barotropic streamfunction, *Beckmann et al.* (1999)), which indicates that the SSH field is a reasonable proxy for the structure of the Weddell Gyre. The two described pathways at the eastern boundary are consistent with results from *Gouretski and Danilov* (1993), *Schröder and Fahrbach* (1999) and *Ryan et al.* (2016), who suggest a shorter, eddy-driven and a longer, advective (mean-flow) pathway, along which CDW is transported into the gyre and ultimately. The structure and variability of these pathways will, ultimately, determine the properties of WDW in the Weddell Gyre.

Figure 4.3c shows the mean SSH field in the last year (2010) of HIGH and Figure 4.3e shows the difference of both years. The SSH field suggests, that the gyre has undergone strong structural changes. While, generally, lower SSH values (< -2 m) are found, most pronounced differences are found in the northwestern corner, where the stronger core was present in 1979. The two-core structure and the associated trough are not maintained. Instead a stronger cell has formed, extending further east along the coast to almost 60°E.

Run LOW (Figure 4.3d,f) depicts similar changes than HIGH, with the vanishing of the northeastern core and an eastward extension of the gyre along the coast. The center of the gyre (SSH< -1.95 m) has moved to the northwestern corner. The observed changes in LOW and HIGH are also reflected in the modelled temperature field at 350 m depth (Figure A.2).

In order to investigate the hydrographic structure of the gyre, two representative sections have been chosen. The first section is placed along the prime meridian, a former WOCE section (SR6). It should capture the possible changes of hydrography and circulation in the eastern part of the gyre, suggested by the SSH fields. The second section, spanning from Kapp Norvegia to the tip of the Antarctic Peninsula (former WOCE section SR04), will give further insight into the hydrography within the Weddell Sea and the properties upstream of FRIS.

4.3.2 Transport and hydrography along the Prime Meridian

In this section, I will investigate the modelled circulation and hydrography at the prime meridian, which captures the southern branch of the Weddell Gyre, that carries the inflowing water masses.

Barotropic transport

Figure 4.4 shows the cumulative, vertically integrated eastward transport along the prime meridian from all model years for HIGH (Figure 4.4a) and LOW (Figure 4.4b). At the beginning of the simulation (1979), both LOW and HIGH depict a westward boundary current at the continental slope with a transport af about 20 Sv. To the north oft, up to about 66°S, a weak flow is found, which can be associated with the presence of Maud Rise (see bathymetry shown in grey in Figure 4.4d-g). Between 64°S and 60°S, the cumulative transport decreases (increasing westward transport) further by about 18 Sv in LOW and 30 Sv in HIGH. Thereafter, a strong increase depicts the northward, eastward flowing branch of the Weddell Gyre, which is located over the southern flank of the Southwest Indian Ridge. The zero-crossing of the cumulative transport marks the northern boundary of the gyre, hence the further increase of the transport to the north describes the eastward transport within the ACC. These transports produced by the initialisation field suggest that the flow along the prime meridian is strongly influence by the topography.

The structural changes of the Weddell Gyre throughout the simulation, as suggest by the SSH fields (Figure 4.3), are also found in the cumulative transports. The above described initial structure changes gradually until 2000, while it is more or less constant from then onward. LOW shows a decrease in the boundary current transport from about 20 Sv to 15 Sv and the interior westward transport vanishes (no further increase in cumulative transport). This goes along with a southward shift of the gyre's northern boundary (zero-crossing) of about 5° latitude (> 500 km), which is in agreement with the changes observed in the modelled SSH field (see position of -1.75 m contour in Figure 4.3).

Although the general gyre structure, i.e. the northern boundary, is maintained in HIGH, the interior circulation also undergoes changes throughout the spin-up period (1979-2000). Two main features are: First, the boundary current transport almost doubles its transport (from roughly 20 Sv to 38 Sv) and becomes broader. Second, the interior westward transport, as in LOW, decreases to almost zero.

The maximum cumulative transport along the section, serves as an estimate of the gyre strength at this location and is shown as a time series of monthly values for HIGH and LOW in Figure 4.5. Both simulations show a decreasing gyre strength throughout the first 15 years, where the mean strength in HIGH decreases from about 50 Sv to 30 Sv and LOW from 40 Sv to 20 Sv. Thereafter, the

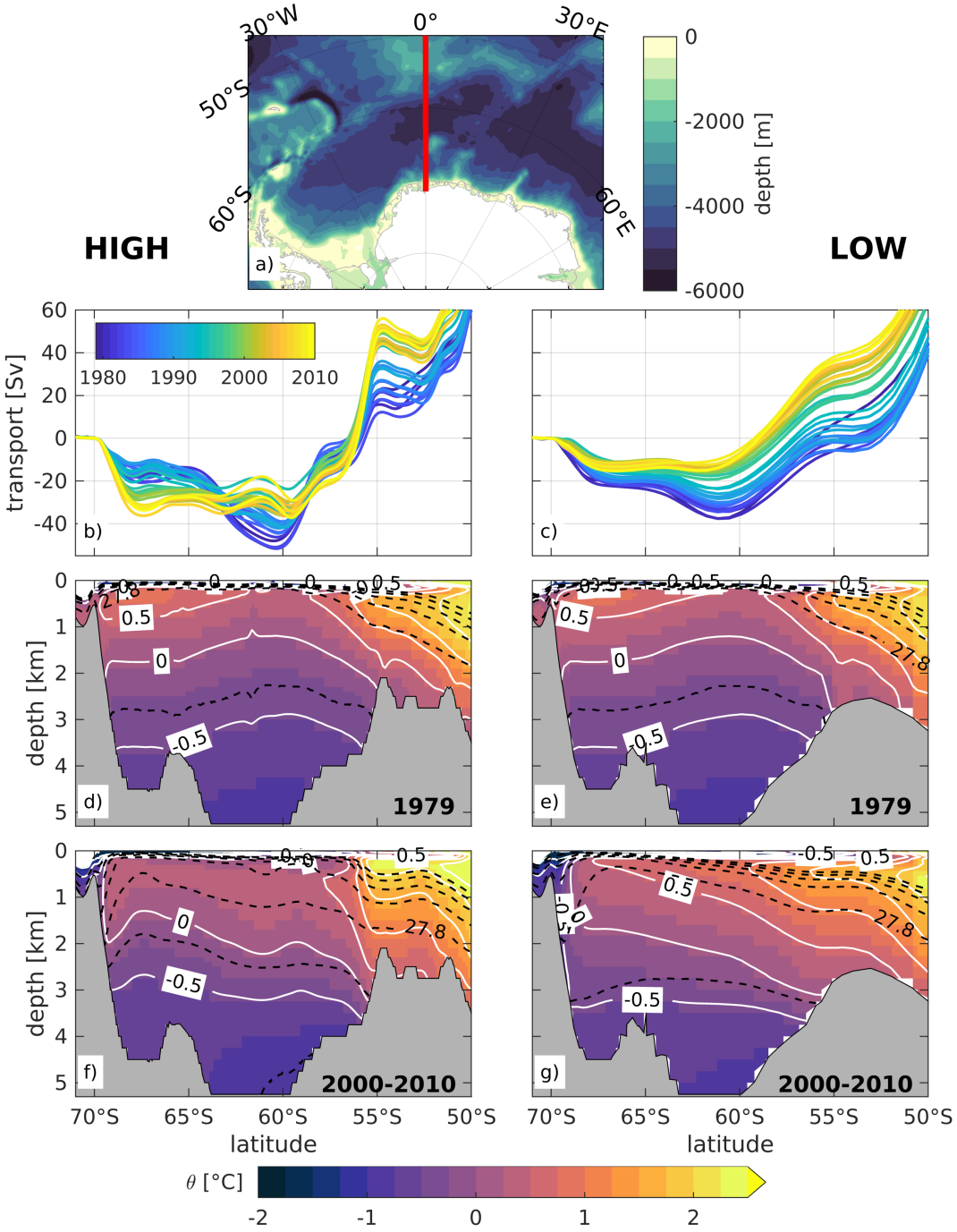

Figure 4.4: a) Bathymetry of the Weddell-Enderby basin with the prime meridian marked in red. Annual mean, cumulative vertically integrated transport over the section for b) HIGH and c) LOW; Initialisation potential temperature field interpolated on the model grid for d) HIGH and e) LOW; Mean potential temperature (2000-2010) for f) HIGH and g) LOW. For d)-g), white isolines denote potential temperature in 0.5°C steps and black, dashed lines potential density in $0.05\,\mathrm{kgm}^{-3}$ intervals.

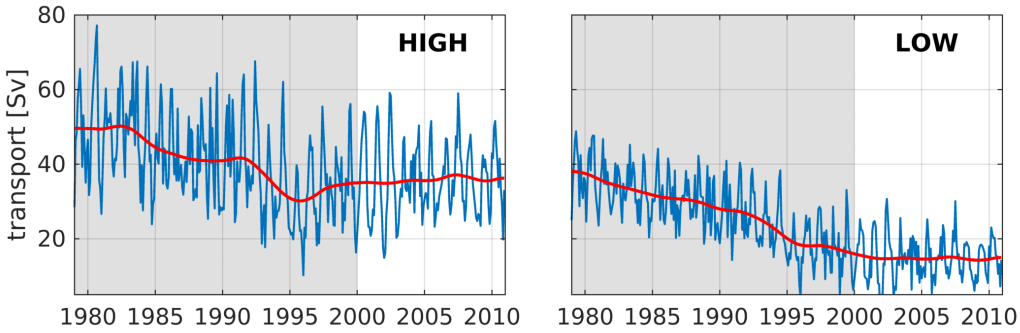

Figure 4.5: Time series of monthly mean values of the maximum cumulative westward transport (see Figure 4.4a,b) at the prime meridian for HIGH (left) and LOW (right). The red line represents the low-pass filtered time series with a cut-off period of 5 years. The grey shading marks the considered time period for the spin-up of the model.

transport in HIGH increases again slightly to about 38 Sv and remains constant around this value from 2000 onward. In LOW the transport further decreases after 1995 by 5 Sv and stays around 15 Sv. The mean seasonal variability in transport in HIGH comprises a range of about 30 Sv compared to about 20 Sv in LOW.

The full depth transport across the prime meridian has been estimated, based on observations, 56 Sv by *Klatt et al.* (2005) and 61 Sv by *Schröder and Fahrbach* (1999). These estimated lie at the upper range of the transport in HIGH, while LOW clearly lies below.

Hydrography

Figure 4.4 shows potential temperature along the prime meridian from the initialisation field (1979) for HIGH (d) and LOW (e). As mentioned earlier, the Weddell Gyre is characterised by doming isopycnals, due to the negative wind stress curl over the region. This feature is well represented in the initialisation field. Furthermore, a warm temperature core ($\theta > 0.5$°C) south of 60 °S represents the southern branch of the Weddell Gyre, where CDW (later WDW) is injected into the gyre (*Schröder and Fahrbach*, 1999; *Ryan et al.*, 2016). Lower temperatures to the north, associated with eastward flow, resemble the 'cold regime', which describes the, in the gyre recirculated, WDW (*Schröder and Fahrbach*, 1999).

Above the Southwest Indian Ridge, an oceanic front, called Southern Boundary (*Orsi et al.*, 1995), marks the transition from polar to subpolar water, marked by the southward extent of the CDW ($\theta > 1.5$°C). This front coincides with the peak

of the mid-ocean ridge.

Figure 4.4f,g show the potential temperature field from 2000-2010 for HIGH and LOW. The temporal changes of the gyre structure, seen in SSH and transport, are also manifested in the hydrography.The characteristic doming structure of the isopycnals does not exist any more after the spin-up time and both runs show shoaling isopynals (see $27.8\,\mathrm{kg\,m^{-3}}$ isopycnal) up to roughly 67°S across the mid-ocean ridge. This is coherent with this observed decreased of westward transport (Figure 4.4b,c).

In HIGH a strong front over the Southwest Indian Ridge persists, indicated by the 0.5°C isotherm, which forms a northern boundary of the gyre. In LOW warm water with temperatures above 0.5°C continuously upwells toward the south. These differences are likely caused by the differences in model resolution, which affects the ocean processes (no mesoscale activity resolved in LOW) but also bathymetry, which is much smoother in LOW. It was shown in several studies that the fronts in the Southern Ocean, hence also the northern boundary of the Weddell Gyre, are strongly steered by topography (*Gille*, 1994; *Orsi et al.*, 1995).

These results show suggest that the eastern part of the Weddell Gyre is a complex region that needs to be improved in the model in the future, as the structure will affect the hydrography in the gyre significantly. To which degree these changes affect the WDW properties further downstream, will be investigated at a later point after taking a closer look at the structure and hydrography in the western part of the gyre.

4.3.3 Transport and hydrography across the Weddell Sea basin

It was shown that the eastern part of the Weddell Gyre undergoes substantial changes in the model, in both, LOW and HIGH. In this section, I will investigate the evolution in the western part of the gyre. SSH fields (Figure 4.3) suggested that a strong gyre persists in the Weddell Sea. For the analysis section SR04 (WOCE) is chosen, which crosses the Weddell Sea basin from Kapp Norvegia to the tip of the Antarctic peninsula.

Barotropic transport

The cumulative vertically integrated transport across SR04 is shown in Figure 4.6b,c. In both simulations, the overall structure of the gyre does not change, meaning that boundary currents are found on either side of the basin and the cumulative transport maximum is located at about 43°W. However, a strong adjustment is also found during the spin-up time. In HIGH, the boundary current has, similar to the prime meridian, strengthened significantly by the end of the spin-up time (from about 15 Sv to 25 Sv), although almost non-existent in between (around 1990). In contrast, the boundary current weakened continuously in LOW, as found already at the prime meridian.

The maximum of the cumulative transport is shown as time series in Figure 4.7 for HIGH and LOW. Similar to the prime meridian, the gyre strength decreases throughout the spin-up period until 1995 in both simulations, with a small exception in HIGH where a short increase is found around 1983. The transport decreases by about 10 Sv from 30 Sv to 20 Sv in HIGH and LOW. In contrast to the prime meridian (Figure 4.5), where the mean gyre strength in HIGH remained more or less constant at 38 Sv after the spin-up period, the decrease at SR04 is followed by a steady increase to a mean transport of about 38 Sv at the end of the simulation (2010). Although the gyre strength at the prime meridian was roughly 20 Sv higher than at SR04 in 1979, both sections exhibit almost the same strength in 2010, which is likely attributed to the observed adjustments in the gyre. In LOW, only a slight increase of transport (≈ 2 Sv) is found from 2000 onward. Here, the transport is about 5 Sv higher at SR04 compared to the prime meridian, but is generally small.

Hydrography

The hydrography at SR04 in the initial field (Figure 4.6d,f) is characterised by WDW layer ($\theta > 0°$) spanning across the whole Weddell basin. On either side a core with temperatures above 0.5°C is found. On the eastern side, WDW is transported southward and recirculates to the north along the western side and cools on its way due to mixing with shelf waters, which is why the warm core is smaller in the west.

After the spin-up period this warm core is not present any more in HIGH, which agrees with the upstream hydrography at the prime meridian (Figure 4.4d). The WDW layer, indicated by the 0°C isotherm, shows only very little changes in

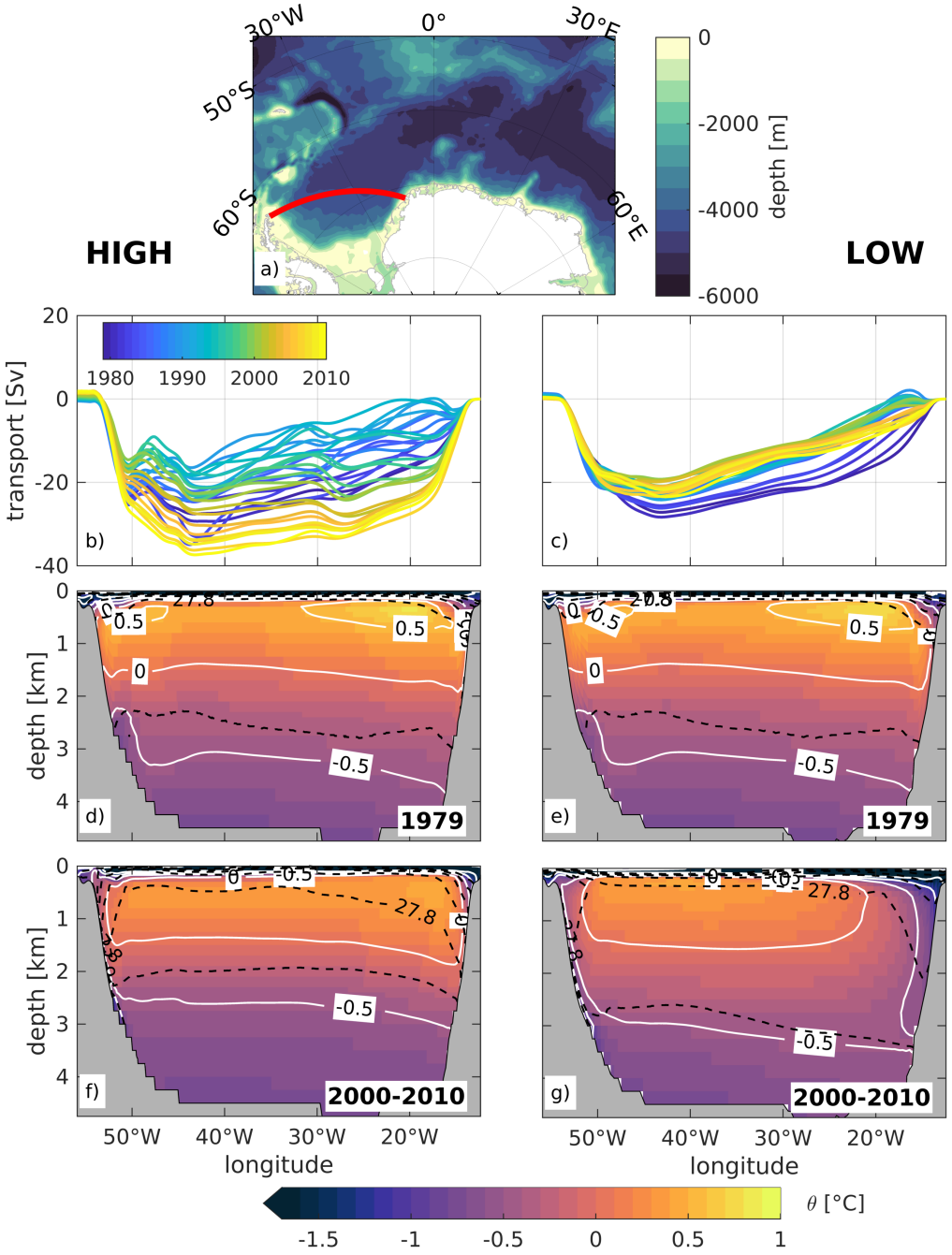

Figure 4.6: a) Bathymetry of the Weddell-Enderby basin with section SR04 marked in red. Annual mean, cumulative vertically integrated transport normal to section SR04 for b) HIGH and c) LOW ; Initialisation potential temperature field interpolated on the model grid for d) HIGH and e) LOW ; Mean potential temperature (2000-2010) for f) HIGH and g) LOW . For d)-g), white isolines denote potential temperature in 0.5°C steps and black, dashed lines potential density in 0.05 kgm^{-3} intervals.

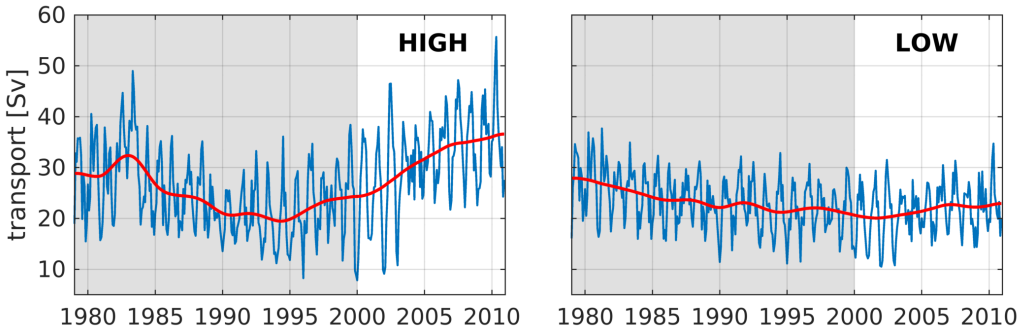

Figure 4.7: Time series of monthly mean values of the maximum cumulative westward transport (see Figure 4.6a,b) at the prime meridian for HIGH (left) and LOW (right). The red line represents the low-pass filtered time series with a cut-off period of 5 years. The grey shading marks the considered time period for the spin-up of the model.

temperature, however, the upper part of the layer has freshened, particularly on the eastern side, which can be seen by the position of the $27.8\,kg\,m^{-3}$ isopycnal. This freshening, was also present at the prime meridian, which suggests that the changes along the eastern boundary have led to property changes of the WDW being transported along the continental slope.

In LOW, the WDW layer over the eastern continental slope (east of 20°E) has been eroded and a very weak ASF is found, which again can be traced back to the changes found at the prime meridian. *Ryan et al.* (2016) have indicated that the eastern boundary is crucial for setting the properties of WDW entering the gyre. Interestingly, the 0°C layer in HIGH undergoes similar changes during the spin-up period, but re-establishes toward the end of the 1990s and persists throughout the last 10 years of the simulation. The warmest core ($\theta > 0.5$°C), however, does not reappear.

4.3.4 Seasonality of the ASC and Drivers

In the following, I will the investigate the seasonality of the modelled ASF current across SR04 and compare it to the mean seasonality of possible forcing mechanisms. For this analysis only results from HIGH will be used as no realistic ASF is produced in LOW. Generally, the current acts as a dynamical barrier along the continental shelf, hence, its seasonality can influence the on-shelf flow of MWDW but also the water mass formation on the shelf.

The boundary part (representing the ASC) has been derived as the maximum

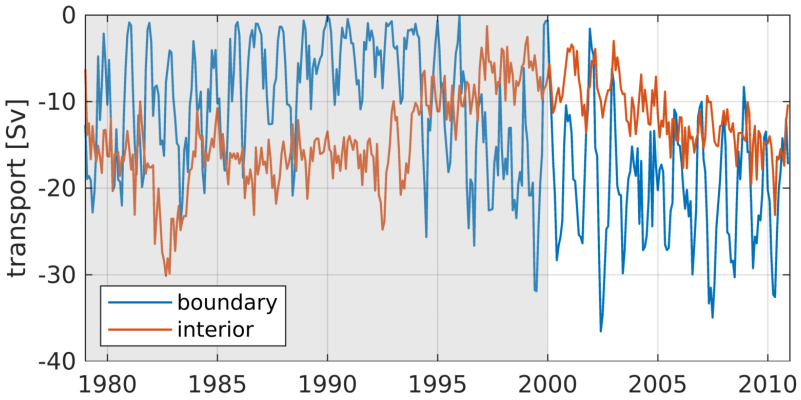

Figure 4.8: Time series of interior and boundary contributions to the maximum cumulative transport normal to section SR04, with the separation at 17.5°W (see black dashed line in Figure 4.9a). The grey shading marks the considered spin-up time period of the model.

of the cumulative southward transport from Kapp Norvegia to 17.5°W (see Figure 4.9a, black dashed line). This boundary flow has been subtracted from the maximum of the cumulative southward transport across the whole section (i.e. the gyre strength presented in Figure 4.7), to obtain the interior southward transport. Figure 4.8 shows the transport time series of both components. Again, the strong adjustment of the gyre is visible during the spin-up period (1979-2000). Between 2000 and 2010, the ASC transport is in the mean almost double as large as the interior (-19.9 Sv vs. -11.5 Sv). Both components show a mean increase, which is in agreement with the increase in the total gyre strength shown in Figure 4.7. Generally, the ASC transport shows a larger variability with a standard deviation of 7.2 Sv compared to 3.8 Sv in the interior over the 10-year period (2000-2010).

Figure 4.9a shows temperature along the eastern part of section SR04. Additionally, the velocity normal to the section is shown as white, dashed contours and potential density as grey contours. The mean seasonal velocity in the upper right red rectangle will represent the strength of the slope current and is shown in Figure 4.9b. The mean ocean surface stress (model output) curl over the Weddell Gyre (60°W-40°E,55 – 75°S) is shown in Figure 4.9c. It was previously suggested, that the local zonal wind component, and the associated on-shore Ekman transport may explain a larger amount of the ASC variability together with the buoyancy forcing. *Núñez-Riboni and Fahrbach* (2009). The zonal wind component (model forcing) has been averaged between $5-15$°W and $70-72$°W and is shown in Figure 4.9d. As a measure of the buoyancy forcing, the multi-year (2000-2010)

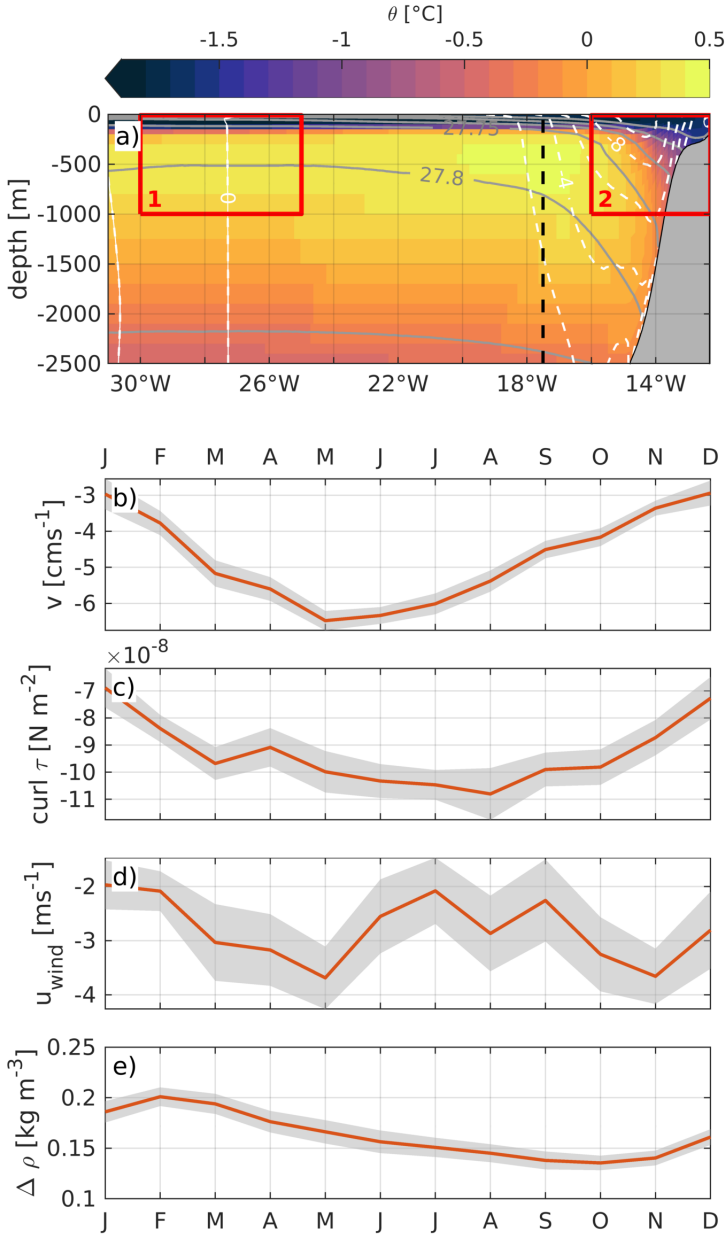

Figure 4.9: a) Modelled mean (2000-2010) temperature of the upper 2500 m along the eastern part of section SR04. White, dashed contours denote negative (southward) velocities, normal to the section in 2 cm s^{-1} intervals and grey contours represent potential density referenced to surface pressure in 0.05 kg m^{-3} intervals. The black dashed line marks the boundary chosen to separate boundary (east of 17.5°W) and interior (west of 17.5°W) southward flow as shown in Figure 4.8. Mean seasonal cycle (2000-2010) of b) the normal velocity, averaged over the boundary current (east of 17.5°W), c) the large scale curl of the model surface stress (40°E - 60°W, 55 – 75°S), d) the local zonal wind component (5 – 15°W, 70 – 72°S) and d) averaged density difference between box 1 and box 2 (see panel a). The grey shading in b)-e) represents the estimated standard error of the mean (see Eqn.4.1).

monthly mean density difference between the interior ($25-30°$W) and the coastal region ($12.5-16°$W) in the upper 1000 m (see Figure 4.9a, red rectangles) is calculated and shown in Figure 4.9e. For each component the standard error of the mean σ_m is estimated for each monthly average from the standard deviation σ

$$\sigma_m = \frac{\sigma}{\sqrt{N-1}} \tag{4.1}$$

where N represents the total number of data points and $N-1$ represents the "effective number of degrees of freedom".

The ASC shows a maximum strength in May ($\approx 6.2\,\mathrm{cm\,s^{-1}}$) and a minimum in December ($\approx 3\,\mathrm{cm\,s^{-1}}$), which is in agreement with the results of *Núñez-Riboni and Fahrbach* (2009), who observe maximum barotropic velocities between $-6\,\mathrm{cm\,s^{-1}}$ and $-9\,\mathrm{cm\,s^{-1}}$ at two moorings at the prime meridian. Also the timing agrees with their observations. The modelled surface stress depicts a maximum in August ($\approx 11 \cdot 10^{-8}\,\mathrm{N\,m^{-2}}$), while the local zonal wind reaches its maximum in May and a second maximum in November. The standard error for both components is rather small. Although slightly larger for the zonal wind, the seasonal cycle seems to be significant. The maximum of the local wind in May, compared to a maximum in August of the large scale surface stress curl, supports the hypothesis of *Núñez-Riboni and Fahrbach* (2009), that the local zonal wind plays a lager role for the slope current variability. Interestingly, the mean seasonal cycle of the interior transport (not shown), shows a maximum in August, suggesting that the interior transport variability is controlled by the large-scale winds.

The buoyancy forcing (Figure 4.9e) is strongest in February with a horizontal density gradient of about $0.2\,\mathrm{kg\,m^{-3}}$, while a minimum gradient of $0.13\,\mathrm{kg\,m^{-3}}$ is found in October. This agrees with the seasonal cycle of sea ice, which has a minimum in February, leading to increased fresh water at the surface that is downwelling over the continental shelf, hence introducing a larger density gradient. In winter, the surface layer becomes denser due to brine release during sea ice formation, thus explaining a weaker gradient.

Generally, HIGH reproduces a seasonality within the coastal current that agrees with the seasonal evolution presented by *Núñez-Riboni and Fahrbach* (2009), which is an important step toward modelling the correct ASF properties.

4.4 Shelf break hydrography and implications for the MWDW inflow

In the previous section it was shown that the model is able to reproduce the key features of the seasonality of the ASC. For the cross-shelf exchange at the southern Weddell Sea continental shelf it is, furthermore, important that the water mass properties associated with the ASF are represented correctly. This will be analysed in this section on the basis of a hydrographic section cross-cutting the shelf break, just east off the Filchner Trough at 31°W.

Modelled mean (2000-2010) potential temperature along this section (Hereafter referred to as section 31W) is shown in Figure 4.10 a) and c) for LOW and HIGH, respectively. It can be seen from the isotherms (white lines) and isopycnals (black, dashed lines) that also here the ASF is less pronounced in LOW compared to HIGH. While in HIGH temperature above the shelf break ranges from $-1.5^{c}irc$C to over 0°, there are no temperatures warmer than 0.5°C found in LOW. Furthermore, density ranges from 27.7 kg m^{-3} to 27.7 kg m^{-3} between roughly 500 m and 2000 m in LOW, while the density gradient is below 0.05 kg m^{-3} in LOW.

Observations show a strong density gradient exceeding 0.2 kg m^{-3} between roughly 500 m and 1000 m depth with a maximum-temperature core ($\theta > 0.5\,°$C) at the lower edge, reaching very close to the shelf break (see Figure 3.4). Hence, HIGH is performing reasonably well regarding by maintaining stronger temperature and density gradients at the shelf break, which suggests that high resolution is important.

Furthermore, observations show a thick fresh and cold layer, representing WW, of several hundred meters thickness, that govern the upper ocean ($\approx$ 500 m), suppressing the WDW core below the shelf break depth (see Figure 3.4). This layer is not present in either run, LOW or HIGH. Instead, the WDW layer, indicated by the −1.5°C isotherm (see white isolines in Figure 4.10a,c), extends higher up in the water column to about 100 m depth, which allows a permanent warm flow onto the continental shelf over a thick layer ($\approx$ 400 m).

θ-S properties along section 31W are shown in yellow in Figure 4.10b (LOW) and d (HIGH), including observational data from the area obtained during PS82 and PS96 (gray). The temperature range is covered fairly well by HIGH, however, the whole distribution is on average shifted about 0.1 toward lower salinities, re-

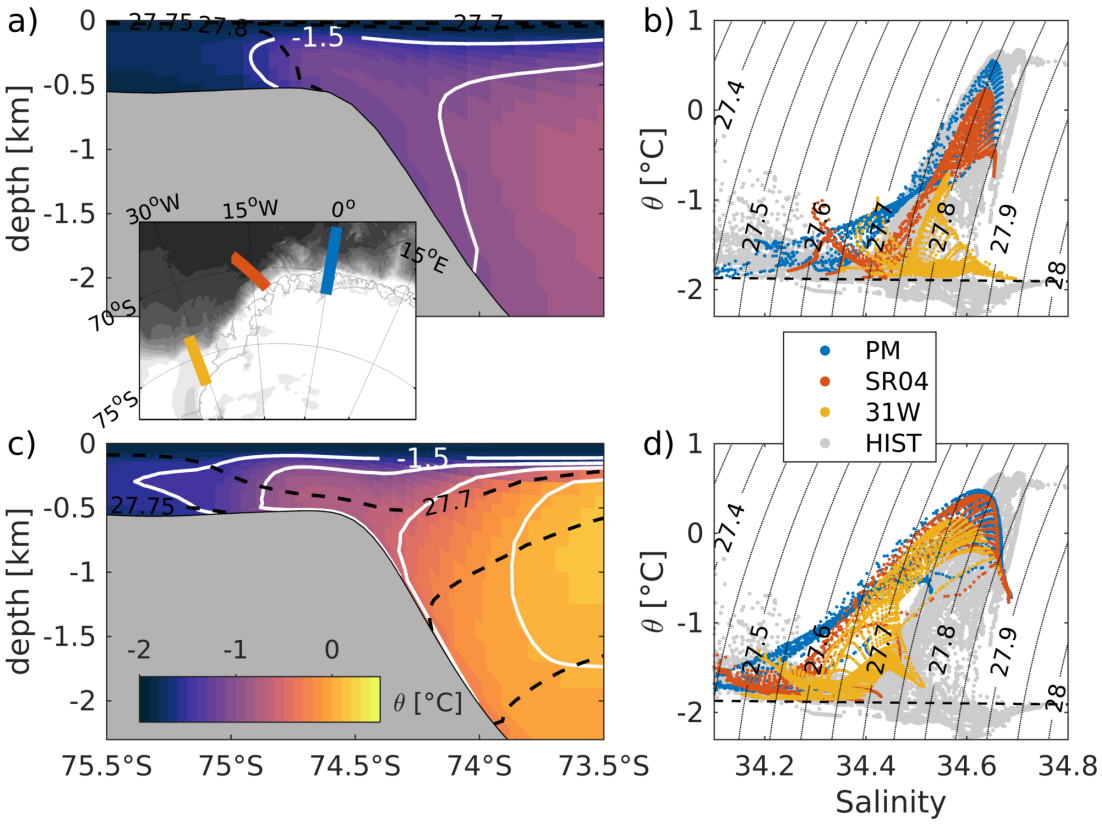

Figure 4.10: Multi-year mean (2000-2010) hydrographic section along the 31°W meridian (section 31W) for LOW (a) and HIGH (c). Isotherms are shown as white contours with 0.5 °C intervals and black, dashed lines denote potential density in 0.05 kg m^{-3} intervals. θS diagrams showing data above the continental slope from LOW (c) and HIGH (d) at three sections: prime meridian (blue) data south of 67°S, Kapp-Orkney (orange) data south of 69°S and 31W (yellow) data south of 73.5°S.

sulting in lower densities ($\approx 0.05\,\mathrm{kg\,m^{-3}}$). A comparison to model results over the continental slope at the prime meridian (blue) and section SR04 (orange) suggests that this freshening in HIGH is determined already at the eastern boundary of the gyre, where the WDW inflow occurs. Little modification takes place during southward propagation. The WDW properties at the prime meridian in LOW match the observations better, which could be due to the direct upwelling of ACC waters at this location after the spin-up time. However, it could also be seen that the WDW does not extend over the continental slope in LOW, which in cohesion with a weak boundary current, results in the properties found at section 31W.

Although the MWDW found on the continental shelf in LOW actually has

similar properties to the observed MWDW, the absence of a slope front and a warmer core at the shelf break do not allow a realistic analysis of the seasonal inflow. Likewise, are the shelf break properties in HIGH not adequate for a regional analysis of the cross-shelf exchange, as the fresh and shallow MWDW layer leads to a permanent warm inflow.

4.5 Conclusions

Increased model resolution over the whole Weddell Gyre leads to a significant improvement regarding the gyre structure, transport and hydrography. SSH fields and vertically integrated transports reveal a strong adjustment of the gyre over the first 20 model years in LOW and HIGH. Both show most pronounced changes in the northeastern part of the gyre, where WDW enters the gyre.

In run LOW, the eastern core of the gyre circulation breaks down entirely and only a weak ASC remains. A hydrographic section along the prime meridian shows a near continuous upwelling across the mid-ocean ridge, exhibiting very weak fronts and the characteristic gyre structure with doming isopycnals is non-existent. As a result less WDW is injected into the southern rim of the gyre, leading to a weaker slope front and an unrealistic WDW transport toward the southern Weddell Sea continental shelf in LOW.

Although the gyre also undergoes significant changes in simulation HIGH, many features have improved compared to LOW. First, the SSH field in HIGH shows the influence of the Southwest Indian Ridge in the circulation by constraining the flow along it and as a results stronger fronts are marking the northern boundary of the gyre. Second, the WDW inflow along the southern branch over the continental slope is captured better in HIGH, leading to a stronger ASC and a more realistic structure of the WDW layer within the gyre. In particular, the slope front persists along the continental slope all the way to the southern continental shelf, associated with a strong ASC.

Despite an improved ASF structure from LOW to HIGH, the modelled WDW properties in HIGH deviate toward lower salinity, i.e., lower density values, when comparing to observations or the model initial conditions. The results suggest that the properties are set at the gyre's eastern boundary. WDW properties at the prime meridian are represented better in LOW, however, due to the vanishing ASC in this simulation, this WDW is not transported toward the southern continental

shelf, thus leading to lower temperatures along the shelf break. The differences in water mass properties in LOW and HIGH, could be due to structural differences of the modelled Weddell Gyre's eastern boundary, such as the continuous upwelling in LOW, but also due to differences in model parameters, such as diffusivity, which are necessary due to the differences in resolution.

An analysis of the modelled shelf break properties just east of the Filchner Trough shows, that although HIGH produces improved ASF representation and is able to simulate a realistic seasonal cycle of the ASC, neither of the simulations allow a realistic analysis of the on-shelf flow of MWDW. I conclude, that high resolution is necessary in order to simulate realistic ASF properties and their seasonal variability, however, further model tuning is required to improve the Weddell Gyre circulation with focus on its eastern boundary and the derived WDW properties. Despite being an important analysis, this would deviate from the focus of this thesis, which is the MWDW flow onto the southern Weddell Sea continental shelf. An alternative approach is presented in the following section.

5. MWDW inflow along the Filchner Trough in a 3D-restoring model approach

As shown in the model assessment in the previous chapter, the high-resolution simulation leads to a significant improvement in terms of the general Weddell Gyre circulation and the ASF structure compared to the low-resolution simulation. However, the current representation of the ASF and the associated water masses does not allow for a detailed analysis of the warm water transport onto the southern continental shelf. A more extensive analysis and tuning of the model is required to improve the Weddell Gyre circulation with focus on its eastern boundary. Although being very essential, this would deviate from the focus of this thesis. In the following, an approach is presented that allows to keep the focus on the MWDW inflow toward FRIS by restoring the upstream region above the continental slope to a newly available climatology.

5.1 A regional restoring model set-up

Since the start of oceanographic research the vastness of the ocean has always been a challenge. Especially in remote areas, such as Antarctica, data acquisition is limited by hazardous conditions. This also causes limitations for data products such as the WOA13, which is used to initialize and also validate ocean models.

For the restoring approach, I use a hydrographic climatology, recently compiled by *Hattermann* (2018). It comprises available historical data from ship-borne CTD profiles and Satellite Relay Data Logger equipped seals (SRDL-CTD) between 1977 and 2016 near the continental shelf in the area $10° - 25°$W and $70° - 74°$S (2859 profiles). The data has been projected onto a mean section

at Kapp Norvegia, at 17°W, and merged to monthly mean fields of temperature and salinity on isobath levels, as the ASF and the associated current (ASC) are strongly controlled by the topography. For further details see *Hattermann* (2018).

The WOA13 mean field is used as a background field. My approach is to implement the section climatology along the continental slope between Kapp Norvegia and Brunt Ice Shelf ($10 - 22$°W, $70 - 76$°S, see white dashed line in Figure 5.1a) according to the local bottom depth. The steps are as follows:

- As the bathymetry is very coarse in the WOA13, the RTopo-2 data set (*Schaffer et al.*, 2016) was interpolated onto the WOA grid ($0.25° * 0.25°$).
- The section climatology has been projected onto the vertical levels available in the WOA13.
- For each point in the defined patch, the bottom depth was identified from the RTopo2 and the profile in the atlas data was replaced by the profile of the section climatology located at the closest isobath.
- Each profile has then been checked for stability and has been corrected, if necessary, via the convective adjustment approach (*Madec et al.*, 1991).
- The edges of the adjusted patch are then smoothed by an one-sided moving average, (e.g. $x_{i-1} = \overline{x_i + x_{i+1} + x_{i+2}}$), in order to maintain the ASF structure as good as possible.

The model set-up is the same as described in section 2.2.3 within the patch temperature and salinity are restored over the whole water column with a time scale of 3 hrs. This nudging method resembles the simplest way of data assimilation and is commonly used for constraining, e.g., sea surface temperature and salinity in ocean and climate models. My approach is to restore the 3-D temperature and salinity field over a region that, I believe, is crucial, in terms of a correct hydrographic representation, for the cross-shelf exchange further downstream. The restoring simulation will be referred to as RESTORING from here on. Again, the first 20 years are used as model-spin up.

In this thesis, I am restoring to summer (January) hydrography, as it comprises the most data points and at the point of analysis, only scattered fields were available for other seasons. At the same time, the summer restoring serves as a sensitivity study, as to how the inflow behaves when the ASF does not show the strong seasonal elevation change as described earlier in the observations, therefore, not suppressing the WDW in winter. Previous studies have suggested a shoaling of

the ASF around the Antarctic continent and an associated increased flow of warm water toward ice shelves (e.g. *Schmidtko et al.* (2014)). Hence, I will investigate the role of the continental shelf itself in the seasonal warm inflow toward FIS.

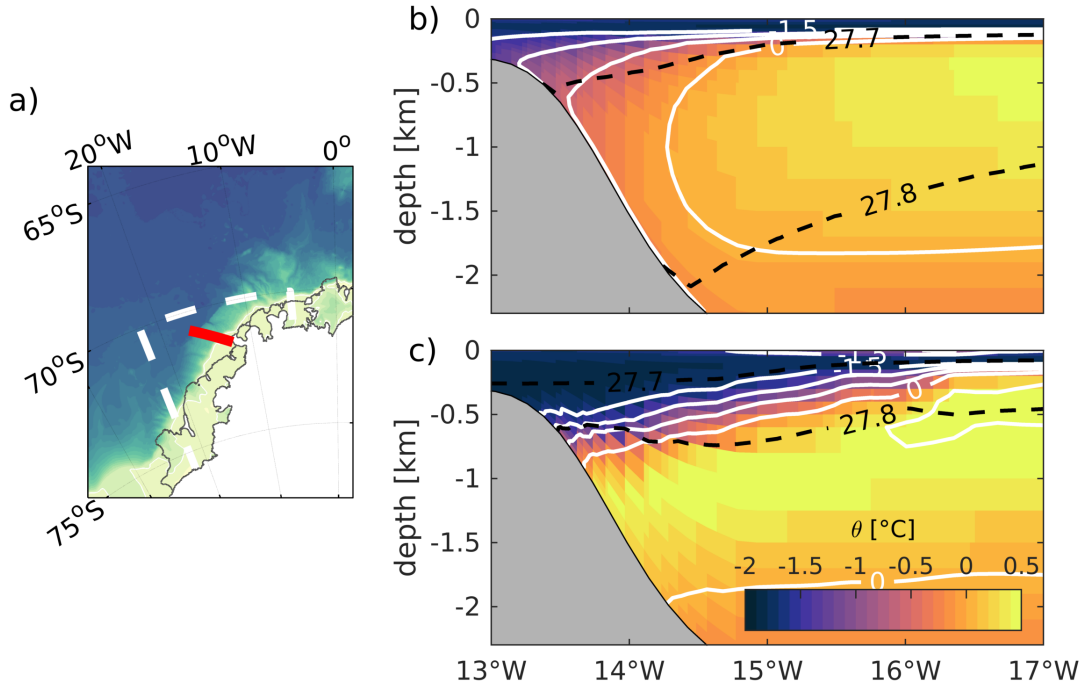

Figure 5.1: a) Bathymetric map showing the extent of the restoring area for run RESTORING. The red line marks the location of the 10-year mean modelled potential temperature θ for b) HIGH and c) RESTORING within the restoring area. Black, dashed lines represent potential density referenced to surface pressure in 0.1 kg m^{-3} intervals. White lines are isotherms in 0.5 °C intervals.

Figure 5.1 shows a 10-year mean (2000-2010) section of potential temperature at Kapp Norvegia (marked red in Figure 5.1), cross-cutting the continental slope, for HIGH (a) RESTORING (b). Differences can be seen in the temperature and density field. While in HIGH the WDW ($\theta > -1.5$°C) lies very high up in the water column ($\approx$ 100 m depth) and reaches onto the continental shelf, it is located below the shelf break depth of $\approx$ 400 m in RESTORING, associated with a sharper front. Furthermore, it has been shown earlier, that although the structure of the WDW layer is maintained better in HIGH compared to LOW, the density of the WDW over the continental slope is about 0.1 kg m^{-3} lower ($\approx$ 27.7 kg m^{-3}) than the observed WDW (see Figure 4.10d). This feature persists all the way to the southern continental shelf in HIGH, where, as a result, WDW enters the shelf in

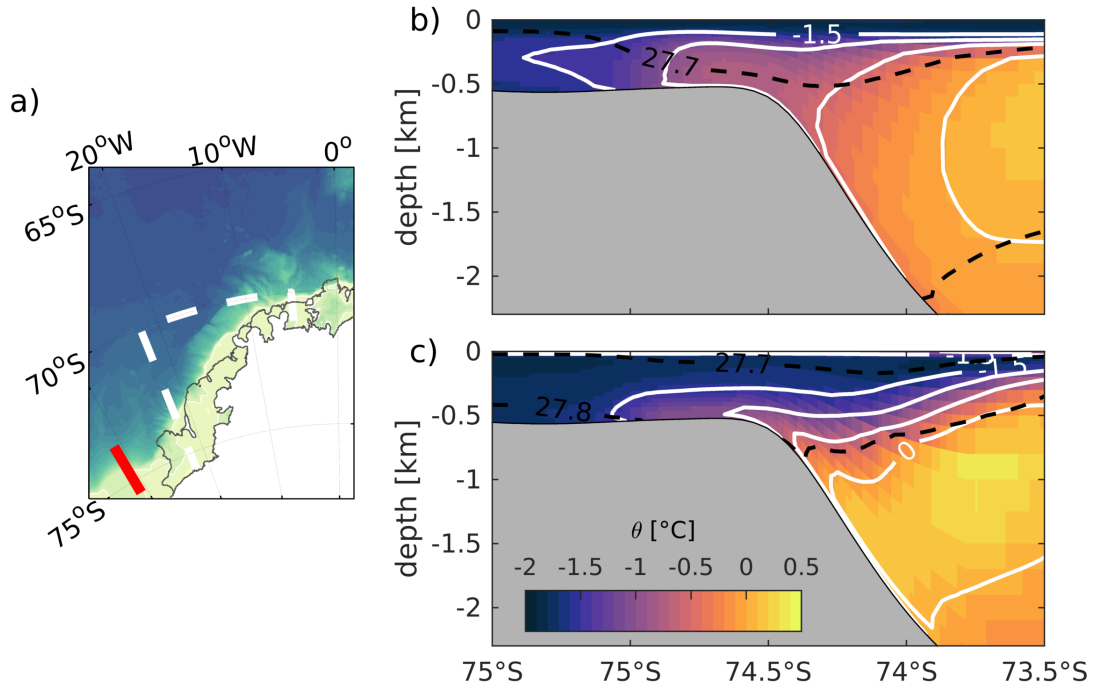

Figure 5.2: a) Bathymetric map showing the extent of the restoring area for run RESTORING. The red line marks the location of the section 31W. Shown is a 10-year mean potential temperature θ section for HIGH (b) and RESTORING (c). Black dashed lines represent potential density referenced to surface pressure in 0.1 kg m^{-3} intervals. White lines are isotherms in 0.5°C intervals.

form of a thick layer causing a too strong warm inflow (see Figure 4.10c). This is corrected in run RESTORING and the WDW core has now a density above 27.8 kg m^{-3} and lies at about 1000 m depth. This agrees with the observations, from the shelf break east of the Filchner Trough, shown in Figure 3.4

The western boundary of the restoring is chosen, such that the ocean can evolve freely before encountering the continental shelf west of Brunt Ice Shelf. In order to assess the effect of the restoring on the ASF properties, the 10-year mean potential temperature is plotted along section 31W (Figure 5.2), for HIGH (b) and RESTORING (c). An improvement can be seen in RESTORING; the isotherms and isopycnals show a dip over the shelf break, with a thicker ($>$ 200 m) WW layer above. Furthermore, the warmest and densest water ($\sigma_\theta > 27.8\,\mathrm{kg\,m^{-3}}$, $\theta > -0.5$°C) is suppressed and the lighter MWDW ($\sigma_\theta < 27.8\,\mathrm{kg\,m^{-3}}$) enters the shelf along the bottom.

This model set-up leads to realistic ASF properties and will be used in the

following to study the flow of MWDW onto the continental shelf and, ultimately, toward the FIS front.

5.2 Mean circulation and hydrography on the southern Weddell Sea continental shelf

After a short assessment of the simulated hydrography and circulation on the southern Weddell Sea continental shelf, the focus will be shifted to the MWDW inflow along the eastern flank of the Filchner Trough. The model is able to reproduce key features over the continental shelf, which can be illustrated by a hydrographic section crossing the continental shelf from east to west as shown in Figure 5.3:

- In agreement with observations (*Gammelsrød et al.*, 1994), most saline waters in the order of 34.8 are formed over the western part of the continental shelf and enter the ice-shelf cavity via the western flank of the Ronne Trough (*Nicholls et al.*, 2003). This results in an east-west density gradient, which has been suggested to be an important driver for the cavity circulation *Timmermann et al.* (2002), with inflow at the Ronne side and outflow at the Filchner side.

- Warm water enters the continental shelf along the bottom on the eastern side of the Filchner Trough and to the west of Berkner Bank. The inflow along the Filchner Trough occurs above the 500 m isobath, while the trough is filled with dense and cold water.

- A strong northward flow, transporting cold water along the eastern slope of the Filchner Trough, is simulated, as described, based on observations, by *Darelius et al.* (2014a) and also seen in the CTD-data presented in this thesis.

These features are also captured by run HIGH, hence without restoring (Figure 5.4), which suggests that the model is generally performing well. Furthermore, it can be seen in Figure 5.4b how the MWDW inflow over the Filchner Trough is stronger in HIGH compared to RESTORING. In HIGH, temperatures above $-1.8°C$ are found at mid-depth across the whole trough in the mean field and cores with $\theta > -1.6°C$ are present at both flanks. These cores are smaller and cooler

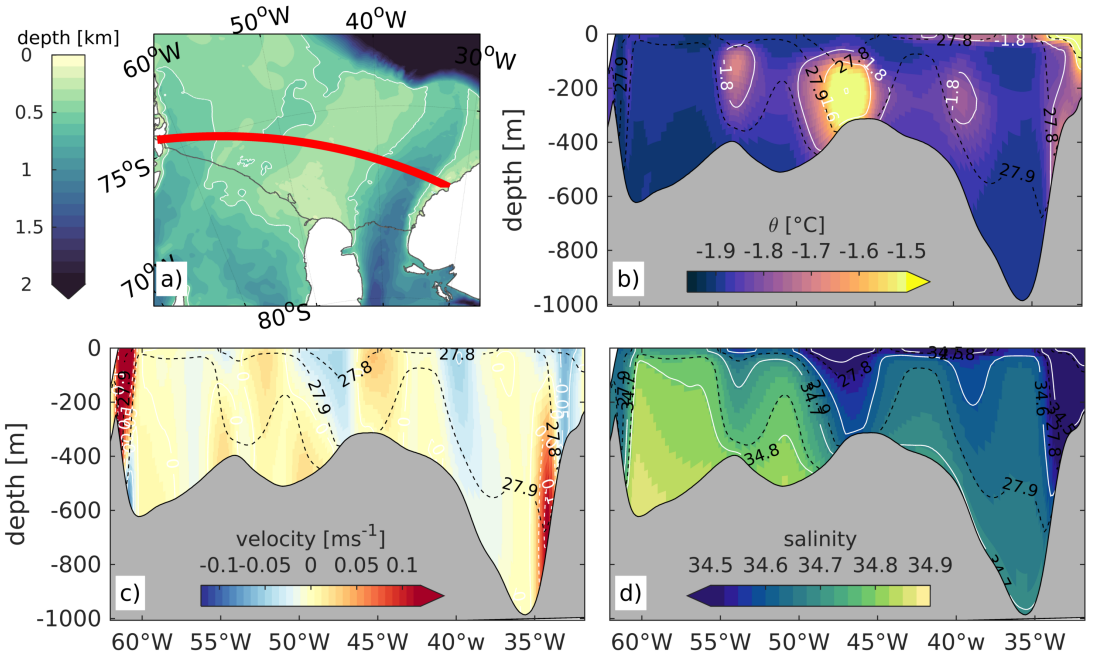

Figure 5.3: a) Bathymetric map (RTopo-2), where the white contour represents the 500 m isobath and the grey line the ice shelf front. The red line marks the hydrographic sections, from RESTORING, shown in b) potential temperature, c) velocity normal to the section and d) salinity, averaged over 2000-2010. Dashed black contours in b)-d) represent potential density referenced to surface pressure. White contours in b) are isotherms in 0.2°C intervals and in d) isohalines in 0.1 intervals.

in RESTORING and and temperatures in the centre of the trough do not exceed −1.8°C. Generally, salinities on the continental shelf are higher in RESTORING, which may be partly attributed to the fact that denser water enters the continental shelf, due to the restored ASF properties (see Figure 5.2). An additional factor could be fresh water input from the Brunt Ice Shelf, as the salinity section in HIGH (Figure 5.4) indicates largest differences along the eastern part of the section.

A deficiency of the model (HIGH and RESTORING) is, that no ISW significantly colder than −1.9°C is transported across the FIS front into the Filchner Trough. Therefore, the thick ISW layer as shown in Figure 3.10, is not present in the model. However, the modelled trough is filled with cold, dense water, whose signature is clearly distinguishable from surrounding water masses and represents the coldest and densest water mass in the Filchner Trough. In particular, the water is denser than the off-shelf WDW, which is important as it prevents a direct

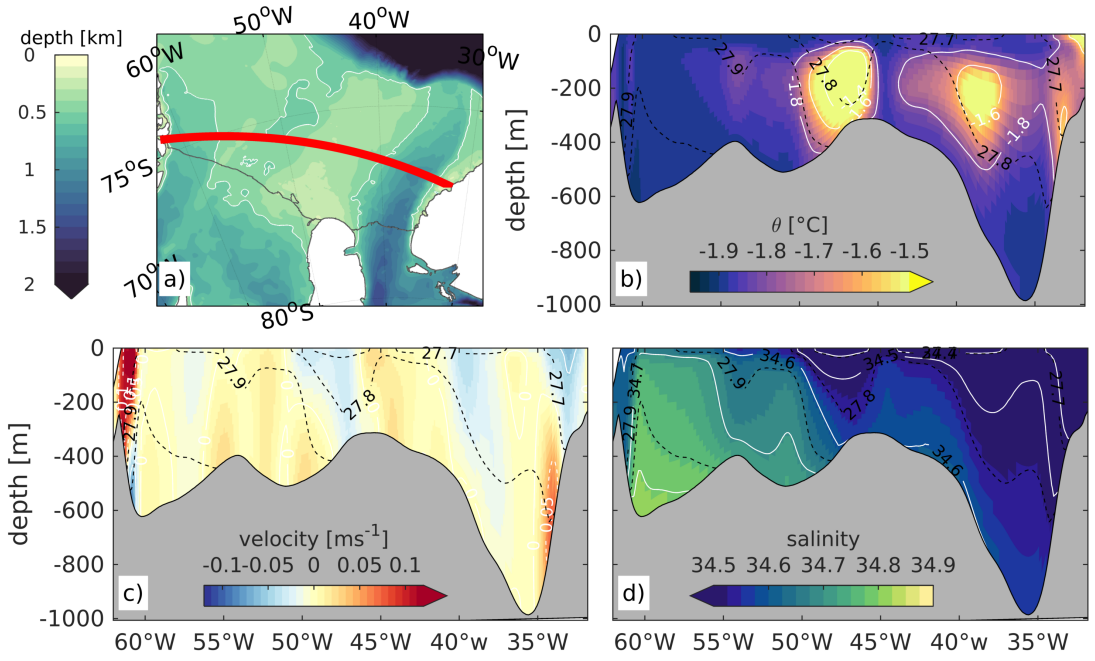

Figure 5.4: Same as Figure 5.3 but for HIGH

warm inflow via the trough and an hypothesized irreversible warm inflow (*Hellmer et al.*, 2017). Furthermore, this dense water contributes to the dense water production in the Weddell Sea, once it crosses the Fichner Sill. In the following I will refer to this dense water mass, as Filchner overflow water (FOW).

Observations show the coldest ISW outflow at the western flank of the trough close to the ice shelf front (*Gammelsrød et al.*, 1994; *Grosfeld et al.*, 2001; *Darelius and Sallée*, 2018). This outflow is absent in the model, instead a southward flow of MWDW is found at mid-depth ($\approx 300\,\mathrm{m}$) over the western flank of the trough (see Figure 5.3b,c). A hydrographic section across the Filchner Sill shows MWDW at the western side of the sill, overlying the ISW layer (Figure 3.2b and *Grosfeld et al.* (2001)), however, no traces of MWDW have been observed in the hydrographic sections taken across the FIS front (*Gammelsrød et al.*, 1994; *Grosfeld et al.*, 2001; *Darelius and Sallée*, 2018). The modelled southward flow is particularly strong at the beginning of summer (not shown) and may be attributed to too strong dense water production on Berkner Bank in winter. This dense water production creates a horizontal density gradient, as indicated by the $27.9\,\mathrm{kg\,m^{-3}}$ isopycnal in Figure 5.3 at $\approx 40°\mathrm{W}$, which sets up a southward flow due to the thermal wind balance. The western warm inflow is also found in idealized model results by *Daae*

et al. (2017) in the case of a dense western shelf. This should be addressed in future simulations, however, it does most like not influence the inflow of MWDW along the eastern flank of the trough.

I conclude that the restoring approach leads to a significant improvement of the Filchner Trough hydrography and is, despite the general model deficiencies, suited for a more detailed analysis of the MWDW inflow along the eastern flank of the Filchner Trough.

5.3 Modelled inflow of MWDW along the eastern flank of the Filchner Trough

In this thesis, a tight link is maintained between model results and available observations on the southern Weddell Sea continental shelf. Generally, observations are used to validate models, however, this can also be done vice versa. As shown in the previous sections, the model is able to capture key features of the shelf hydrography and, due to the restoring, also simulates the right ASF properties. Therefore, the model can be used to integrate the mooring results, presented in section 3.2, into a broader picture. This allows an assessment of how representable of the general circulation the observations are.

Figure 5.5 shows 10-year mean (2000-2010) simulated bottom potential temperature (a), salinity (b) and meridional velocity in colour with normalized current vectors (c). The mooring locations at 76°S are marked as coloured diamonds. In agreement with the mooring data, $M_{31.5W}$ is located in the cold water layer in the model, while M_{31W} and $M_{30.5W}$ lie within the warm inflow band. Observations show a roughly 2-week shift during the warm inflow period between $M_{30.5W}$ and M_{31W}, where the signal appears first in the east and then propagates to the west (see Figure 3.11a,b). This agrees with the modelled warm water tongue, which shows an eastward deflection at roughly 75°S and turns westward again just north of the mooring locations. Mean seasonal fields (not shown) show a delayed westward spreading of this warm water tongue, which would explain the observed shift in the moorings. The model results suggest that the moorings are located in an adequate position to capture the main inflow path.

The eastward deflection of the warm water tongue is also reflected in the velocity field (Figure 5.5c), and, as a result, the northward flow crosses the 500 m isobath and a small recirculation cell is formed. Looking closer at bathymetry, the

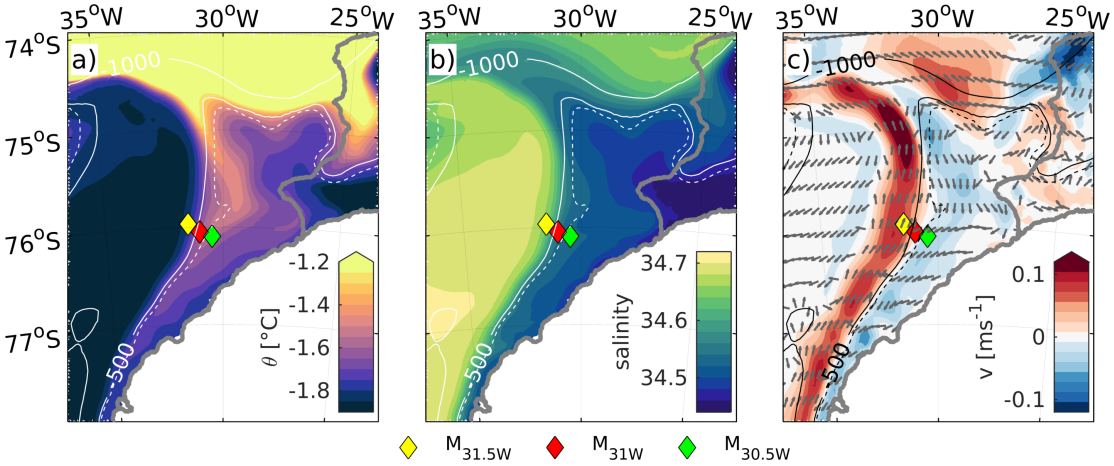

Figure 5.5: Modelled 10-year (2000-2010) mean bottom potential temperature a), salinity b) and meridional velocity c) in the north eastern corner of the Filchner Trough and the adjacent contiental shelf. White and black contours (solid) in a)-b) and c), respectively, represent isobaths from the model bathymetry in 500 m intervals. Dashed contours represent the 450 m isobath. The thick grey line over the ocean marks Brunt Ice Shelf. Coloured diamonds mark mooring positions as described in the legend. Grey vectors in c) represent the bottom circulation (normalized vectors).

450 m isobath (dashed contour in Figure 5.5) shows an eastward excursion just north of the moorings, which is a likely explanation for the shape of the warm inflow path.

The mean modelled velocity field depicts a band of almost purely westward velocities at about 76°S. M_{31W} shows a distinct westward flow in winter, which, however, is not as pronounced at $M_{30.5}$. Hence, it is possible that M_{31W} is located at the southern edge of the described recirculation cell, which can lead to persistent westward flow in winter. Seasonal and interannual variability in the in- and/or outflow strength can cause a shift of this cell, such that northward flow is observed at the moorings, as it was the case in one year (2014) of the time series. The observed westward flow in winter and the shift in the temperature signal were two main features during the observational analysis that required further assessment that was not possible based on the available observations. The model provides conclusive answers to both, which advances the current stage of knowledge of the shelf circulation.

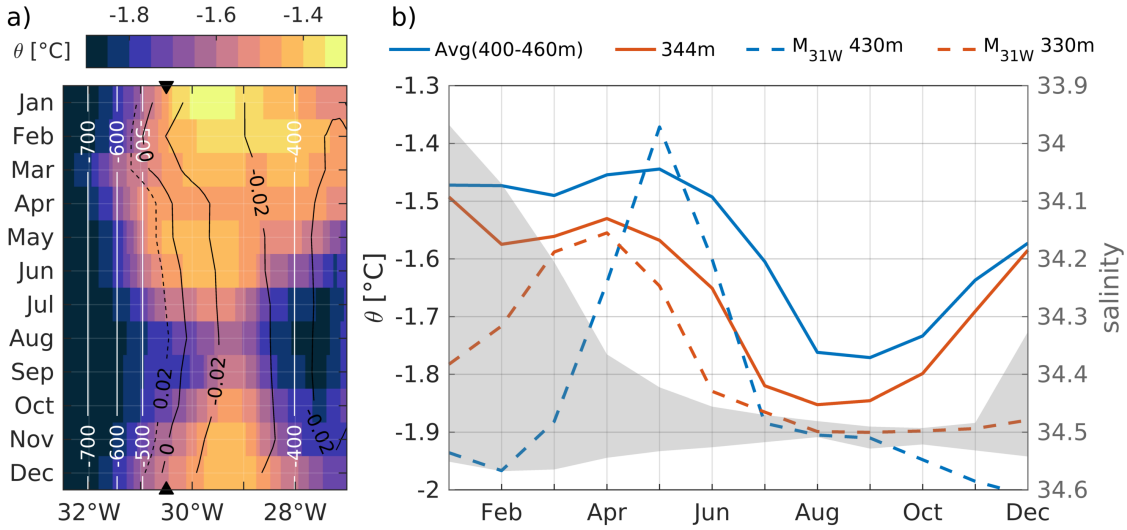

Figure 5.6: a) Hovmöller diagram showing the mean seasonal cycle (2000-2010) of modelled temperatures averaged over the bottom three layers along 76°S. White contours represent the bottom depth along the model section in 100 m intervals. Black contour represents meridional velocity (dashed=northward, solid = southward) b) Mean simulated seasonal cycle (2000-2010) at 30.5°W, 76°S at 344 m depth in blue and averaged over the bottom three layers ($400 - 460$ m) in orange. Dashed lines represent monthly mean values averaged over two years (2014,2015) at the two depth levels from mooring M_{31W} (see Figure 3.6). Grey shading represents envelope of mean modelled seasonal salinity of all layers at 30.5°W, 76°S.

5.3.1 MWDW at 76°S

One goal of this chapter is to extend the study of the seasonal inflow of MWDW. After evaluating the general shelf circulation in the model, a direct comparison of the model and the moorings observations at 76°S will be undertaken in this section, with the focus on the mean seasonal hydrography.

In order to investigate the modelled mean seasonal inflow of MWDW at 76°S, a hydrographic section at this latitude was extracted. Figure 5.6a) shows the 10-year mean (2000-2010) seasonal evolution of temperature, averaged over the bottom three layers ($\approx 400 - 600$ m), as a Hovmöller plot. The major southward flow of MWDW occurs over isobath range of $400 - 500$ m (see Figure 5.6a, white contours). Above the slope, FOW is transported northward, creating a shear zone roughly above the 500 m isobath.

A seasonal cycle can be seen in the inflow band, with warmest temperatures ($> -1.5\,°C$) from January to June, followed by a cooling from July to October. This cooling is most pronounced over the shallower part of the shelf (< 400 m),

while a thin band of temperatures around -1.6°C persists throughout winter further west. The seasonal temperature signal is accompanied by a lateral shift of the velocity shear, indicated by the zero velocity contour (Figure 5.6a), where northward flow extends further up-slope in winter, in agreement with the mooring observations. Furthermore, not all MWDW is transported southward, but some is recirculated to the north over the deeper slope, which is indicated by the warm temperatures ($\theta > -1.6$°C) west of the zero-velocity contour in Figure 5.6a.

Based on bottom depth and seasonal temperature (warm summer inflow and cooling in winter), as well as the velocity signal (seasonal east-west shift), longitude 30.5°W seems closest to the mooring observations at M_{31W}. The mean modelled seasonal temperature cycle at 30.5°W (see black triangles in Figure 5.6a) is shown in Figure 5.6b), again as average over the bottom three layers. Additionally, a shallower model layer (344 m) is shown together with the monthly mean averages over the whole mooring time series at M_{31W} at both depth levels (330 m and 430 m, dashed lines). The modelled maximum temperatures lie within the range of the observations (≈ 1.5°C) and the observed time shift (see Figure 3.6) between the mid-depth (330 m) maximum and the maximum at the bottom (430 m) of roughly one month is captured.

Based on the presented mooring observations, it was suggested, that deep convection sets in winter, leading to a cold, weakly stratified water column and eroding possible remnants of MWDW on the continental shelf. Temperatures in the model also drop significantly and reach a minimum in August, although the thermocline at the continental shelf break is not suppressed in winter (due to the restoring further upstream). The presence of convection becomes more clear in the modelled salinity distribution, which is shown, comprising all model layers, as grey shading in Figure 5.6b). Between July and October, the salinity at all levels lies within a very small range around 34.5, in contrast to a much larger range in summer ($\Delta S \approx 0.6$), where a fresh surface layer is present due to sea ice melt. The weak winter stratification in the model goes along with modelled temperatures below -1.8°C at mid-depth and below -1.7°C in the bottom layers, indicating a cooling from the surface due to the convection. While the bottom layer at this location still shows a warm trace, temperatures further to the east, i.e., at bottom depth shallower than 400 m are close to the freezing point, suggesting that convection reaches all the way to the bottom there.

While observed temperatures on the continental shelf stay at the surface freez-

ing point until December and March at mid-depth and in the bottom layer, respectively, modelled temperatures increase already from September onward and high temperatures ($\theta > -.1, 6$), characterising MWDW, persist throughout summer and autumn. This can be attributed to the effect of the restoring, where the ASF is not suppressed in winter and warm water is present above the shelf break depth all year around. The fact that, nevertheless, the model reproduces a seasonal cycle similar to the observations, implies that winter convection over the continental shelf plays a vital role in the seasonal temperature evolution by limiting the southward heat transport.

5.3.2 Seasonal shelf hydrography

In the following, a broader look will be taken at the hydrography on the shelf and how it impacts the seasonal southward inflow of MWDW. For this, a hydrographic section has been defined along the mean inflow path (hereafter referred to as InflowNS), based on the 10-year mean (2000-2010) modelled bottom temperature field on the Eastern Shelf (see Figure 5.7a), from the Filchner Sill to the FIS front. Mean summer (Dec-Feb), autumn (Mar-May) and winter (Jun-Nov) temperature sections are shown in Figure 5.7b-d.

Summer hydrography is characterized by a pronounced warm, fresh surface layer because a large polynya is present each summer along the coast. The southern part of the section takes course close to the coast. Here, the surface layer extends to about 100 m depth, likely due to wind-driven coastal downwelling, that drives a coastal current. As a result, some of this warm surface water enters the cavity, as the presence of fresh basal melt water at the ice shelf base allows the isopycnals to connect across the front. However, this water does not penetrate far into the cavity (not shown). Measurements of ice shelf thickness show a rather steep FIS front (*Lambrecht et al.*, 2007), however, terrain-following vertical coordinates require more smoothing, for the ice shelf draft as well as bathymetry, to ensure numerical stability. Therefore, the model may be prone to an overestimation of flow into the cavity, which has also been suggested by, e.g., *Timmermann et al.* (2012) and *Naughten et al.* (2018).

Below the surface layer, isopycnals are shoaling toward the south in summer, indicating a positive density gradient from the north to the south. It is MWDW denser than $27.75\,\mathrm{kg\,m^{-3}}$ that flows southward along the shelf with temperatures above $-1.6°\mathrm{C}$, however, it is blocked by the presence of denser ($\sigma_\theta > 28\,\mathrm{kg\,m^{-3}}$)

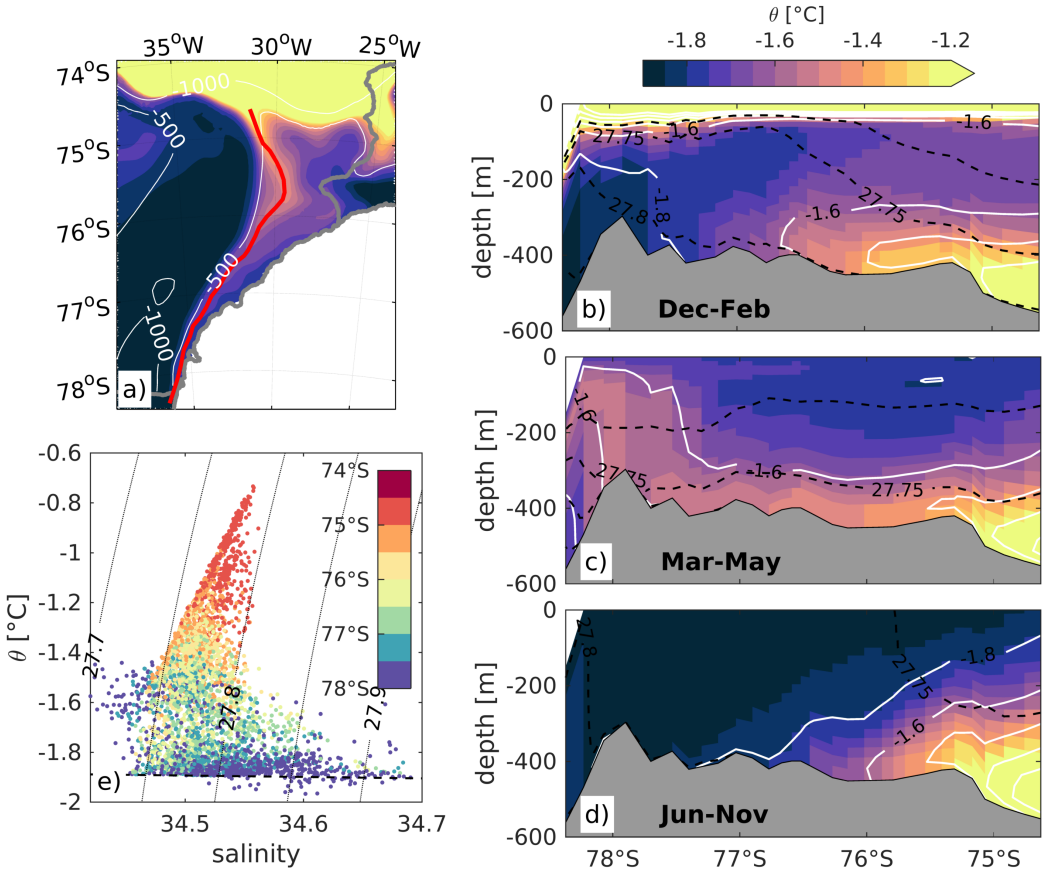

Figure 5.7: a) 10-year mean (2000-2010) modelled bottom temperature, with white contours representing model bathymetry (only 500 m and 1000 m isobath). The red line marks the hydrographic section (referred to as InflowNS) shown for summer (Dec-Feb) in b), for autumn (Mar-May) in c) and winter/spring (Jun-Nov) in d). Black, dashed lines represent potential density in 0.05 kg m^{-3} intervals between 27.7, kg m^{-3} and 27.9, kg m^{-3}. e) θS- diagram of the average over the bottom three layers along the section, where the colour shading shows the latitude. Thick, dashed line represents the surface freezing point and thin, black lines represent potential density in 0.05 kg m^{-3} intervals.

water south of about 76.6°S. In autumn, the isopycnals flatten and the densest bottom layer has either eroded or retreated from the Eastern Shelf, allowing for a southward spreading of MWDW up to 78°S. This agrees with observations published by *Darelius et al.* (2016), who observed MWDW close to the ice front for the first time in 2013. The pulse appeared in mid-April. South of 77.5°, temperatures above −1.6°C cover almost the whole water column, suggesting that fresh warm water above 300 m depth has been transported southward within the boundary current, while only the denser water resembles MWDW.

Looking at the section data in θS space, with colour marking the latitude, shows, that the MWDW is significantly modified along its path, forming the characteristic straight line between WDW and WW. The majority of the water at 78°S has temperatures below -1.8°C and salinities above 34.45. Warm temperatures up to -1.4°C are also found, however, they are associated with the significantly fresher, hence, lighter surface water. As shown in Figure 5.7, it is this water that can enter the ice shelf cavity due to a smoothed ice shelf front.

5.3.3 Interannual variability of MWDW inflow

It was shown that in the mean modelled state MWDW reaches the ice shelf front during autumn with temperatures between -1.6°C and -1.4°C, which are significantly cooler than at the sill. In winter, the southern part of the shelf water becomes denser due to convection, impeding a southward penetration of the lighter MWDW past 76.5°S. In this section, I will investigate the interannual variability of the warm inflow along section InflowNS.

Figure 5.8 shows a Hovmöller diagram of temperature averaged over the bottom three layers along section InflowNS. The described seasonal southward propagation of MWDW and its modification along its path can be seen. The inflow reaches 78°S every year, however, does not enter the cavity (south of red line) significantly. As seen in Figure 5.7a), the Eastern Shelf (shallower than $500\,m$), where the southward spreading of MWDW is seen in the model as well as observations, becomes very narrow south of 77°S. As long as the trough is filled with dense water, there is, therefore, no direct pathway into the cavity, in particular in case of a deeper ice shelf draft in reality.

Higher temperatures (up to 1°C) are found in the second half of the analysis period, i.e., from 2005 onward, which is particularly prominent at the sill (north of 75°S) but also further south on the shelf up to about 77°S. It has been suggested by *Stewart and Thompson* (2016) and *Daae et al.* (2017) that denser water on the continental shelf leads to a stronger warm inflow, as dense isopycnals on the shelf connect with off-shelf isopycnals, forming a v-shaped front. Bottom density is shown as white isolines in Figure 5.8 and it can be seen that the shelf is denser prior to winter 2005, hence, when the temperatures were lower. Here, the $27.8\,\mathrm{kg\,m^{-3}}$ isopycnal covers the southern part of the section almost the whole year and extends all the way to the sill during summer. One exception is found in summer 2002/2003, where the northern shelf stays lighter (fresher), associated

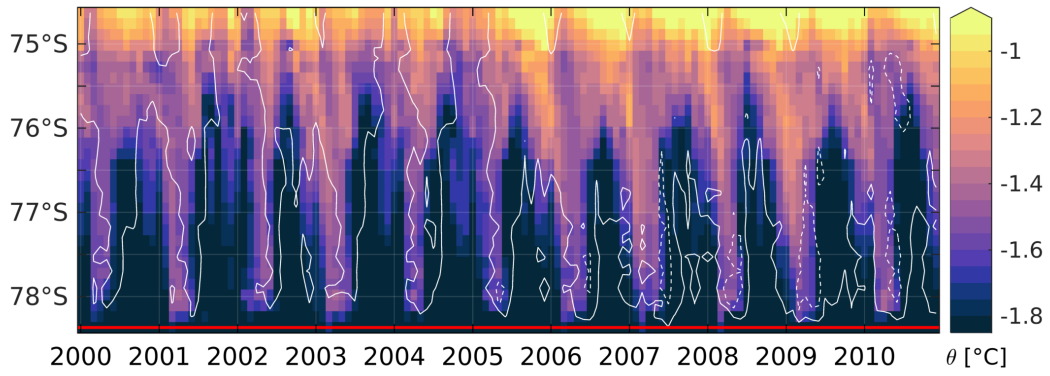

Figure 5.8: Mean modelled potential temperature averaged over three bottom layers along section InflowNS in RESTORING. White contours represent bottom density (full line: 27.8 kg m^{-3}, dashed line: 27.75 kg m^{-3}). The red line marks the position if the ice shelf front

with a warmer signal at the sill.

From winter 2005 onward, the 27.8 kg m^{-3} isopycnal does not extend beyond 76°S and also the period of the southern shelf being denser than 27.8 kg m^{-3} is shorter, resulting in a fresher shelf in summer and autumn. Understanding processes controlling the MWDW flow, is of particular interest in order to assess a possible sensitivity to future climate change. To deepen this analysis, the data will be split into two time periods, from 2000 to 2005 (hereafter referred to as period 1) and from 2006 to 2010 (hereafter period 2).

Figure 5.9 shows the difference in potential temperature, averaged from December to May (summer + autumn), of period 1 minus period 2 (Both individual sections are shown in Figure A.4). It can be seen that the bottom layer is significantly warmer ($\approx$ 0.4°C) in period 2 compared to period 1 (negative values). Above the bottom layer, positive values indicate warmer temperatures over a thick layer in period 1. Generally, largest differences are found at the sill, while they become gradually smaller toward the south.

Additionally, two isopycnals, representing the range of MWDW (27.75 kg m^{-3} & 27.8 kg m^{-3}, see Figure 5.7), are plotted for each period (green). In period 1, densities above 27.8 kg m^{-3} are found at the bottom of the continental shelf, associated with colder temperatures. Generally, the shelf is denser in period 1, indicated by the depth difference of the 27.75 kg m^{-3} isopycnal, which is found about 100 m higher up in the water column in period 1.

These results suggest that denser water in the south in period 1 blocks the

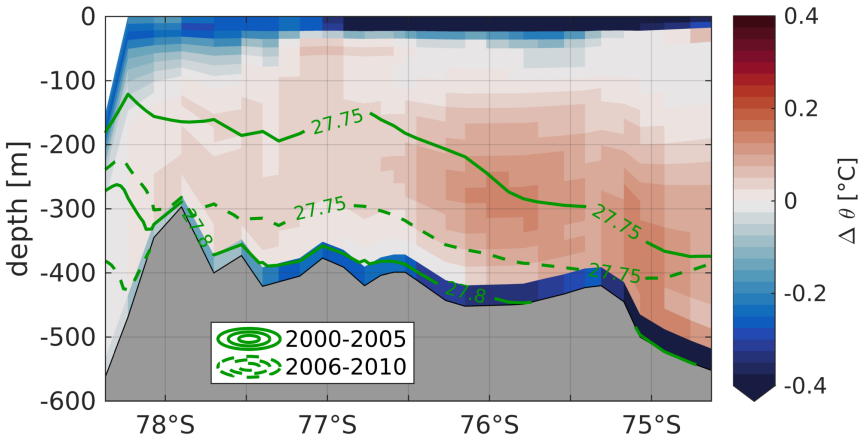

Figure 5.9: Difference in modelled potential temperature, averaged over summer and autumn (Dec-May) between 2000-2005 (period 1) and 2006-2010 (period 2) along section InflowNS (period 1 minus period 2). Green contours represent selected isopycnals for period 1 (solid) and period 2 (dashed).

lighter MWDW and lifts it off the bottom, leading to a colder and denser bottom layer. In period 2, the inflow occurs along the bottom, as the dense bottom layer is absent. This explains the warmer signal found in Figure 5.8.

While the bottom temperatures are higher in period 2, temperatures above are warmer and the thickness of the MWDW layer spreading southward is larger in period 1. This can partly be caused by an uplift of isopycnals at the shelf break due to the denser outflow, granting an easier access for the off-shelf MWDW as proposed by *Daae et al.* (2017). This also affects the warm inflow (see Figure 5.3) at mid-depth over the western flank of the trough, which is warmer during period 1, likely due to the uplift of MWDW at the sill (see Figure A.3).

The question arises as to what drives the interannual changes in the trough's density. One possible factor is sea ice and associated dense water production on the continental shelf. The Filchner Trough can be influenced mainly by two ways. First, by dense water production on the Ronne side, which will lead to denser water in the cavity and, ultimately, outflow on the Filchner side. Second, by sea ice production on Berkner Bank and directly over the Filchner, which can feed dense water directly into the trough as seen earlier in Figure 5.3.

Figure 5.10a shows a map of the difference of the mean ice production rates over period 1 and 2. The pattern exhibits larger ($\approx 1\,\mathrm{m\,y^{-1}}$) ice production over the southern part of the continental shelf in period 1, being particularly strong along the ice shelf front and on the Ronne side. Over large parts of the remaining shelf,

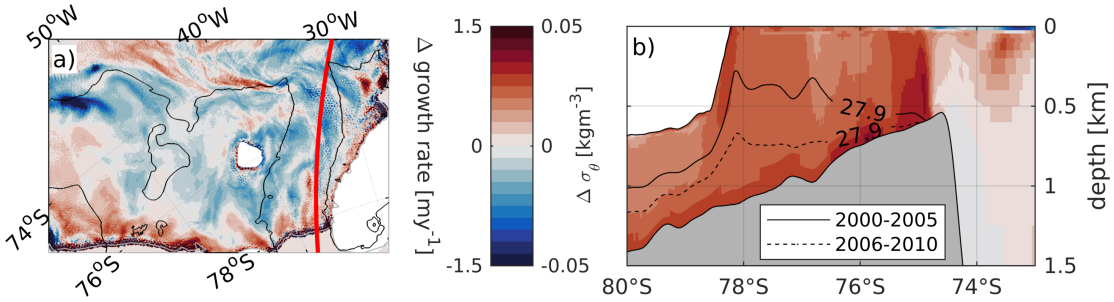

Figure 5.10: a) Difference of the mean sea ice production rate between period 1 (2000-2005) and period 2 (2006-2010). Black contour represents the 500 m isobath from RTopo-2 (*Schaffer et al.*, 2016). The white feature west of the Filchner Trough represents a large grounded ice berg (A23-A). b) Potential density difference between period 1 and 2 (1 minus 2) along a hydrographic section through the Filchner Trough (see red line in a)). Black isolines represent the mean position of the 27.9 kg m^{-3} isopycnal in period 1 (solid) and period 2 (dashed).

however, the difference is negative, hence, higher production in the second period. Figure 5.10b shows the density difference between the two periods, together with the mean position of the 27.9 kg m^{-3} isopycnal and it can be seen that significantly higher densities are found within the whole trough in period 1 (positive values). The layer thickness of water denser than 27.9 kg m^{-3} is about double in period 1 compared to period 2. While it is difficult to quantify contributions from Ronne and Berkner, the shoaling isopycnals toward the ice front in period 1 suggest that local convection does play a large role, which is further supported by the pattern of the density difference, showing a maximum directly at the ice front.

Other maxima in the density difference are found at the sill (north of 76°S) at the bottom, which cannot be directly linked to the sea ice production rates, however could be attributed to a denser overflow in period 1. It was shown in Figure 5.5 that the northward flow turns westward at the sill. Due to the location of the hydrographic section, this outflow crosses the section at the sill.

5.4 Discussion

The current understanding of the hydrography and ocean circulation on the southern Weddell Sea continental shelf has been patched together from observations and model results over a long period of time. The presented model simulation reproduces many of the key observed features on the continental shelf and further advance the current understanding of the shelf circulation along the eastern

flank of the Filchner Trough. No other model, regional or global, with a realistic set-up is currently available for this very complex region. Many models require restoring of sea surface salinity in order to achieve realistic water masses over the continental shelf or to prevent the occurrence of a spurious Weddell polynya (e.g. *Naughten et al.* (2018)).

The regional restoring approach, as a simple tool of data assimilation, has proven to be an efficient tool to improve the representation of the modelled ASF and, ultimately, the flow of MWDW onto the southern continental shelf. This set-up allows for a direct comparison with mooring observations and, at the same time, serves as a sensitivity study. Observations show a seasonal heaving of the ASF, which lies shallower in summer, allowing an on-shelf flow of MWDW, while it is suppressed below the shelf break depth in winter (*Årthun et al.*, 2012). It was shown in section 3.2, that the warm signal observed at the moorings at 76°S can be connected to this seasonal evolution of the ASF. It was further suggested that the observed seasonal cycle, with the warm inflow being limited to summer/autumn, is a combination of the seasonal cycle of the ASF depth and winter time convection over the continental shelf. By applying restoring to only summer hydrography, where the ASF is not suppressed in winter, one can investigate the influence of the continental shelf on the southward propagation of MWDW toward the FIS front.

The results show that, despite the upstream restoring to summer hydrography, a clear seasonal cycle on the continental shelf is produced by the model, which is comparable to the mooring observations at 76°S, with maximum temperature toward the end of summer/beginning of autumn and a significant cooling and weakly stratified water column in winter. The model results suggest that shelf convection plays a key role in limiting the southward penetration of MWDW in winter. While available observations show that the ASF depth increases in winter, therefore, preventing the on-shore flow of MWDW (*Årthun et al.*, 2012), a multidecadal warming associated with a shoaling of the mid-depth temperature maximum is suggested to provide greater access for warmer, saltier water to the continental shelf around Antarctica (*Schmidtko et al.*, 2014). Therefore, the role of the winter shelf convection is important in limiting the heat transport to ice shelves and might become more important in the future. However, model projections suggest a decrease of sea ice production in a future warming climate, which will in turn decrease the strength of convection (*Timmermann and Hellmer*, 2013).

Hence, the shoaling of the ASF in combination with decreasing sea ice formation will increase the potential for a warm inflow into the FRIS cavity. *Hellmer et al.* (2017) show that once the warm inflow into the cavity has started the system is irreversible.

MWDW was observed in the vicinity of the ice front for the first time in 2013 (*Darelius et al.*, 2016). A comparison of hydrographic sections at 76°S from the beginning of January in 2013, 2014 and 2016 (Figure 3.10) showed that in 2013, warmer and denser MWDW was present, compared to the other years, suggesting an earlier onset of the warm inflow. Therefore, the MWDW would have more time to propagate southward before the winter convection sets in. The model results show MWDW reaching the FIS ice front every year, although strong convection sets in. Due to the restoring, the warm inflow starts also early in the model and the warm water can reach the front, before it is eroded in winter. Hence, the onset of the inflow seems to be an important factor in determining whether MWDW can reach the ice front or not.

Generally, the model shows that the MWDW is modified significantly by the time it reaches the ice front and mean temperatures are found between -1.6°C and -1.4°C, agreeing with the observed MWDW trace in 2013, which showed maximum values of -1.4°C (*Darelius et al.*, 2017). Higher temperatures are only found north of 77°C in the model. Furthermore, the model results suggest, that there is no direct inflow of MWDW into the cavity along the Eastern Shelf. The southward flow of warm water in the bottom layers is limited to the shallower part of the shelf east of the 500 m isobath, which does not extend into the cavity (see Figure 5.7). Instead, it was found that AASW enters the cavity along the ice shelf base in summer, which may partly be attributed to an unavoidable smoothing of the ice front related to the terrain-following coordinates (in agreement with *Naughten et al.* (2018)). This explains the simulated high melt rates in summer along the FIS front (Figure 4.2). Although this melting is likely overestimated, no information about the real seasonal cycle is available due to the lack of observations.

Interannual variability of the modelled warm inflow (along section InflowNS) was found to be depending on the density in the trough. From 2000-2005 the FOW in the whole trough is significantly denser, which is expressed in lifted isopycnals, and results in a denser bottom layer also on the shelf east of the trough. This dense layer blocks the warm inflow along the bottom and lifts the MWDW core.

In contrast, maximum temperatures (up to 1°C higher at the sill) are found along the bottom between 2006-2010. Despite warmer bottom temperatures in period 2, the MWDW layer ($27.75\,\mathrm{kg\,m^{-3}} < \sigma_\theta < 27.8\,\mathrm{kg\,m^{-3}}$) on the shelf was about twice as thick in period 1 compared to period 2, thus, leading to warm inflow over a larger part of the water column. A future task would be to perform a heat budget analysis, in order to determine in which of the two phases more heat is carried southward.

It was shown that the differences between the periods might be due to stronger sea ice formation over the southern continental shelf in period 1 compared to period 2. *Petty et al.* (2014) state that the net salt flux from sea ice production or melt dominates the depth of the mixed layer over the continental shelf around Antarctica. Therefore, higher production rates are likely the cause of an overall denser shelf in the simulation. Reasons for the variability of the sea ice production rates are likely connected to the forcing, however, this would need further analysis in the future.

5.5 Summary

The aim of this Chapter was to study the MWDW flow onto the southern Weddell Sea continental shelf and, ultimately, toward the FRIS in FESOM. It was shown in the previous chapter that the ASF properties upstream of the Filchner Trough improve with higher resolution, however, are not sufficiently well represented in the model to study the inflow of MWDW. Therefore, I developed a new model configuration, where the 3-D field of temperature and salinity upstream of the Filchner Trough is restored to a modified version of the WOA13. For this I used a newly available climatology that combines hydrographic observations from ship cruises as well as data from CTD-tagged seals along a section cross-cutting the continental slope at Kapp Norvegia ($\approx 17°$W) and implemented this data into the WOA13 over a defined patch. The model temperature and salinity were restored with a time scale of 3 hrs. I found that this approach leads to a greatly improved representation of the ASF and, ultimately, of the MWDW flow onto the shelf. The model simulation was used to integrate the mooring observations (presented in section 3.2) into a broader picture with a modelled seasonal cycle at 76°S that is comparable to the one identified from mooring observations. It was shown that winter convection over the continental shelf limits the southward propagation of MWDW, thereby, impeding a year-long inflow, even if MWDW is present at the sill all year around. Furthermore, the model results suggest that, at present day conditions, there is no direct pathway for MWDW east of the Filchner Trough to enter the cavity. Due to high densities within the Filchner Trough, the southward flow of MWDW is limited to bottom depths shallower than 500 m, however, this part of the continental shelf becomes very narrow toward the FIS front and does not reach into the cavity. Finally, it was found that higher densities in the Filchner Trough and its eastern flank can lead to broader warm inflow at mid-depth, while lower densities allow a stronger inflow along the bottom, which, however, occurs over a smaller depth range. It will be important to address the question, which of the two observed situations creates a larger southward heat transport and, ultimately, increases the possibility of a warm water transport into the cavity.

6. Conclusions and Outlook

The aim of this thesis was to study the MWDW flow onto the southern Weddell Sea continental shelf, with focus on the Filchner Trough region. For the first time, the seasonality of the hydrography along the eastern flank of the trough could be described, based on mooring observations. Furthermore, a global configuration of FESOM was applied with increased resolution over the Weddell Sea ($\mathcal{O}[10\,km]$) and an even higher resolved continental shelf ($\mathcal{O}[3\,km]$). Additionally, a model-restoring approach has been developed in order to test the sensitivity of the modelled warm inflow to the ASF representation in the model. The main objectives formulated for this thesis were:

1. Observations at the shelf break show a seasonal flow of MWDW onto the continental shelf at the eastern side of the Filchner Sill (*Årthun et al.*, 2012) and warm pulses have been observed for the first time close to the FIS front in 2013 (*Darelius et al.*, 2016). However, little is known about the seasonal and interannual variability along the eastern flank of the Filchner Trough. What is the seasonal variability of the MWDW inflow downstream of the shelf break? What are the main processes involved?

2. With exponentially increasing computational power and data storage capabilities, more powerful ocean models are being developed. In this thesis, a global configuration of the Finite Element Sea Ice - Ocean Model (FESOM), which allows a local mesh refinement. How well is the Weddell Gyre circulation represented in low and high resolution simulations and how does it influence the cross-shelf exchange in the southern Weddell Sea?

3. How do the model results compare to observations and can the model reproduce a realistic flow of MWDW onto the continental shelf? If so, what is the interannual variability and can MWDW enter the FIS cavity via the Eastern Shelf?

In the following, I will provide conclusions specific to each objective, followed by an overall conclusion and an outlook of planned, as well as proposed, future work.

1. Generally, the Filchner Trough is filled by a thick layer of ISW, while MWDW enters the continental shelf to the east of the trough, creating a strong temperature and density front. A distinct seasonal cycle is found along the eastern flank of the Filchner Trough, which can be described by four phases (see Figure 3.9). MWDW is found on the continental shelf at 76°S between January and June, which can be described in two separated phases. In Phase 1, spanning roughly from January to February, MWDW is only present at mid-depth with increasing temperatures toward the end of the phase ($\theta \approx -1.5$°C). At the same time, the bottom layer depicts a mean northward flow of ISW, due to an eastward extent of the ISW layer, which is most likely blocking the lighter MWDW further north . In the following phase (Phase 2), the ISW retreats, by either a dynamical process or erosion (needs further investigation), and a persistent southwestward flow sets in, transporting denser MWDW southward along the bottom. Maximum temperatures at the bottom are reached in June and exceed -1.5°C, while temperatures at mid-depth have started to decrease. By the beginning of July, temperatures in the water column have dropped to the surface freezing point ($\theta = -1.9$°C), associated with a weak stratification, which marks the beginning of Phase 3. This phase lasts for about three months (July to October), during which temperatures stay at the surface freezing point, while a steady increase in salinity indicates active shelf convection. Furthermore, the flow, depicts a strong westward component during this period, which may be driven by a North-South density gradient on the shelf. With the onset of surface melt in October, the salinity increase terminates and Phase 4 starts. This phase is characterised by the appearance of ISW along the bottom, which is associated with a northward flow component, while the temperature at mid-depth remains at the surface freezing point and salinity decreases slightly until the MWDW inflow starts in Phase 1. This seasonal cycle can be connected to the seasonal heaving of the ASF, which shoals during summer, allowing on-shelf flow of MWDW. Maximum temperatures at the shelf break, exceeding -1°C, are observed in March. In winter the ASF is suppressed and lays below the shelf break depth. A thick layer of

WW with temperatures around -1.8°C is present above. The MWDW takes about 2 months to travel from the shelf break to 76°S, which corresponds to a mean flow strength of about $2.5\,\mathrm{cm\,s^{-1}}$ in agreement with the observed current. Winter convection on the shelf leads to a densification of the water column, which likely blocks the shoaling MWDW at the shelf break from a southward propagation during spring. The main processes determining the observed seasonal cycle, are the depth of the ASF at the shelf break, the strength of winter convection, induced by sea ice formation and harsher atmospheric conditions, as well as the seasonal extent of the ISW onto the Eastern Shelf.

2. FESOM was run on two different meshes, one with a resolution of $4 - 73\,\mathrm{km}$ in the Weddell Sea (run LOW) and one with a resolution in the order of the Rossby radius, where minimum resolution is approximately 3 km over the southern continental shelf and the maximum resolution around 15 km in the northeastern corner of the Weddell Gyre. The representation of the Weddell Gyre circulation and hydrography improves with increased resolution, resulting in a stronger gyre, which can be attributed to a sharper ASF in HIGH and an associated stronger ASC. In LOW the slope current is vanishingly small. High resolution, at least in the order of the Rossby radius, is needed to maintain the ASF in the model. In HIGH, the interior gyre flow agrees with estimates based on the Sverdrup theory and accounts for about half of the total gyre strength (Total transport $\approx 40\,\mathrm{Sv}$). The second half is limited to the slope current. Both simulations show deficiencies in the eastern part of the gyre, where it interacts with the ACC and WDW is injected into the gyre. In LOW the eastern part of the gyre breaks down during the simulation and continuous upwelling across the Southwest Indian Ridge is found east of the prime meridian. While in HIGH some form of a gyre structure is maintained in the eastern part, the WDW layer above the continental slope is too fresh, which results in WDW being found at too shallow depth. This leads to a too strong warm flow onto the continental shelf. The properties of the water transported to the southern continental shelf within the slope current are determined by the processes at the eastern boundary. Neither of the simulations is suitable for a realistic analysis of the seasonal MWDW flow onto the southern Weddell Sea continental shelf. Despite a too strong warm inflow, HIGH reproduces key features on the

continental shelf: High salinities ($\mathcal{O}[34.85]$) on the western shelf and lower values in the Filchner Trough ($\mathcal{O}[34.6]$), strong northward flow ($\mathcal{O}[10\text{cm}\,\text{s}^{-1}]$) along the eastern slope of the Filchner Trough, representing the ISW outflow, major inflow paths of MWDW on the Eastern Shelf and via Hughes Trough (west of Berkner Bank).

3. By restoring the 3-D temperature and salinity field upstream of the Filchner Trough, to an, observation based, climatological hydrography of the ASF above the continental slope, a realistic inflow of MWDW is achieved, whose seasonal cycle is comparable to the presented mooring observations at 76°S. Model results suggest, that the moorings at 76° are located south of a small depression in the bathymetry ($\approx 450\,\text{m}$ depth), creating a small recirculation cell, that can explain the observed westward flow at M_{31W} and the time shift of the MWDW signal between $\text{M}_{30.5W}$ and M_{31W}, since the warm inflow steers around the depression. Due to data availability, only a restoring to summer conditions (shallow ASF depth) was possible, which at the same time served as a sensitivity experiment, to assess the importance of the processes on the continental shelf, such as winter convection, for the seasonal MWDW inflow. Although MWDW is present at the shelf break depth all year around, winter convection, which is strongest south of 76°S, impedes a year-long southward flow of MWDW. The MWDW that reaches Interannual variability of the modelled MWDW inflow is suggested to be driven by the overall density on the shelf. A positive density anomaly might weaken the warm inflow along the bottom, by lifting the MWDW core, however allows a broader inflow at mid-depth and could, therefore, lead to an overall stronger heat transport toward the south. A likely driver for the interannual variability of the shelf density in the model is the strength of sea ice production over the Ronne side, as well as, over the Berkner Bank and the southern Filchner Trough. The model results suggest, that under present day conditions, where the Filchner Trough is filled with dense ISW and the MWDW flow is limited to the Eastern Shelf that is shallower than 500 m, there is no direct pathway for MWDW to enter the FIS cavity, far beyond the ice shelf front, along the eastern side. This would only be possible if the thickness of the dense layer in the trough or its density was to decrease.

To conclude, the southern Weddell Sea is a highly complex region, which re-

mains undersampled due its remoteness and the presence of harsh conditions all year around. The lack of oceanic as well as atmospheric observations pose a big challenge to numerical models, in addition to the small Rossby radius governing the whole Weddell Gyre, requiring high resolution in order to resolve mesoscale activity. Observations show that the seasonal inflow of MWDW along the eastern flank of the Filchner Trough is strongly connected to the seasonality of the ASF. The properties of the water masses associated with the ASF, are likely set along the eastern boundary of the Weddell Gyre, suggesting that special care has to be taken of this region in ocean models. While the finite-element approach provides a great and promising opportunity for global ocean and climate models, by allowing a regional refinement of the mesh, the set-up has to be treated carefully with the consideration of large-scale circulation. However, the regional-restoring approach, developed in this thesis, might serve as a valuable tool for global ocean models, in order to improve the ocean circulation in the southern Weddell Sea locally. The main findings in this thesis give new insight to the general hydrography along the eastern flank of the Filchner Trough, by providing, for the first time, a full description of the seasonal hydrography. However, the results also demonstrate the great demands made on a global ocean model, for simulating cross-shelf exchanges in the Weddell Sea and ultimately, ocean-ice shelf interactions.

Based on the results of this thesis, several objectives for future work can be formulated. The mooring deployments at 76°S and the two *RV Polarstern* cruises (PS82, PS96) presented in this thesis, are part of a large project (Filchner Ice Shelf Project) of international collaboration, comprising two hot-water drilling campaigns on FIS to deploy under-shelf ice moorings (2015/2016 and 2016/2017), in total, three cruises with *RV Polarstern* (PS82, PS96 and PS111), besides additional efforts by international colleagues. The mooring time series presented here, is only the first part of a long-term time series (> 6 years) at 76°S. The moorings have been redeployed successfully during PS96 (2016) and again at the beginning of 2018, during PS111. Therefore, additional two-year long time series are available, which will be analysed in the near future and will give further insight into the, previously described, seasonal cycle. The moorings were equipped with additional temperature sensors during the first redeployment, allowing a better description of the temperature evolution throughout the water column. Furthermore, an extensive CTD-survey was possible during PS111, due to good sea ice

conditions, which includes data along the Ronne as well as Filchner ice shelf front, next to other valuable hydrographic data in the Filchner trough. Data from the under-shelf ice moorings is being transmitted via satellite and more than one year of data has been collected by now. Bringing this large set of observations together will be a challenging but exciting task and will provide new insight into the complex circulation on the southern Weddell Sea continental shelf.

Along with the data analysis, further development of FESOM simulations will be important. This thesis set a cornerstone for future modelling work in the Weddell Sea by highlighting deficiencies in the model regarding the ocean circulation, on which one can build on in future studies. One long-term goal should be to improve the representation of the Weddell Gyre, with focus on the ASF properties. The next step, however, is to apply the seasonal restoring, with the now available full data set, which will include the seasonal variability in the upper-layer hydrography over the continental slope. Many idealized modelling studies have suggested that a resolution in the order of 1 km is needed to fully resolve the dynamics of the ASF. Recently developed FESOM configurations in the Artic use such a high resolution regionally, however, this still requires exceptional computational effort. With exponentially increasing computer power, these high-resolution simulations might be more feasible in the near future.

A. Complementary Figures

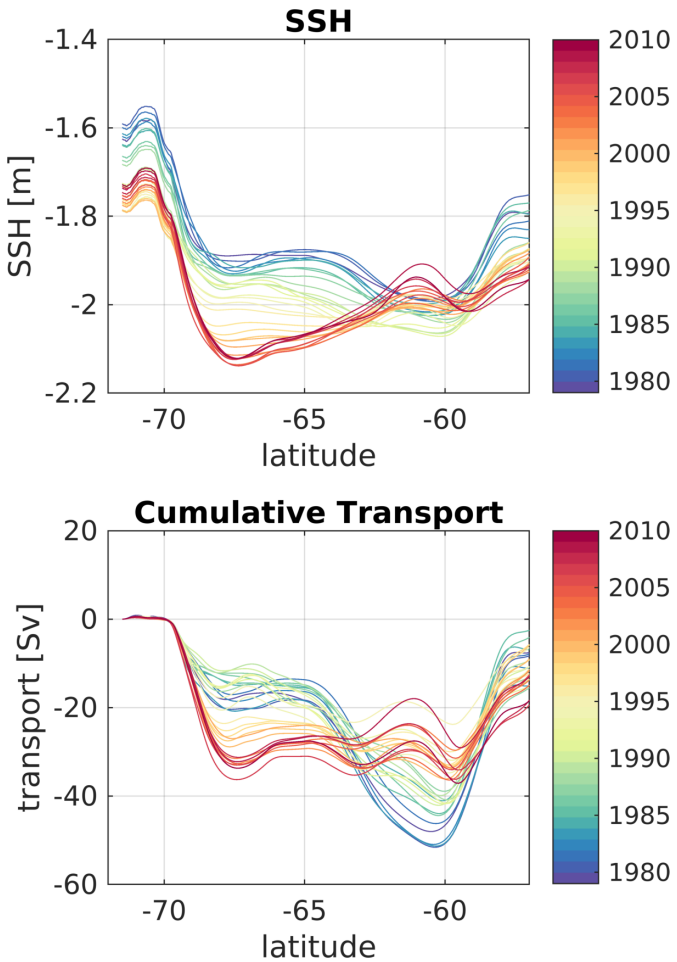

Figure A.1: Modelled annual mean SSH (top) and vertically integrated westward transports (bottom) along the prime meridian in HIGH. The comparison illustrated that the SSH field captures the structural changes of the Weddell Gyre throughout the model simulation.

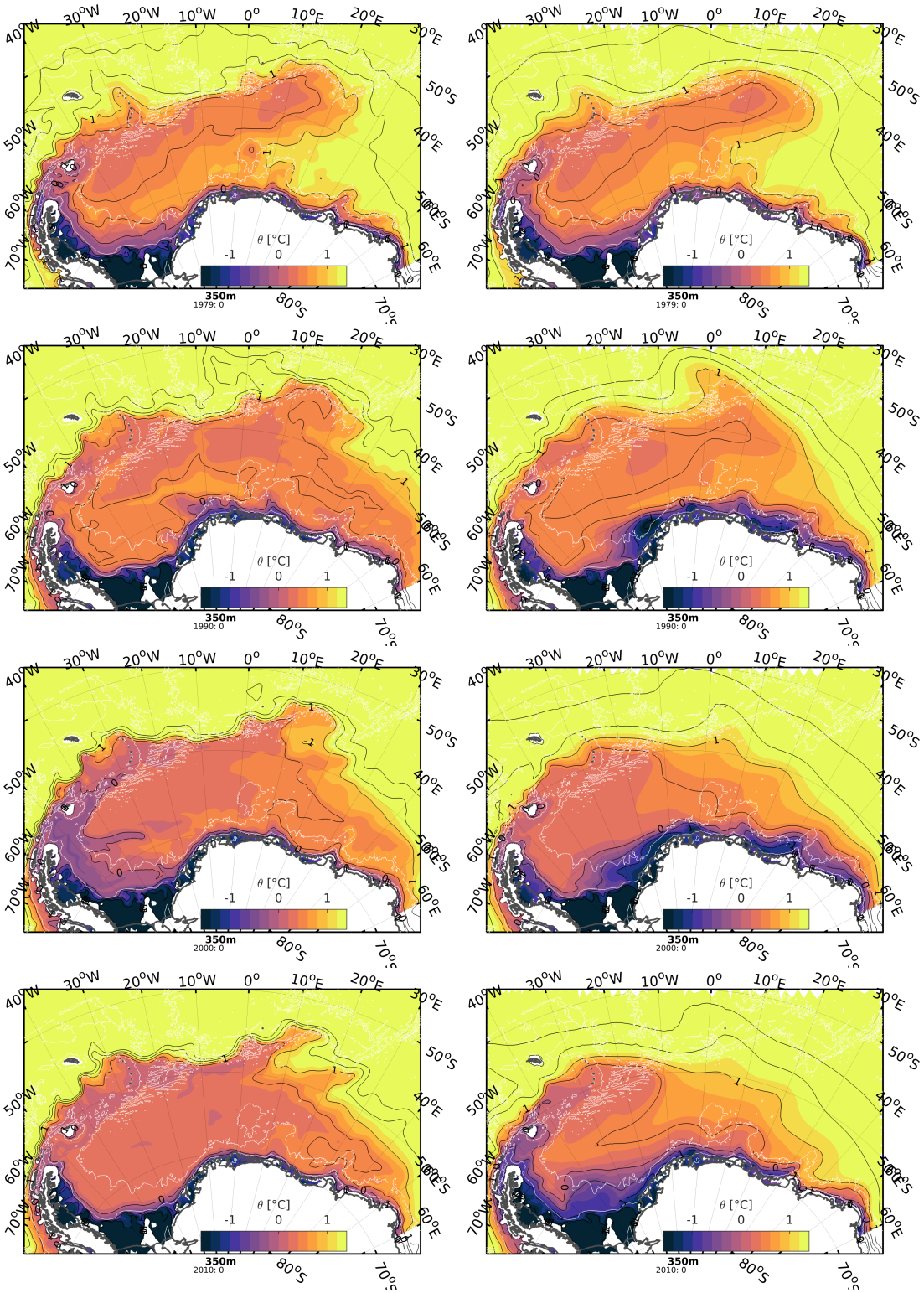

Figure A.2: Modelled potential temperature field at 350 m depth over the Weddell Gyre in 10-year intervals starting in 1979 (top) until 2010 (bottom) in run HIGH (left) and LOW (right). Black isolines represent isotherms in 1°C intervals. The temperature field illustrates the structural changes of the Weddell Gyre throughout the simulation.

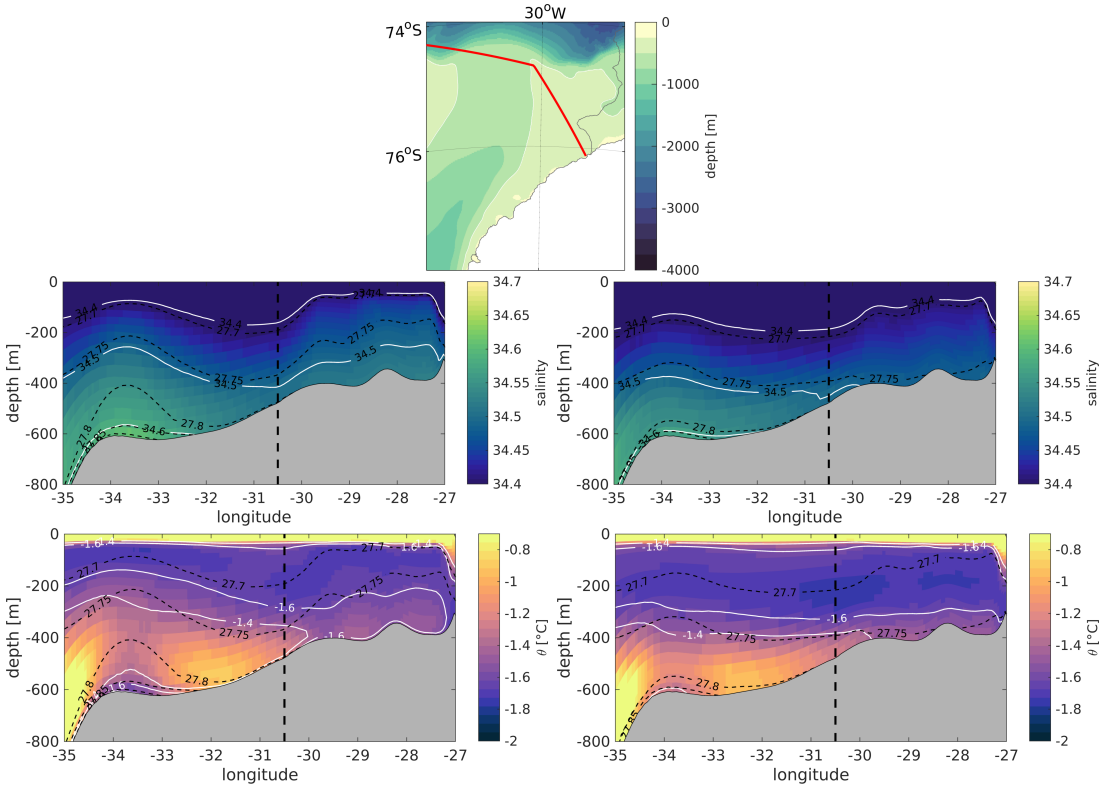

Figure A.3: Modelled temperature and salinity sections across the Eastern Shelf in HIGH average from 2000 to 2005 (left) and from 2006 to 2010 (right). The sections highlight the density differences on the continental shelf between both time periods.

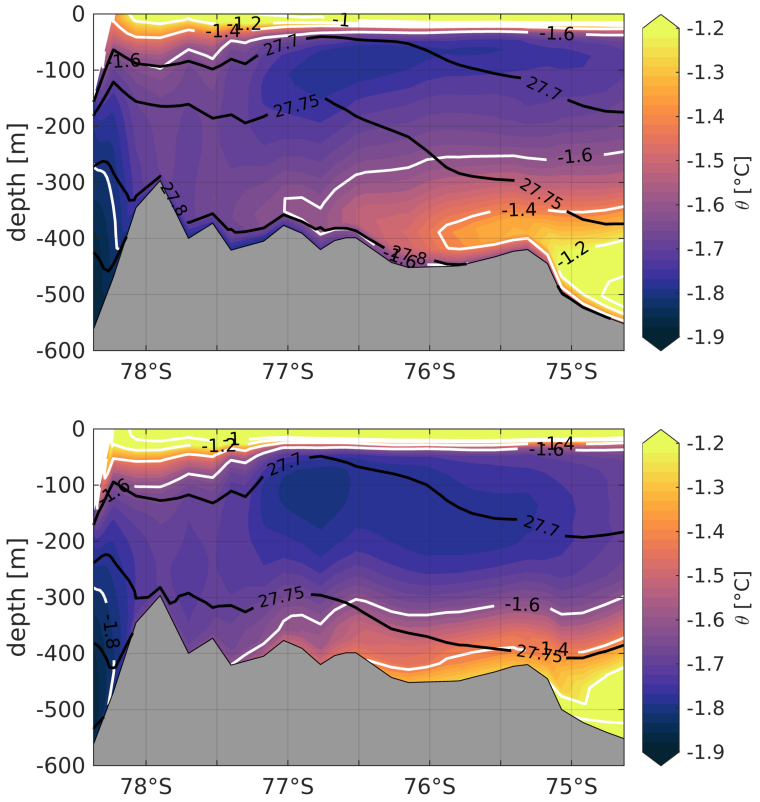

Figure A.4: Modelled potential temperature in HIGH, averaged over summer and autumn (Dec-May) between 2000-2005 (top) and 2006-2010 (bottom) along section InflowNS. White isolines represent temperature in 0.2°C intervals and black isolines represent potential density referenced to the surface in 0.05 $\mathrm{kg\,m^{-3}}$ intervals.

List of Figures

List of Tables

Bibliography

Andreas, E. L., T. W. Horst, A. A. Grachev, P. O. G. Persson, C. W. Fairall, P. S. Guest, and R. E. Jordan (2010), Parametrizing turbulent exchange over summer sea ice and the marginal ice zone, *Quarterly Journal of the Royal Meteorological Society*, *136*(649), 927–943, doi:10.1002/qj.618.

Aoki, S., S. R. Rintoul, S. Ushio, S. Watanabe, and N. L. Bindoff (2005), Freshening of the Adélie Land Bottom Water near 140E, *Geophysical Research Letters*, *32*(23), L23,601, doi:10.1029/2005GL024246.

Arakawa, A., and V. R. Lamb (1977), Computational Design of the Basic Dynamical Processes of the UCLA General Circulation Model, *Methods in Computational Physics: Advances in Research and Applications*, *17*, 173–265, doi:10.1016/B978-0-12-460817-7.50009-4.

Arneborg, L., A. K. Wåhlin, G. Björk, B. Liljebladh, and A. H. Orsi (2012), Persistent inflow of warm water onto the central Amundsen shelf, *Nature Geoscience*, *5*(12), 876–880, doi:10.1038/ngeo1644.

Årthun, M., K. W. Nicholls, K. Makinson, M. a. Fedak, and L. Boehme (2012), Seasonal inflow of warm water onto the southern Weddell Sea continental shelf, Antarctica, *Geophysical Research Letters*, *39*(17), 2–7, doi:10.1029/2012GL052856.

Årthun, M., K. W. Nicholls, and L. Boehme (2013), Wintertime Water Mass Modification near an Antarctic Ice Front, *Journal of Physical Oceanography*, *43*, 359–365, doi:10.1175/JPO-D-12-0186.1.

Beckmann, A., H. H. Hellmer, and R. Timmermann (1999), A numerical model of the Weddell Sea: Large-scale circulation and water mass distribution, *Journal of Geophysical Research*, *104*(C10), 23,375 – 23,391, doi:10.1029/1999JC900194.

Boehme, L., P. Lovell, M. Biuw, F. Roquet, J. Nicholson, S. E. Thorpe, M. P. Meredith, and M. Fedak (2009), Technical Note: Animal-borne CTD-Satellite Relay Data Loggers for real-time oceanographic data collection, *Ocean Science*, *5*(4), 685–695, doi:10.5194/os-5-685-2009.

Bornemann, H., M. N. Bester, P. J. N. De Bruyn, T. McIntyre, J. Plötz, M. Schröder, and C. A. Tosh (2015), Ocean temperature and salinity measured by CTD SRDLs deployed on Weddell seals at Atka Bay, Drescher Inlet and Filchner Trough with links to datasets, doi:10.1594/pangaea.150010.

Carmack, E. C., and T. D. Foster (1975), Circulation and distribution of oceanographic properties near the Filchner Ice Shelf, *Deep-Sea Research and Oceanographic Abstracts*, *22*(2), 77–90, doi:10.1016/0011-7471(75)90097-2.

Chelton, D. B., R. A. DeSzoeke, M. G. Schlax, K. El Naggar, N. Siwertz, D. B. Chelton, R. A. DeSzoeke, M. G. Schlax, K. E. Naggar, and N. Siwertz (1998), Geographical Variability of the First Baroclinic Rossby Radius of Deformation, *Journal of Physical Oceanography*, *28*(3), 433–460, doi:10.1175/1520-0485(1998)028⟨0433:GVOTFB⟩2.0.CO;2.

Church, J., P. Clark, A. Cazenave, J. Gregory, A. Jevrejava, A. Levermann, M. Merrifield, G. Milne, R. Nerem, P. Nunn, A. J. Payne, W. Pfeffer, D. Stammer, and A. Unnikrishnan (2013), 'Sea level change'. In: Climate Change 2013: The Physical Science Basis. Contribution of Working Group I to the Fifth Assessment Repoert of the Intergovernmental Panel in Climate Change.

Couldrey, M. P., L. Jullion, A. C. Naveira Garabato, C. Rye, L. Herráiz-Borreguero, P. J. Brown, M. P. Meredith, and K. L. Speer (2013), Remotely induced warming of Antarctic Bottom Water in the eastern Weddell gyre, *Geophysical Research Letters*, *40*(11), 2755–2760, doi:10.1002/grl.50526.

Daae, K., T. Hattermann, E. Darelius, and I. Fer (2017), On the effect of topography and wind on warm water inflowAn idealized study of the southern Weddell Sea continental shelf system, *Journal of Geophysical Research: Oceans*, pp. 2017–2033, doi:10.1002/2013JC009262.Received.

Danilov, S., and Q. Wang (2015), Resolving eddies by local mesh refinement, *Ocean Modelling*, *93*, 75–83, doi:10.1016/j.ocemod.2015.07.006.

Danilov, S., G. Kivman, and J. Schröter (2004), A finite-element ocean model: Principles and evaluation, *Ocean Modelling*, *6*(2), 125–150, doi:10.1016/S1463-5003(02)00063-X.

Darelius, E., and I. Fer (2015), Physical oceanography from CTD in the Filchner Depression (Weddell Sea, Antarctica) during Ernest Shackleton cruise ES060, doi:10.1594/PANGAEA.846962.

Darelius, E., and I. Fer (2017), Physical oceanography from mooring SB, SC, SD and SE in the Weddell Sea, doi:10.1594/PANGAEA.870518.

Darelius, E., and J. B. Sallée (2018), Seasonal Outflow of Ice Shelf Water Across the Front of the Filchner Ice Shelf, Weddell Sea, Antarctica, *Geophysical Research Letters*, *45*(8), 3577–3585, doi:10.1002/2017GL076320.

Darelius, E., K. Makinson, K. Daae, I. Fer, P. R. Holland, and K. W. Nicholls (2014a), Hydrography and circulation in the Filchner Depression, Weddell Sea, Antarctica, *Journal of Geophysical Research: Oceans*, *119*(9), 5797–5814, doi:10.1002/2014JC010225.

Darelius, E., K. O. Strand, S. Østerhus, T. Gammelsrød, M. Årthun, and I. Fer (2014b), On the Seasonal Signal of the Filchner Overflow, Weddell Sea, Antarctica, *Journal of Physical Oceanography*, *44*(4), 1230–1243, doi:10.1175/JPO-D-13-0180.1.

Darelius, E., K. Makinson, K. Daae, I. Fer, P. R. Holland, and K. W. Nicholls (2014c), Hydrography and circulation in the Filchner Depression, Weddell Sea, Antarctica, *Journal of Geophysical Research: Oceans*, pp. n/a–n/a, doi:10.1002/2014JC010225.

Darelius, E., I. Fer, and K. W. Nicholls (2016), Observed vulnerability of Filchner-Ronne Ice Shelf to wind-driven inflow of warm deep water, *Nature Communications*, *7:12300*, doi:10.1038/ncomms12300.

Darelius, E., S. Ryan, S. Østerhus, and I. Fer (2017), Hydrography and circulation in the Filchner Depression, Weddell Sea, Antarctica from one year of moored measurements, *Journal of Geophysical Research, submitted*.

Dupont, T. K., and R. B. Alley (2005), Assessment of the importance of ice-shelf buttressing to ice-sheet flow, *Geophysical Research Letters*, *32*(4), L04,503, doi:10.1029/2004GL022024.

Dutrieux, P., J. De Rydt, A. Jenkins, P. R. Holland, H. K. Ha, S. H. Lee, E. J. Steig, Q. Ding, E. P. Abrahamsen, and M. Schröder (2014), Strong Sensitivity of Pine Island Ice-Shelf, *Science*, *174*(January), 174–179, doi:10.1126/science.1244341.

Emery, W. J., and R. E. Thomson (2001), *Data Analysis Methods in Physical Oceanography*, 2nd editio ed., Elsevier B.V., Amsterdam.

Fahrbach, E., G. Rohardt, M. Schröder, and V. Strass (1994), Transport and structure of the Weddell Gyre, *Annales Geophysicae*, *12*, 840–855.

Fahrbach, E., G. Rohardt, N. Scheele, M. Schröder, V. Strass, and A. Wisotzki (1995), Formation and discharge of deep and bottom water in the northwestern Weddell Sea, *Journal of Marine Research*, *53*(4), 515–538, doi:10.1357/0022240953213089.

Fer, I. (2016), Temperature and salinity measurements in the southern Weddell Sea at mooring site M3, doi:10.1594/PANGAEA.869784.

Ferrigno, J. G., and W. G. Gould (1987), Substantial changes in the coastline of Antarctica revealed by satellite imagery, *Polar Record*, *23*(146), 577, doi:10.1017/S003224740000807X.

Foldvik, A. (2004), Ice shelf water overflow and bottom water formation in the southern Weddell Sea, *Journal of Geophysical Research*, *109*(C2), C02,015, doi:10.1029/2003JC002008.

Foldvik, A., and T. Gammelsrød (1988), Notes on Southern Ocean hydrography, sea-ice and bottom water formation, *Palaeogeography, Palaeoclimatology, Palaeoecology*, *67*(1), 3–17, doi:10.1016/0031-0182(88)90119-8.

Foldvik, A., T. Gammelsrød, and T. Tørresen (1985a), Hydrographic observations from the Weddell Sea during the Norwegian Antarctic Research Expedition 1976/77, *Polar Research*, *3*(2), 177–193, doi:10.1111/j.1751-8369.1985.tb00506.x.

Foldvik, A., T. Gammelsrød, and T. Tørresen (1985b), Circulation and water masses on the southern Weddell Sea shelf, in *Oceanology of the Antarctic Continental Shelf*, edited by S. Jacobs, pp. 5–20, American Geophysical Union, Washington, D.C., doi:10.1029/AR043p0005.

Foldvik, A., T. Gammelsrød, E. Nygaard, and S. Østerhus (2001), Current measurements near Ronne Ice Shelf: Implications for circulation and melting, *Journal of Geophysical Research*, *106*(C3), 4463–4477, doi:10.1029/2000JC000217.

Foster, T. D., and E. C. Carmack (1976), Frontal zone mixing and Antarctic Bottom water formation in the southern Weddell Sea, *Deep Sea Research and Oceanographic Abstracts*, *23*(March 1975), 301–317, doi:10.1016/0011-7471(76)90872-X.

Fox, A. J., A. Paul, and R. Cooper (1994), Measured properties of the Antarctic ice sheet derived from the SCAR Antarctic digital database, *Polar Record*, *30*(174), 201, doi:10.1017/S0032247400024268.

Fretwell, P., H. D. Pritchard, D. G. Vaughan, J. L. Bamber, N. E. Barrand, R. Bell, C. Bianchi, R. G. Bingham, D. D. Blankenship, G. Casassa, G. Catania, D. Callens, H. Conway, A. J. Cook, H. F. J. Corr, D. Damaske, V. Damm, F. Ferraccioli, R. Forsberg, S. Fujita, Y. Gim, P. Gogineni, J. A. Griggs, R. C. A. Hindmarsh, P. Holmlund, J. W. Holt, R. W. Jacobel, A. Jenkins, W. Jokat, T. Jordan, E. C. King, J. Kohler, W. Krabill, M. Riger-Kusk, K. A. Langley, G. Leitchenkov, C. Leuschen, B. P. Luyendyk, K. Matsuoka, J. Mouginot, F. O. Nitsche, Y. Nogi, O. A. Nost, S. V. Popov, E. Rignot, D. M. Rippin, A. Rivera, J. Roberts, N. Ross, M. J. Siegert, A. M. Smith, D. Steinhage, M. Studinger, B. Sun, B. K. Tinto, B. C. Welch, D. Wilson, D. A. Young, C. Xiangbin, and A. Zirizzotti (2013), Bedmap2: improved ice bed, surface and thickness datasets for Antarctica, *The Cryosphere*, *7*(1), 375–393, doi:10.5194/tc-7-375-2013.

Gade, H. G. (1979), Melting of Ice in Sea Water: A Primitive Model with Application to the Antarctic Ice Shelf and Icebergs, *Journal of Physical Oceanography*, *9*, 189–198, doi:http://dx.doi.org/10.1175/1520-0485(1979)009⟨0189:MOIISW⟩2.0.CO;2.

Gammelsrød, T., A. Foldvik, O. A. Nøst, Ø. Foldvik, L. G. Anderson, E. Fogelqvist, K. Olsson, T. Tanhua, E. P. Jones, and S. Østerhus (1994), Distribution of water masses on the continental shelf in the southern Weddell Sea,

in *Geophysical Monograph Series*, pp. 159–176, American Geophysical Union, doi:10.1029/GM085p0159.

Gill, A. E. (1973), Circulation and bottom water production in the Weddell Sea, *Deep-Sea Research and Oceanographic Abstracts*, *20*(2), 111–140, doi:10.1016/0011-7471(73)90048-X.

Gille, S. T. (1994), Mean sea surface height of the Antarctic Circumpolar Current from Geosat data: Method and application, *Journal of Geophysical Research*, *99*(C9), 18,255, doi:10.1029/94JC01172.

Golledge, N. R., R. H. Levy, R. M. McKay, and T. R. Naish (2017), East Antarctic ice sheet most vulnerable to Weddell Sea warming, *Geophysical Research Letters*, *44*(5), 2343–2351, doi:10.1002/2016GL072422.

Gordon, A. L., and B. A. Huber (1984), Thermohaline stratification below the Southern Ocean sea ice, *Journal of Geophysical Research*, *89*(C1), 641, doi:10.1029/JC089iC01p00641.

Gordon, A. L., M. Visbeck, and B. Huber (2001), Export of Weddell Sea deep and bottom water, *Journal of Geophysical Research: Oceans*, *106*(C5), 9005–9017, doi:10.1029/2000JC000281.

Gordon, A. L., B. Huber, D. McKee, and M. Visbeck (2010), A seasonal cycle in the export of bottom water from the Weddell Sea, *Nature Geoscience*, *3*(8), 551–556, doi:10.1038/ngeo916.

Gouretski, V. V., and A. I. Danilov (1993), Weddell Gyre: structure of the eastern boundary, *Deep Sea Research Part I: Oceanographic Research Papers*, *40*(3), 561–582.

Graham, J. A., K. J. Heywood, C. P. Chavanne, and P. R. Holland (2013), Seasonal variability of water masses and transport on the Antarctic continental shelf and slope in the southeastern Weddell Sea, *Journal of Geophysical Research: Oceans*, *118*(4), 2201–2214, doi:10.1002/jgrc.20174.

Grosfeld, K., M. Schröder, E. Fahrbach, R. Gerdes, and A. Mackensen (2001), How iceberg calving and grounding change the circulation and hydrography in the Filchner Ice Shelf-Ocean System, *Journal of Geophysical Research*, *106*(C5), 9039, doi:10.1029/2000JC000601.

Hattermann, T. (2018), On the Thermocline Depth at the Weddell Sea Continental Slope, *Journal of Physical Oceanography*, *under revi*.

Hattermann, T., L. Smedsrud, O. Nøst, J. Lilly, and B. Galton-Fenzi (2014), Eddy-resolving simulations of the Fimbul Ice Shelf cavity circulation: Basal melting and exchange with open ocean, *Ocean Modelling*, *82*, 28–44, doi:10.1016/j.ocemod.2014.07.004.

Hellmer, H. H., and D. Olbers (1989), A two-dimensional model for the thermohaline circulation under an ice shelf, *Antarctic Science*, *1*(4), 325–336.

Hellmer, H. H., F. Kauker, R. Timmermann, J. Determann, and J. Rae (2012), Twenty-first-century warming of a large Antarctic ice-shelf cavity by a redirected coastal current, *Nature*, *485*, 5–8, doi:10.1038/nature11064.

Hellmer, H. H., F. Kauker, R. Timmermann, and T. Hattermann (2017), The fate of the Southern Weddell Sea Continental Shelf in a Warming Climate, *Journal of Climate*, *30*(12), 4337–4350, doi:10.1175/JCLI-D-16-0420.1.

Heywood, K. J., R. a. Locarnini, R. D. Frew, P. F. Dennis, and B. a. King (1998), TRANSPORT AND WATER MASSES OF THE ANTARCTIC SLOPE FRONT SYSTEM IN THE EASTERN WEDDELL SEA We present observations of the Antarctic Slope Front and the water masses of the continental shelf and slope in the eastern Weddell Sea near 17 W , obtained during, *75*, 203–214.

Heywood, K. J., A. C. Naveira Garabato, D. P. Stevens, and R. D. Muench (2004), On the fate of the Antarctic Slope Front and the origin of the Weddell Front, *Journal of Geophysical Research C: Oceans*, *109*(6), 1–13, doi:10.1029/2003JC002053.

Huhn, O., H. H. Hellmer, M. Rhein, C. Rodehacke, W. Roether, M. P. Schodlok, and M. Schröder (2008), Evidence of deep- and bottom-water formation in the western Weddell Sea, *Deep-Sea Research Part II: Topical Studies in Oceanography*, *55*(8-9), 1098–1116, doi:10.1016/j.dsr2.2007.12.015.

Jackett, D. R., and T. J. Mcdougall (1995), Minimal Adjustment of Hydrographic Profiles to Achieve Static Stability, *Journal of Atmospheric and Oceanic Technology*, *12*(2), 381–389, doi:10.1175/1520-0426(1995)012⟨0381:MAOHPT⟩2.0.CO;2.

Jacobs, S., C. Giulivi, P. Dutrieux, E. Rignot, F. Nitsche, and J. Mouginot (2013), Getz Ice Shelf melting response to changes in ocean forcing, *Journal of Geophysical Research: Oceans*, *118*(9), 4152–4168, doi:10.1002/jgrc.20298.

Jacobs, S. S. (1991), On the nature and significance of the Antarctic Slope Front, *Marine Chemistry*, *35*(1-4), 9–24, doi:10.1016/S0304-4203(09)90005-6.

Jacobs, S. S., and J. C. Comiso (1989), Sea ice and oceanic processes on the Ross Sea continental shelf, *Journal of Geophysical Research*, *94*(C12), 18,195, doi:10.1029/JC094iC12p18195.

Jacobs, S. S., C. F. Giulivi, and P. A. Mele (2002), Freshening of the Ross Sea during the late 20th century., *Science*, *297*(5580), 386–9, doi:10.1126/science.1069574.

Jacobs, S. S., C. F. Giulivi, S. S. Jacobs, and C. F. Giulivi (2010), Large Multidecadal Salinity Trends near the PacificAntarctic Continental Margin, *Journal of Climate*, *23*(17), 4508–4524, doi:10.1175/2010JCLI3284.1.

Jacobs, S. S., A. Jenkins, C. F. Giulivi, and P. Dutrieux (2011), Stronger ocean circulation and increased melting under Pine Island Glacier ice shelf, *Nature Geoscience*, *4*(8), 519–523, doi:10.1038/ngeo1188.

Jensen, M. F., I. Fer, and E. Darelius (2013), Low frequency variability on the continental slope of the southern Weddell Sea, *Journal of Geophysical Research: Oceans*, *118*(9), 4256–4272, doi:10.1002/jgrc.20309.

Joughin, I. (2003), Melting and freezing beneath Filchner-Ronne Ice Shelf, Antarctica, *Geophysical Research Letters*, *30*(9), 1477, doi:10.1029/2003GL016941.

Jullion, L., S. Jones, A. Naveira Garabato, and M. P. Meredith (2010), Wind-controlled export of Antarctic Bottom Water from the Weddell Sea, *Geophysical Research Letters*, *37*(9), L09,609, doi:10.1029/2010GL042822.

Jullion, L., A. C. Naveira Garabato, S. Bacon, M. P. Meredith, P. J. Brown, S. Torres-Vald\{e}s, K. G. Speer, P. R. Holland, J. Dong, D. Bakker, M. Hoppema, B. Loose, H. J. Venables, W. j. Jenkins, M.-J. Messias, and E. Fahrbach (2014), The contribution of the Weddell Gyre to the lower limb of the Global Overturning Circulation, *Journal of Geophysical Research: Oceans*, *119*(6), 3357–3377, doi:10.1002/2013JC009725.Received.

Kida, S. (2011), The Impact of Open Oceanic Processes on the Antarctic Bottom Water Outflows, *Journal of Physical Oceanography*, *41*(10), 1941–1957, doi: 10.1175/2011JPO4571.1.

Klatt, O., E. Fahrbach, M. Hoppema, and G. Rohardt (2005), The transport of the Weddell Gyre across the Prime Meridian, *Deep-Sea Research Part II: Topical Studies in Oceanography*, *52*(3-4), 513–528, doi:10.1016/j.dsr2.2004.12.015.

Klinck, J. M., and M. S. Dinniman (2010), Exchange across the shelf break at high southern latitudes, *Ocean Science*, *6*(2), 513–524, doi:10.5194/os-6-513-2010.

Knust, R., and M. Schröder (2014), The Expedition PS82 of the Research Vessel POLARSTERN to the southern Weddell Sea in 2013/2014, *Reports on Polar and Marine Research*, *680*, 1–155, doi:10.2312/BzPM_0680_2014.

Lambrecht, A., H. Sandhäger, D. Vaughan, and C. Mayer (2007), New ice thickness maps of Filchner\Ronne Ice Shelf, Antarctica, with specific focus on grounding lines and marine ice, *Antarctic Science*, *19*(04), 521–532, doi: 10.1017/S0954102007000661.

Lemarié, F., J. Kurian, A. F. Shchepetkin, M. Jeroen Molemaker, F. Colas, and J. C. McWilliams (2012), Are there inescapable issues prohibiting the use of terrain-following coordinates in climate models?, *Ocean Modelling*, *42*, 57–79, doi:10.1016/J.OCEMOD.2011.11.007.

Locarnini, R. A., A. V. Mishonov, J. I. Antonov, T. P. Boyer, H. E. Garcia, O. K. Baranova, M. M. Zweng, C. R. Paver, J. R. Reagan, D. R. Johnson, M. Hamilton, and D. Seidov (2013), World Ocean Atlas 2013, Volume 1: Temperature, in *NOAA Atlas NESDIS 73*, edited by S. E. Levitus and A. t. E. Mishonov, p. 40 pp.

Madec, G., P. Delecluse, M. Crepon, M. Chartier, G. Madec, P. Delecluse, M. Crepon, and M. Chartier (1991), A Three-Dimensional Numerical Study of Deep-Water Formation in the Northwestern Mediterranean Sea, *Journal of Physical Oceanography*, *21*(9), 1349–1371, doi:10.1175/1520-0485(1991)021⟨1349:ATDNSO⟩2.0.CO;2.

Makinson, K., P. R. Holland, A. Jenkins, K. W. Nicholls, and D. M. Holland (2011), Influence of tides on melting and freezing beneath Filchner-

Ronne Ice Shelf, Antarctica, *Geophysical Research Letters*, *38*(6), 4–9, doi: 10.1029/2010GL046462.

Mantyla, A. W., and J. L. Reid (1983), Abyssal characteristics of the World Ocean waters, *Deep Sea Research Part A. Oceanographic Research Papers*, *30*(8), 805–833, doi:10.1016/0198-0149(83)90002-X.

Marshall, J., and K. Speer (2012), Closure of the meridional overturning circulation through Southern Ocean upwelling, *Nature Geoscience*, *5*(3), 171–180, doi:10.1038/ngeo1391.

Martinson, D. G., and R. A. Iannuzzi (1998), Antarctic ocean-ice interaction: implications from ocean bulk property distributions in the Weddell Sea, in *Antarctic Research Series*, vol. 74, edited by M. Jeffries, chap. Antarctic, pp. 243–271, AGU, Washington, D.C.

Mashayek, A., H. Salehipour, D. Bouffard, C. P. Caulfield, R. Ferrari, M. Nikurashin, W. R. Peltier, and W. D. Smyth (2017), Efficiency of turbulent mixing in the abyssal ocean circulation, *Geophysical Research Letters*, *44*(12), 6296–6306, doi:10.1002/2016GL072452.

Mathiot, P., H. Goosse, T. Fichefet, B. Barnier, and H. Gallée (2011), Modelling the seasonal variability of the Antarctic Slope Current, *Ocean Science*, *7*(4), 455–470, doi:10.5194/os-7-455-2011.

Meredith, M. P. (2013), Oceanography: Replenishing the abyss, *Nature Geoscience*, *6*(3), 166–167, doi:10.1038/ngeo1743.

Moffat, C., B. Owens, and R. C. Beardsley (2009), On the characteristics of Circumpolar Deep Water intrusions to the west Antarctic Peninsula Continental Shelf, *Journal of Geophysical Research*, *114*(C5), C05,017, doi:10.1029/2008JC004955.

Nakayama, Y., M. Schröder, and H. H. Hellmer (2013), From circumpolar deep water to the glacial meltwater plume on the eastern Amundsen Shelf, *Deep-Sea Research Part I: Oceanographic Research Papers*, *77*, 50–62, doi:10.1016/j.dsr.2013.04.001.

Nakayama, Y., R. Timmermann, C. B. Rodehacke, M. Schröder, and H. H. Hellmer (2014), Modeling the spreading of glacial meltwater from the Amundsen and Bellingshausen Seas, *Geophysical Research Letters*, *41*(22), 7942–7949, doi:10.1002/2014GL061600.

Naughten, K. A., K. J. Meissner, B. K. Galton-Fenzi, M. H. England, R. Timmermann, H. H. Hellmer, T. Hattermann, and J. B. Debernard (2018), Intercomparison of Antarctic ice-shelf, ocean, and sea-ice interactions simulated by MetROMS-iceshelf and FESOM 1.4, *Geoscientific Model Development*, *11*(4), 1257–1292, doi:10.5194/gmd-11-1257-2018.

Naveira Garabato, A. C., K. J. Heywood, and D. P. Stevens (2002), Modification and pathways of Southern Ocean Deep Waters in the Scotia Sea, *Deep-Sea Research Part I: Oceanographic Research Papers*, *49*(4), 681–705, doi:10.1016/S0967-0637(01)00071-1.

Nicholls, K., S. Østerhus, K. Makinson, and M. Johnson (2001), Oceanographic conditions south of Berkner Island, beneath Filchner-Ronne Ice Shelf, Antarctica, *106*(Figure 1), doi:10.1029/2000JC000350.

Nicholls, K., L. Padman, M. Schröder, R. Woodgate, A. Jenkins, and S. Østerhus (2003), Water mass modification over the continental shelf north of Ronne Ice Shelf, Antarctica, *Journal of Geophysical Research*, *108*(C8,3260), 15pp, doi:10.1029/2002JC001713.

Nicholls, K. W. (2005), JR097 Cruise Report: Autosub Under Ice Cruise to the southern Weddell Sea, RRS James Clark Ross, Br. Antarct. Surv., Cambridge, U.K. [Available at https://www.bodc.ac.uk/resources/inventories/cruise_inventory/reports/jr97_05.pdf].

Nicholls, K. W., S. Østerhus, K. Makinson, T. Gammelsrød, and E. Fahrbach (2009), Ice-ocean processes over the continental shelf of the Southern Weddell Sea, Antarctica: A review, *Reviews of Geophysics*, *47*(3), 1–23, doi:10.1029/2007RG000250.

Nøst, O., and S. Østerhus (1998), Impact of grounded icebergs on the hydrographic conditions near the Filchner Ice Shelf, *Ocean, Ice and Atmosphere: Interactions at the Antarctic Continental Margin*, *75*, 267–284, doi:10.1029/AR075p0267.

Nøst, O. A., M. Biuw, V. Tverberg, C. Lydersen, T. Hattermann, Q. Zhou, L. H. Smedsrud, and K. M. Kovacs (2011), Eddy overturning of the Antarctic Slope Front controls glacial melting in the Eastern Weddell Sea, *Journal of Geophysical Research: Oceans*, *116*(11), 1–17, doi:10.1029/2011JC006965.

Núñez-Riboni, I., and E. Fahrbach (2009), Seasonal variability of the Antarctic Coastal Current and its driving mechanisms in the Weddell Sea, *Deep-Sea Research Part I: Oceanographic Research Papers*, *56*(11), 1927–1941, doi:10.1016/j.dsr.2009.06.005.

Orsi, A. H., W. D. Nowlin, and T. Whitworth III (1993), On the circulation and stratification of the Weddell Gyre, *Deep-Sea Research Part I: Oceanographic Research Papers*, *40*(1), 169–203, doi:10.1016/0967-0637(93)90060-G.

Orsi, A. H., T. Whitworth, and W. D. Nowlin (1995), On the meridional extent and fronts of the Antarctic Circumpolar Current, *Deep Sea Research Part I: Oceanographic Research Papers*, *42*(5), 641–673, doi:10.1016/0967-0637(95)00021-W.

Orsi, a. H., G. C. Johnson, and J. L. Bullister (1999), Circulation, mixing, and production of Antarctic Bottom Water, *Progress in Oceanography*, *43*(1), 55–109, doi:10.1016/S0079-6611(99)00004-X.

Orsi, A. H., S. S. Jacobs, A. L. Gordon, and M. Visbeck (2001), Cooling and ventilating the Abyssal Ocean, *Geophysical Research Letters*, *28*(15), 2923–2926, doi:10.1029/2001GL012830.

Paolo, F. S., H. A. Fricker, and L. Padman (2015), Volume loss from Antarctic ice shelves is accelerating, *Science*, *348*(6232), 327–332, doi:10.1126/science.aaa0940.

Park, Y.-H., E. Charriaud, P. Craneguy, and A. Kartavtseff (2001), Fronts, transport, and Weddell Gyre at 30E between Africa and Antarctica, *Journal of Geophysical Research*, *106*(C2), 2857, doi:10.1029/2000JC900087.

Parkinson, C. L., and D. J. Cavalieri (2012), Antarctic sea ice variability and trends, 19792010, *The Cryosphere*, *6*, 871–880, doi:10.5194/tc-6-871-2012.

Parkinson, C. L., and W. M. Washington (1979), A large-scale numerical model of sea ice, *Journal of Geophysical Research*, *84*(C1), 311, doi:10.1029/JC084iC01p00311.

Petty, A. A., D. L. Feltham, and P. R. Holland (2013), Impact of Atmospheric Forcing on Antarctic Continental Shelf Water Masses, *Journal of Physical Oceanography*, *43*(5), 920–940, doi:10.1175/JPO-D-12-0172.1.

Petty, A. A., P. R. Holland, and D. L. Feltham (2014), Sea ice and the ocean mixed layer over the Antarctic shelf seas, *Cryosphere*, *8*(2), 761–783, doi:10.5194/tc-8-761-2014.

Preisendorfer, R. W. (1988), *Principal Component Analysis in Metorology and Oceanography*, Elsevier B.V., Amsterdam.

Pritchard, H. D., S. R. M. Ligtenberg, H. A. Fricker, D. G. Vaughan, M. R. V. D. Broeke, and L. Padman (2012), Antarctic ice-sheet loss driven by basal melting of ice shelves, *Nature*, *484*(7395), 502–505, doi:10.1038/nature10968.

Purkey, S. G., and G. C. Johnson (2010), Warming of global abyssal and deep Southern Ocean waters between the 1990s and 2000s: Contributions to global heat and sea level rise budgets, *Journal of Climate*, *23*(23), 6336–6351, doi:10.1175/2010JCLI3682.1.

Rignot, E., J. L. Bamber, M. R. van den Broeke, C. Davis, Y. Li, W. J. van de Berg, and E. van Meijgaard (2008), Recent Antarctic ice mass loss from radarinterferometry and regional climatemodelling, *Nature Geoscience*, *1*(2), 106–110, doi:10.1038/ngeo102.

Rignot, E., I. Velicogna, M. R. van den Broeke, A. Monaghan, and J. T. M. Lenaerts (2011), Acceleration of the contribution of the Greenland and Antarctic ice sheets to sea level rise, *Geophysical Research Letters*, *38*(5), L05,503, doi:10.1029/2011GL046583.

Rignot, E., S. Jacobs, J. Mouginot, and B. Scheuchl (2013), Ice-Shelf Melting Around Antarctica, *Science*, *341*(6143), 266–270, doi:10.1126/science.1235798.

Rind, D., M. Chandler, J. Lerner, D. G. Martinson, and X. Yuan (2001), Climate response to basin-specific changes in latitudinal temperature gradients and im-

plications for sea ice variability, *Journal of Geophysical Research: Atmospheres*, *106*(D17), 20,161–20,173, doi:10.1029/2000JD900643.

Rintoul, S. R. (2007), Rapid freshening of Antarctic Bottom Water formed in the Indian and Pacific oceans, *Geophysical Research Letters*, *34*(6), L06,606, doi:10.1029/2006GL028550.

Ryan, S., M. Schröder, O. Huhn, and R. Timmermann (2016), On the warm inflow at the eastern boundary of the Weddell Gyre, *Deep-Sea Research Part I: Oceanographic Research Papers*, *107*, 70–81, doi:10.1016/j.dsr.2015.11.002.

Ryan, S., T. Hattermann, E. Darelius, and M. Schröder (2017), Seasonal cycle of hydrography on the eastern shelf of the Filchner Trough, Weddell Sea, Antarctica, *Journal of Geophysical Research: Oceans*, *122*, 6437–6453, doi:10.1002/2017JC012916.

Rye, C. D., A. C. Naveira Garabato, P. R. Holland, M. P. Meredith, A. J. George Nurser, C. W. Hughes, A. C. Coward, and D. J. Webb (2014), Rapid sea-level rise along the Antarctic margins inresponse to increased glacial discharge, *Nature Geoscience*, *7*(10), 732–735, doi:10.1038/ngeo2230.

Saha, S., S. Moorthi, H. L. Pan, X. Wu, J. Wang, S. Nadiga, P. Tripp, R. Kistler, J. Woollen, D. Behringer, H. Liu, D. Stokes, R. Grumbine, G. Gayno, J. Wang, Y. T. Hou, H. Y. Chuang, H. M. H. Juang, J. Sela, M. Iredell, R. Treadon, D. Kleist, P. Van Delst, D. Keyser, J. Derber, M. Ek, J. Meng, H. Wei, R. Yang, S. Lord, H. Van Den Dool, A. Kumar, W. Wang, C. Long, M. Chelliah, Y. Xue, B. Huang, J. K. Schemm, W. Ebisuzaki, R. Lin, P. Xie, M. Chen, S. Zhou, W. Higgins, C. Z. Zou, Q. Liu, Y. Chen, Y. Han, L. Cucurull, R. W. Reynolds, G. Rutledge, and M. Goldberg (2010), The NCEP climate forecast system reanalysis, *Bulletin of the American Meteorological Society*, *91*(8), 1015–1057, doi:10.1175/2010BAMS3001.1.

Schaffer, J., R. Timmermann, J. E. Arndt, S. S. Kristensen, C. Mayer, M. Morlighem, and D. Steinhage (2016), A global, high-resolution data set of ice sheet topography, cavity geometry, and ocean bathymetry., *Earth System Science Data*, *8*(2), 543–557, doi:10.5194/essd-8-543-2016.

Schmidtko, S., K. J. Heywood, A. F. Thompson, and S. Aoki (2014), Mul-

tidecadal warming of Antarctic waters, *Science*, *346*(6214), 1227–1231, doi:10.1126/science.1256117.

Schodlok, M. P., H. H. Hellmer, and A. Beckmann (2002), On the transport, variability and origin of dense water masses crossing the South Scotia Ridge, *Deep Sea Research Part II: Topical Studies in Oceanography*, *49*(21), 4807–4825, doi:10.1016/S0967-0645(02)00160-1.

Schröder, M. (2016), The expedition PS96 of the research vessel POLARSTERN to the southern Weddell Sea in 2015/2016, *Reports on Polar and Marine Research*, *700*, 1–142, doi:10.2312/BzPM_0700_2016.

Schröder, M., and E. Fahrbach (1999), On the structure and the transport of the eastern Weddell Gyre, *Deep-Sea Research Part II: Topical Studies in Oceanography*, *46*(1-2), 501–527, doi:10.1016/S0967-0645(98)00112-X.

Schröder, M., S. Ryan, and A. Wisotzki (2014a), Physical oceanography and current meter data from mooring AWI254-1.

Schröder, M., S. Ryan, and A. Wisotzki (2014b), Physical oceanography and current meter data from mooring AWI253-1.

Schröder, M., S. Ryan, and A. Wisotzki (2014c), Physical oceanography and current meter data from mooring AWI252-1.

Srivastava, R., R. Ramesh, S. Prakash, N. Anilkumar, and M. Sudhakar (2007), Oxygen isotope and salinity variations in the Indian sector of the Southern Ocean, *Geophysical Research Letters*, *34*(24), L24,603, doi:10.1029/2007GL031790.

St-Laurent, P., J. M. Klinck, and M. S. Dinniman (2013), On the Role of Coastal Troughs in the Circulation of Warm Circumpolar Deep Water on Antarctic Shelves, *Journal of Physical Oceanography*, *43*(1), 51–64, doi:10.1175/JPO-D-11-0237.1.

Stewart, A. L., and A. F. Thompson (2015), Eddy-mediated transport of warm Circumpolar Deep Water across the Antarctic Shelf Break, *Geophysical Research Letters*, *42*(2), 432–440, doi:10.1002/2014GL062281.

Stewart, A. L., and A. F. Thompson (2016), Eddy generation and jet formation on the Antarctic continental slope, *in Preparation*, doi:10.1175/JPO-D-16-0145.1.

Sverdrup, H. (1933), On the vertical circulation in the ocean due to the action of the wind with application to conditions within the Antarctic Circumpolar Current, *Discov. Rep.*, *VII*, 139–170.

Sverdrup, H. (1954), The currents off the coast of Queen Maud Land, *Norsk Geografisk Tidskrift*, *14*(1), 239–249, doi:10.1080/00291955308542731.

Thorsten, M., K. Christoph, and F. Eberhard (1998), *Ice Formation in Coastal Polynyas In the Weddell Sea and Their Impact on Oceanic Salinity*, chap. Antarctic, pp. 273–292, American Geophysical Union (AGU), Washington, D.C., doi:10.1029/AR074p0273.

Timmermann, R., and S. Goeller (2017), Response to FilchnerRonne Ice Shelf cavity warming in a coupled oceanice sheet model Part 1: The ocean perspective, *Ocean Science*, *13*(5), 765–776, doi:10.5194/os-13-765-2017.

Timmermann, R., and H. H. Hellmer (2013), Southern Ocean warming and increased ice shelf basal melting in the twenty-first and twenty-second centuries based on coupled ice-ocean finite-element modelling, *Ocean Dynamics*, *63*(9-10), 1011–1026, doi:10.1007/s10236-013-0642-0.

Timmermann, R., A. Beckmann, and H. H. Hellmer (2002), Simulations of ice-ocean dynamics in the Weddell Sea 1. Model configuration and validation, *Journal of Geophysical Research*, *107*(C3), 3024, doi:10.1029/2000JC000742.

Timmermann, R., S. Danilov, J. Schröter, C. Böning, D. Sidorenko, and K. Rollenhagen (2009), Ocean circulation and sea ice distribution in a finite element global sea ice-ocean model, *Ocean Modelling*, *27*(3-4), 114–129, doi:10.1016/j.ocemod.2008.10.009.

Timmermann, R., A. Le Brocq, T. Deen, E. Domack, P. Dutrieux, B. Galton-Fenzi, H. Hellmer, A. Humbert, D. Jansen, A. Jenkins, A. Lambrecht, K. Makinson, F. Niederjasper, F. Nitsche, O. A. Nøst, L. H. Smedsrud, and W. H. F. Smith (2010), A consistent data set of Antarctic ice sheet topography, cavity geometry, and global bathymetry, *Earth System Science Data*, *2*(2), 261–273, doi:10.5194/essd-2-261-2010.

Timmermann, R., Q. Wang, and H. H. Hellmer (2012), Ice-shelf basal melting in a global finite-element sea-ice/ice-shelf/ocean model, *Annals of Glaciology*, *53*(60), 303–314, doi:10.3189/2012AoG60A156.

Tiwari, M., S. S. Nagoji, T. Kartik, G. Drishya, R. K. Parvathy, and S. Rajan (2013), Oxygen isotopesalinity relationships of discrete oceanic regions from India to Antarctica vis-à-vis surface hydrological processes, *Journal of Marine Systems*, *113-114*, 88–93, doi:10.1016/j.jmarsys.2013.01.001.

Treasure, A., F. Roquet, I. Ansorge, M. Bester, L. Boehme, H. Bornemann, J.-B. Charrassin, D. Chevallier, D. Costa, M. Fedak, C. Guinet, M. Hammill, R. Harcourt, M. Hindell, K. Kovacs, M.-A. Lea, P. Lovell, A. Lowther, C. Lydersen, T. McIntyre, C. McMahon, M. Muelbert, K. Nicholls, B. Picard, G. Reverdin, A. Trites, G. Williams, and P. N. de Bruyn (2017), Marine Mammals Exploring the Oceans Pole to Pole: A Review of the MEOP Consortium, *Oceanography*, *30*(2), 132–138, doi:10.5670/oceanog.2017.234.

van Caspel, M. (2016), The importance of the western Weddell Sea to Weddell Sea Deep Water Formation, Phd thesis, Universität Bremen.

van Caspel, M., M. Schröder, O. Huhn, and H. Hellmer (2015), Precursors of Antarctic Bottom Water formed on the continental shelf off Larsen Ice Shelf, *Deep Sea Research Part I: Oceanographic Research Papers*, *99*, 1–9, doi:10.1016/j.dsr.2015.01.004.

Wang, Q., S. Danilov, and J. Schröter (2008), Finite element ocean circulation model based on triangular prismatic elements, with application in studying the effect of topography representation, *Journal of Geophysical Research*, *113*(C5), C05,015, doi:10.1029/2007JC004482.

Wang, Q., S. Danilov, E. Fahrbach, J. Schröter, and T. Jung (2012), On the impact of wind forcing on the seasonal variability of Weddell Sea Bottom Water transport, *Geophysical Research Letters*, *39*(6), 1–5, doi:10.1029/2012GL051198.

Wang, Q., S. Danilov, D. Sidorenko, R. Timmermann, C. Wekerle, X. Wang, T. Jung, and J. Schröter (2014), The Finite Element Sea Ice-Ocean Model (FESOM) v.1.4: Formulation of an ocean general circulation model, *Geoscientific Model Development*, *7*(2), 663–693, doi:10.5194/gmd-7-663-2014.

Wang, Z., and M. P. Meredith (2008), Density-driven Southern Hemisphere subpolar gyres in coupled climate models, *Ge*, *35*(April), 1–5, doi:10.1029/2008GL034344.

Wouters, B., A. Martin-Español, V. Helm, T. Flament, J. M. van Wessem, S. R. M. Ligtenberg, M. R. van den Broeke, and J. L. Bamber (2015), Glacier mass loss. Dynamic thinning of glaciers on the Southern Antarctic Peninsula., *Science (New York, N.Y.)*, *348*(6237), 899–903, doi:10.1126/science.aaa5727.

Yuan, X. (2004), ENSO-related impacts on Antarctic sea ice: a synthesis of phenomenon and mechanisms, *Antarctic Science*, *16*(4), 415–425, doi:10.1017/S0954102004002238.

Zhou, Q., T. Hattermann, O. A. Nøst, M. Biuw, K. M. Kovacs, and C. Lydersen (2014), Wind-driven spreading of fresh surface water beneath ice shelves in the Eastern Weddell Sea, *Journal of Geophysical Research: Oceans*, *119*(6), 3818–3833, doi:10.1002/2013JC009556.

Zwally, H. J., J. C. Comiso, C. L. Parkinson, D. J. Cavalieri, and P. Gloersen (2002), Variability of Antarctic sea ice 19791998, *Journal of Geophysical Research*, *107*(C5), 3041, doi:10.1029/2000JC000733.

Zweng, M. M., J. R. Reagan, J. I. Antonov, R. A. Locarnini, A. V. Mishonov, T. P. Boyer, H. E. Garcia, O. K. Baranova, D. R. Johnson, D. Seidov, and M. M. Biddle (2013), World Ocean Atlas 2013, Volume 2: salinity, in *Atlas NESDIS 74*, edited by S. E. Levitus and A. V. T. E. Mishonov, p. 39 pp.

Acknowledgements

First of all, I would like to thank my supervisors Dr. Michael Schröder and Dr. Ralph Timmermann for their support and care during my time as a PhD student. Many thanks for always finding time to answer questions and for providing valuable advice. Special thanks to Prof. Dr. Torsten Kanzow, who was always supportive of my work in all aspects, including my general work but also my attendance at conferences, summer schools and research stays abroad.

Thank you Dr. Michael Schröder for introducing me to this exciting topic and for giving me the chance to visit the fascinating place Antarctica several times. I am grateful for your continuous unconditioned support and fruitful scientific as well as general discussions.

I would like to thank Dr. Ralph Timmermann for introducing me to FESOM and for being patient with me being critical of the model, I know it was not always easy. I am grateful for your detailed proofreading of several manuscripts.

Special thanks to Dr. Tore Hattermann, who became an unofficial advisor to me during my PhD. Thank you for introducing me to new analysis methods and for always providing constructive comments on my work. Furthermore, I would like to thank you Dr. Svein Østerhus and Dr. Elin Darlius for inviting me to Bergen to work with you. Special thanks to Elin Darelius for a great cooperation throughout my PhD and for giving me the chance to participate in the *Coriolis* tank experiments in Grenoble.

Thanks to Dr. Hartmut Hellmer for dedicated proofreading of manuscripts and for valuable discussions. To Lukrecia Štulić and Mathias van Caspel, thank you for your valuable help with FESOM. Thanks to Andreas Wisotzki and Dr. Gerd Rohardt for high-quality data processing of CTD and mooring data, which is an essential part of successful science. Finally, I am grateful to Prof. Dr. Monika Rhein for reviewing my thesis.

Thank you to the Helmholtz Graduate School for Polar and Marine Research

(POLMAR) for providing travel support at several occasions.

Special thanks goes to all my colleagues and friends at work, in particular, Dr. Janin Schaffer, Lukrecia Štulić and Nicolas Le Paih, who made me feel happy, laughed with me and supported me at all times. You made my time in Bremerhaven worthwhile.

Most sincere thanks to my family for their unconditional love and support at all times. I am proud to have such a great family. My deepest gratitude goes to my husband, Brett Ryan, for being the rock in my life. You make me laugh every day and show me what happiness in life is about.